Steady and Unsteady Waves Generated by a Moving Body and Multiple Bodies

PhD Thesis

Mingxin Li

Department of Naval Architecture, Ocean and Marine Engineering
University of Strathclyde, Glasgow

April 6, 2020

This thesis is the result of the author's original research. It has been composed by the author and has not been previously submitted for examination which has led to the award of a degree.

Abstract

When a single ship moves through calm water, it generates a steady surface wave. Although vessels do spend the majority of their operational time traveling at a constant speed in the waterways of uniform depth, there are circumstances when the unsteady effects can be significant. Among these examples are:

- In practical operations, when a ship maneuvers in a port/harbour/lock environment. Under this circumstance, a ship is likely to travel in close proximity to waterway boundaries that have an abrupt change, i.e., a step-change in bank dimension or bottom depth;

- When conducting ship model tests in a towing tank, the ship model is accelerated from the rest to the target speed. The measured resistance was found to experience persistent periodic oscillations after the target speed was achieved (Doctors et al., 2008);

- When a ship is moving during overtaking (or being overtaken) or passing other ships in a dense shipping traffic environment. The interaction between ships will initiate the unsteady forces/moments.

The aforementioned unsteady effects are associated with the unsteady waves on the free surface. The two main objectives of this thesis are 1) to develop a linear method and implement a numerical programme to simulate the steady waves generated by a single body and to predict the wave interference between multiple bodies; 2) to develop an unsteady and nonlinear methodology to predict the unsteady waves generated by the aforementioned unsteady circumstances.

Chapters 2 & 3 are presented in this thesis to achieve objective 1). Chapter 2 deals

with the steady waves generated by a single body. The numerical demonstration case in this chapter is a ship passing a false bottom in towing tank tests. Chapter 3 extends the methodology developed in Chapter 2 to investigate the steady wave interference phenomenon by multiple bodies. The numerical demonstration case in this chapter is the steady hydrodynamic interaction between human swimmers.

Chapter 4 & 5 are presented in this thesis to achieve objective 2). Chapter 4 will introduce the unsteady boundary condition to the mathematical model developed in Chapters 2 & 3. In particular, a nonlinear and unsteady free surface boundary condition will be implemented to account for the unsteady effects initiated by the acceleration or the changing water depth. The numerical demonstration case in Chapter 4 is the unsteady waves generated by an accelerating ship. The methodology developed in Chapter 4 will be extended in Chapter 5 to account for the unsteady interaction between multiple bodies. A superposition method will be deployed to investigate the waves generated by two ships at different speeds. The numerical demonstration case in Chapter 5 is the hydrodynamic interaction between two ships during the overtaking operation.

Contents

List of Figures

List of Figures

List of Tables

List of Tables

List of the publications

1. Li, M., Yuan, Z. and Delefortrie, G., 2019. Investigation of the false bottom effects on ship model tests, in The Sixth International Conference on Advanced Model Measurement Technology for the Maritime Industry (AMT'19).(Li et al., 2019)

2. Yuan, Z.M., Li, M., Ji, C.Y., Li, L., Jia, L. and Incecik, A., 2019. Steady hydrodynamic interaction between human swimmers. Journal of the Royal Society Interface, 16(150), p.20180768.

3. Li, M., Yuan, Z.M., and Incecik, A., 2020. Unsteady waves generated by an accelerating ship in shallow water. Submitted to Ocean Engineering.

4. Li, M., Yuan, Z.M., and Yeung, R.W. (2020) On Unsteady Wave-Making Resistance Of An Accelerating Ship, OMAE-2020 Conference, June 28-July 3, 2020.

5. Li, M., Yuan, Z.M., and Yeung, R.W. (2020) Unsteady waves generated by a ship travelling over a step bottom, the 35th Intl Workshop on Water Waves and Floating Bodies, 26-29 April, 2020.

Preface/Acknowledgements

I would like to express my great thanks and gratitude to my supervisor Dr. Zhiming Yuan at Strathclyde University, for his quality and kindly academic supervision, guidance as well as endless support throughout the years of this research. I thank him for the enormous concern for my work at Strathclyde University. During my PhD time, his kind encouragement of my current and future research development inspired me in what I do, especially for building a decent foundation for my academic career.

I also would like to thank my co-supervisor, Prof. Atilla Incecik at Strathclyde University, who has always been accessible to advise me for his valuable advice and helpful suggestions during my study. My sincere appreciation goes to Prof. Ronald W. Yeung at the University of California at Berkeley for his support and guidance throughout the paperwork.

I want to extend my great appreciation to Dr. Weichao Shi and Dr. Yibo Liang who have helped me with the experience of fluid dynamics from the beginning of my research. Their valuable comments always extend and inspire my understanding of the research.

I also wish to thank significantly my friends and schoolmates, Mr. Zhenkai Zhao, Mr. Mingyang Li and Mr. Xiudi Ren, Mr. Yang Zhou at Strathclyde University for their endless help throughout my PhD programme.

I am grateful to my parents and wife, without their encouragement and understanding, I could not finish my PhD career.

Chapter 1

Introduction

1.1 Background

In response to the continuously increasing demand for world trade, more and larger vessels navigate in confined waterways. However, the waterway dimensions cannot become increased with the same speed as the vessel dimension does. It causes the safety margins of the exhausted increasing navigation due to the ports still need to keep pace with the ship improvement. The hydrodynamic interactions can cause significant forces or moments to be exerted on one or all of the ships when two or more vessels are operating close to each other. Such loads are particularly important in shallow water, like the harbour area, confined channel, or canal, where the restricted flow accentuates the interaction effects. Therefore, the ships are more likely to be close due to navigational constraints. Navigation errors may result in ship accidents with catastrophic consequences for man, cargos, and environment.

Describing the hydrodynamic characteristics of the multiple bodies is very complicated. It is not only because of the interaction between the bodies but also the physical process of the body-wave problem is extremely complex. Based on whether the configuration of the bodies floating on the free surface is time-independent or not, the hydrodynamic interaction between multiple bodies can be divided into two problems: steady or unsteady problem. The term 'steady' is used here to describe the time-independent process when the ships are moving on parallel tracks with the same velocities, as in a refuelling oper-

ation. The 'unsteady' problem of the multi-bodies can be illustrated as in an overtaking maneuvre, a meeting maneuvre or passing a moored ship. Besides, the latter includes the unsteady process during a single ship accelerating from the rest to a constant speed. The ship motion problem is not considered in this work.
This is a thesis by publication and conference paper. The thesis contains an introduction (Chapter 1), core chapters (Chapters 2–5) containing the results and a conclusion (Chapter 6). The core chapters of the thesis consist of journal articles and conference papers that have been primarily written by the author.

1.2 Literature review

In recent years, numerous studies have attempted the solution of the inviscid steady flow past ships. However, the unsteady effects can be significant in some circumstances, for example, a ship travels near the waterway with uneven boundaries, a ship model is accelerated from the rest to the target speed, and a vessel is overtaking or passing other ships in the dense shipping traffic environment. This unsteady effect could induce a fluctuation of the hydrodynamic forces/moments. Precisely, the unsteady effect is mainly generated by the unsteady flow around past ships (Day et al., 2009; Doctors et al., 2008). Therefore, to investigate the unsteady phenomena, the present study involves in steady and unsteady waves generated by a single body and multiple bodies. It will be divided into three parts in this literature review: 1. the steady wave generated by ships; 2. The unsteady wave generated by a ship; 3. Ship to ship interaction problem.

1.2.1 The steady wave generated by ships

Because of the complexity of the flow phenomena involved, steady waves generated by the surface-piercing ships were calculated in the past mainly by the potential flow methods under assumptions concerning the body geometry, free surface, and the speed. Around the first half of the 20th century, early attempts to model ships in potential flow focused on variations of thin-ship theory (Michell, 1898) and the related slender-body theory (Tuck,

1966a) to solve the steady ship motion problem, where the vessel is assumed to advance steadily in an otherwise calm sea. Based on the slender-body theory, Newman (1985) used the perturbation theory to the wave resistance problems. The strip theory is one of the varieties of the slender body theory developed (Lewis, 1929) and improved (Salvesen et al., 1970) to predict the seakeeping performance of a variety of hull types. The slender-body theory required that the lateral variations are small and smooth along the length. While linearized approaches have been available for problems in two dimensions for some time, three-dimensional formulations have been relatively developed.

Until the 1950s, with the advent of digital computers, the application of hydrodynamic theory became practical for ships. Hess and Smith (1964) pioneered the first three-dimensional surface-source panel method for calculating potential flows about arbitrary configurations in an unbounded fluid. To solve the free surface flow problem involving a steady forward speed, the two most promising panel methods: 1. Wave Green function, in which only the ship/body wetted surface needs to be discretized; 2. The Rankine source method, in the review by Yeung (1982). Although for the Wave Green function, it does not need to distribute the elements on the free surface, it has disadvantages in considering the nonlinear effect and the shallow water effect. The simple-source formulation (Rankine source method) was solved in the boundary-integral equation method as one of the major numerical methods. This Boundary Element Method forms the basis of the majority of the computational algorithms for the numerical solution of the linearized wave resistance problem (Nakos, 1990). Since the pioneering work of Dawson (1977) who used the Rankine source method to solve the steady wave resistance problem of the slow-ship, based on the proposed model of the double body flow, various Rankine source methods regarding a free surface condition have been developed. When the ship travelling with constant slow speed in the open water, the wave resistance can be solved very accurate due to the linear term is dominant. The double-body flow is the wave pattern that bears more resemblance to reality. In this flow, there is no longer a free surface, no waves are generated, but at least the no-flux condition on the hull of the ship is satisfied. Therefore, this method is also only valid for lowspeeds. The Neumann-Kelvin method is also one of the most popular methods to solve the linear hydrodynamic problems in the time domain or frequency do-

main (King, 1987; King et al.; Newman, 1985). It enforces the exact boundary condition on the mean position of the body. For the steady ship-wave analysis, it has been reported by applied the Rankine source method (Kara, 2000; Kring, 1994b). The steady problem of a ship moving with a constant speed has been widely studied (Nakos et al., 1994; Raven, 1998; Sclavounos and Nakos; Tarafder and Suzuki, 2008; Yuan et al., 2019). Yuan (2019) validated the feasibility of the Rankine source method in investigating the hydrodynamic behaviour of the ships advancing in confined waterways. Generally, the ship model tests in limited water depth are achieved by varying the water depth in the towing tank. The most effective and reliable method is changing the water depth by the installation of an artificial bottom. However, a large full-size false bottom is usually accompanied with a small stiffness and will be easily deformed. Therefore, during shallow water tests, the false bottom is usually truncated at a limited size. This leads to the question of how much error could be induced on the ship behaviour by differences in size and configuration of the false bottom. To the author's knowledge, there is limited research that could quantify the error caused by a false bottom with limited horizontal dimensions.

On the other hand, many problems in swimming competitions are associated with steady wave phenomena. It has also been validated in naval architecture that the wave-cancellation effect is beneficial for drag reduction of multihull vessels (Faltinsen, 2005; Soding, 1997; Tuck and Lazauskas, 1998). Pioneering studies have provided fundamental insight into the interactions between a group of animals moving in formation. The studies on ducklings swimming in formation (Fish, 1994, 1995), fish in schools (Weihs, 1973) and single-file line or birds flying in a 'V' formation (Badgerow and Hainsworth, 1981; Lissaman and Shollenberger, 1970; May, 1979; Portugal et al., 2014; Weimerskirch et al., 2001) have found the energy consumption of individuals during group locomotion could be reduced. The 'aid' that the animal acquired from its companions varies by species. Inspired by the behaviour of animals in formation, these studies shed light on the performance of human competitive swimmers. Following questions are interested in Chapter 3. Can the following swimmers benefit from the wakes of the leading swimmers, thus reducing the drag and conserving the energy cost? Thus the hydrodynamic interaction between two or three swimmers swimming at the same speed would be study to explain the interaction in terms

of the wave interference phenomenon.

1.2.2 Unsteady wave and wave resistance

In practical operations when a ship maneuvers in close proximity to waterway boundaries that have an abrupt change or towing a ship model accelerated from the rest to the target speed, the unsteady effect becomes significant (Calisal, 1977; Doctors et al., 2008; Wehausen, 1964). However, the unsteady wave generated by an accelerating ship or abrupt bottom, particularly in shallow water, was rarely investigated. Some pioneer works in the early 1950s shed light on the unsteady wave resistance. Lunde (1951) developed an unsteady theory to analyze the ship-wave problem. Based on Lunde's theory, Wehausen (1964) proposed asymptotic formulas to predict the unsteady wave resistance of a ship. The experiments conducted by Doctors et al. (2008) showed that the linearized theory (Doctors, 1975) provided well predictions of the acceleration effect on the resistance. However, he did not analyse the impact of different water depth on the unsteady waves generated by the accelerated ship. The inland ships are most likely to maneuvre in shallow water. The behaviour of a vessel in shallow water was investigated by slender-body theory (Chen and Sharma, 1995; Gourlay, 2008; Tuck, 1966a) and experimental measurements (Kijima and Nakiri, 1990). The unsteady problem of an accelerating ship remains a challenging issue. The shallow water equation (Boussinesq equations) has been used numerically to simulate the waves generated by a ship at critical speed in limited water depths. Torsvik et al. (2006) investigated the speed effects on the waves generated by a ship passing through the transcritical speed region in shallow water based on Boussinesq equations. In their simulations, they examined the amplitude of the waves generated by a ship with various Froude numbers near-critical speeds. Li and Sclavounos (2002) used modified Boussinesq equations to calculate the nonlinear long waves generated by a disturbance moving at critical speed. However, they did not consider the unsteady effects when a vessel is accelerated from the rest.

1.2.3 Ship to ship problem

When a vessel is overtaking (or being overtaken) or passing other ships in the dense shipping traffic environment. The interaction between ships will initiate unsteady forces/moments. The interaction effects are increased when the ships are maneuvring in confined waterways, or when the ships are travelling with high speed. During the 1960s-1990s, the slender-body theory is one of the most reliable methodologies that has been widely used (Collatz, 1963b; Dand, 1975a; Kijima and Yasukawa, 1985; Tuck, 1966b; Tuck and Newman, 1974; Varyani et al., 1998b; Yeung, 1978a). In these studies, some significantly simplified assumptions for the body geometry and ship speed were adopted in the mathematical model and led to a high-efficiency numerical calculation. For the ships travelling at relatively low Froude numbers, the numerical calculations showed a good prediction of the sway force and yaw moment on ships during overtaking or meeting operations. To account for the three-dimensional effects and remove the geometrical idealization. Korsmeyer et al. (1993a) adopted a three-dimensional panel method, which applies to any number of arbitrarily shaped bodies in arbitrary motions. Pinkster (Pinkster, 2004) extended Korsmeyer's method with the implementation of a model to account for the free surface effects partially. However, his model only involves the impact of the passing ship on a moored ship. Therefore, the most critical far-field waves or so-called Kelvin waves were neglected. Especially, the divergence wave system has the more severe effect on the interaction. More recently, the three-dimensional panel method has been more commonly used (Söding and Conrad, 2005; Xiang and Faltinsen, 2010; Xu et al., 2016; Zhou et al., 2012a). However, few efforts has yet been made to investigate the effects of unsteady free surface waves on interaction forces. Thus, the thesis would extend the developed numerical algorithm to the unsteady wave problem generated by two ships during overtaking in deep or shallow water.

1.3 Aims & Objectives

This thesis is concerned with the hydrodynamic problem that arises when vessels advance on the sea surface. Both the steady and unsteady free surface flow is addressed. The

ultimate objective of this study is the development of a computational algorithm that will consider the steady or unsteady effect between the multi-bodies and the free surface in shallow water. The solution of the free surface flow around vessels advancing at high speed is in the scope of the present study. Accordingly, the current research includes the following specific tasks:

• To predict the behaviour of a single ship travelling steadily in shallow water.

• To investigate the coupled behaviour between the simply swimming bodies in a steady motion.

• Extend the numerical program from the steady problem to predict the unsteady problem of the single ship accelerated from the rest to a constant speed.

• Extend the numerical program to investigate the unsteady interaction forces among multiple ships of bodies, which are operating near to each other during the passing or overtaking process.

1.4 Thesis Outline

The main objective of the present thesis is to study the fluid mechanics of steady or unsteady waves around the multi-bodies. Before achieving this objective, the basic solution should be established to investigate the steady motion of single or multi-ships. After that, it can extend the numerical program from solving the steady problem to solve the unsteady problem. The thesis is structured in the following major parts, as shown in Figure 1.1.

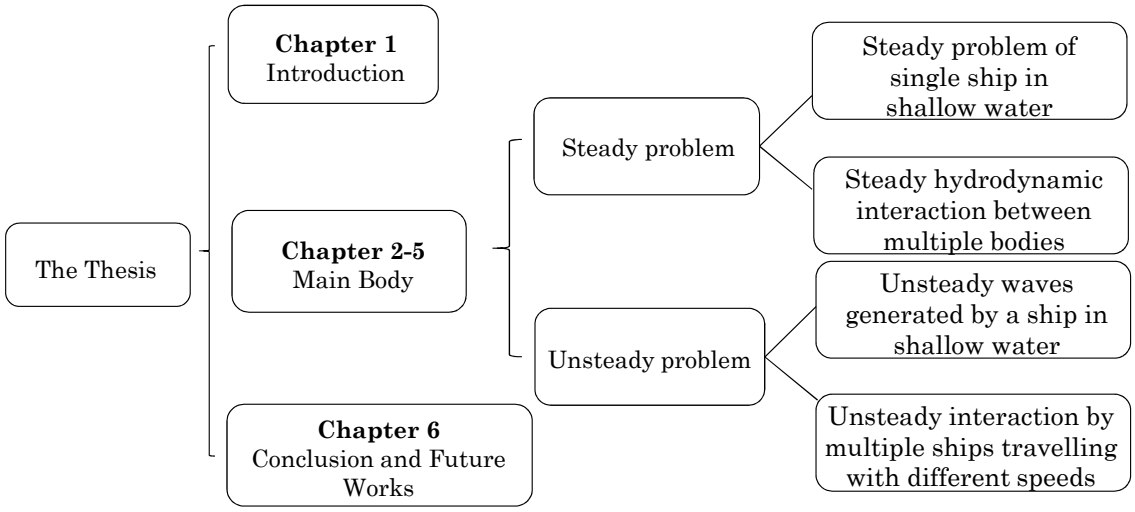

Figure 1.1: Thesis Outlines.

- Chapter 1 introduces the background and the objectives of the present study following the outlines.
- Chapter 2 predicts the interaction effects between the false bottom and the ship model and to quantify the test errors (in percentage) due to different configurations and sizes of the false bottom.
- Chapter 3 focuses on the hydrodynamic interaction between two or three human swimmers in competitive swimming.
- Chapter 4 develops a numerical algorithm for investigating the unsteady wave resistance acting on a ship moving from the acceleration phase to the constant-speed stage in shallow water.
- Chapter 5 extends the numerical algorithm for the unsteady motion of the ships during overtaking in restricted waterways.
- Chapter 6 summaries the main contributions of the present work. A list of references is presented at the end of the thesis.

In the present study, the Rankine source method proposed by Hess and Smith (1964) will be applied, which uses a simple Green function in the boundary integral formulation. This

method requires the sources distributed not only on the body surface but also on the free surface and sea bottom surface. As a result, a flexible choice of free surface condition and sea bottom condition can be realized in these methods. The nonlinear free surface condition and the shallow water effects can be taken into consideration in the BVP. A 3-D boundary element program based on the Rankine source method will be developed to investigate the hydrodynamic interaction between multi-bodies arranged side by side with a forward speed in shallow water. The hydrodynamic forces of the bodies and the wave patterns will be calculated and compared to the experimental results.

Chapter 2

Steady waves generated by a single ship in shallow water

2.1 Introduction

It has already been pointed out that ships are most likely to maneuvre in shallow water, which probably results in larger hydrodynamic forces, control loss and more energy consumption (Sun et al., 2013). It is, therefore, crucial to investigate the behaviour of a ship in such conditions. The most reliable option is the execution of full-scale experiments, but this is rarely performed due to the massive cost involved.

As an alternative, the behaviour of a ship in shallow water can be studied theoretically, as was done by Tuck (1966a), who used the slender-body theory to solve the disturbance to a stream of shallow water due to a slender body. The slender –body theory was also used by (Chen and Sharma, 1995) to investigate the hydrodynamic performance of a ship moving at a near-critical speed in a channel, and by Gourlay to predict the ship squat (Gourlay, 2008).

With the development of higher performance computation, numerical methods have been implemented to solve the problem of a ship moving in shallow water. Numerous examples can be found in literature, such as Saha et al. (2004), who used a RANS method to improve the hull form in shallow water. Terziev et al. (2018) studied the hydrodynamic interaction between the hull and the seabed, the sinkage, trim and resistance of the Duis-

burg Test Case (DTC) container ship is simulated using CFD, and the results obtained have been compared with the computation by the slender-body theory and various empirical methods. Full numerical simulations are nowadays also possible as shown by Carrica et al. (2016), who studied experimentally and numerically the 20/5 zigzag maneuver for the container ship KCS in shallow water.

Apart from theoretical methods Kijima et al. (1990), among others, proposed a prediction method for ship maneuvrability in deep and shallow waters, based on approximate formulae, at the initial stage of design. Such empirical formulae can be obtained by analysing existing data or by studying model test results. The latter is still one of the most common methods for estimating ship maneuvrability to simulate the maneuvring motion. During such a program, multiple experiments are needed to capture the hydrodynamic performance fully. Some examples of the KCS hull model in shallow water were conducted in the towing tank (Carrica et al., 2016; Enger et al., 2010).

The organizing committee of SIMMAN 2014 (Simman, 2014) has the purpose of benchmarking the capabilities of different methods for simulating ship maneuvring (Shen et al., 2014; Yasukawa and Yoshimura, 2015). Since 2014, shallow water tests are also included. During such experiments, the water depth has to be adapted. It means that the water has to be drained out of the tank, which is not always feasible, or at least time-consuming. As an alternative, some towing tanks are equipped with a false bottom. It enables the facility to adjust the water level in a fast way. Examples of such test campaigns can be found in (Mucha et al., 2016; Yeo et al., 2016).

A false bottom facility has also been built at the Maritime and Ocean Engineering Research Institute (MOERI) /KRISO towing tank. The tank tests are usually conducted by steadily towing the ship model, either in deep water or in shallow water. Comparing the full dimension of the tank, the false bottom usually does not cover the full length and width of the tank. The question arises: does the truncated false bottom bring uncertainties when comparing with the full-size real bottom? To the author's knowledge, this question has never been addressed. One can imagine that such a false bottom influences the ship's behaviour, similarly as tank walls can affect the result of a resistance test as described by Raven (2018).

The objective of the present study is to investigate the interaction effects between the false bottom and ship model and to quantify the test errors (in percentage) due to different configurations and sizes of the false bottom. In this Chapter, a 3D panel method based on the Rankine type Green function will be used to solve the hydrodynamic problem of a ship model maneuvring in tanks equipped with various false bottom configurations. This panel method based on the potential flow theory has been widely and successfully applied to various hydrodynamic problems (Yuan et al., 2015b; Yuan et al., 2019).

In this Chapter, the numerical convergence analysis and validation tests were firstly carried out to examine the hydrodynamic forces and wave profiles of a benchmark ship model (Li et al., 2019). After the validations, the present numerical approach was then applied to investigate the false bottom problem. A contour of errors (in percentage) induced by the limited size of the false bottom was finally obtained, showing the effects of the width and submerged depth of the false bottom.

2.2 Facilities and Methodology

2.2.1 Numerical towing tank and false bottom facilities

A false bottom was set up symmetrical on the longitudinal centre line of the towing tank. The ship model is towed along the longitudinal centre line. Thus, the lateral forces (moments) are negligible due to the cancellation effect. Figure 2.1 (a) and (b) are the side view and front view of the towing tank, respectively, showing the dimension and position of the false bottom facility. The physical characteristics of the numerical towing tank and the false bottom is shown in Table 2.1. For a ship with forwarding speed, two right-handed coordinate systems are used: a global reference frame $O - x_0y_0z_0$ fixed to the earth, and a local reference frame $o - xyz$ fixed to the body. Both frames have positive x-direction pointing towards the bow, positive z-direction pointing upwards. The local body-fixed $o - xyz$, as shown in Figure 2.1, is set on the undisturbed free surface.

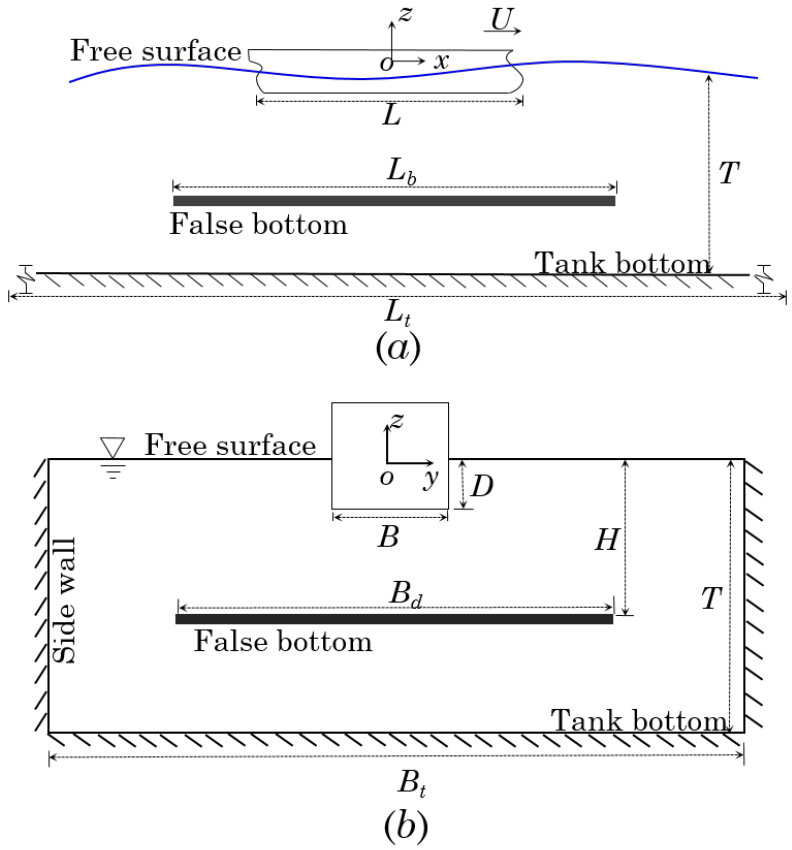

Figure 2.1: (a) Side view of the false bottom; the false bottom shows in the figure as a black plane and L denotes the length of the ship hull. (b) Front view of the false bottom. B and D denote the ship's breadth and draught. The breadth of the false bottom and the tank bottom is B_d *and* B_t, respectively. The false bottom is placed at a submerged depth H. The water depth of the tank is denoted by T.

The sketch of the tank equipped with a false bottom facility is shown in Figure 2.1. The dimension of the KRISO towing tank is 200m $\times$ 16m $\times$ 7m ($L_t \times B_t \times T$). The length of the false bottom L_b is 54 m, which is assumed to be sufficiently long and the false bottom effect in the length dimension will not be investigated. We mainly focus on the truncated effects in the breadth dimension. In the present study, the breadth of the false bottom varies from 0 to 16 m. The false bottom effect is also determined by the bottom depth H and towing speed U.

Table 2.1: Characteristics of Numerical towing tank and false bottom

	Items	Value
Towing tank	Length (m)	200
	Breadth (m)	16
	Depth (m)	7
False bottom	Length (m)	54
	Breadth (m)	0-16

2.2.2 Methodology

The present study aims to investigate the interaction effects between the false bottom and the ship model, and to quantify the test errors (in percentage) due to different configurations and sizes of the false bottom. To achieve this goal, a criterion must be identified to quantify the false bottom effects. In captive model tests, when a ship is towed along the centre line of a tank with/without a false bottom, the differences are mainly represented by the model's hydrodynamic characteristics, including the forces/moments in surge, heave and pitch directions, and the free surface waves. In this Chapter, we mainly focus on force-based criteria to assess the difference due to the presence of the false bottom. In particular, the wave-making resistance is used as the quantity to calculate the errors (in percentage) due to different configurations and sizes of the false bottom. Of course, the results of sinkage and trim can also be provided as supplementary criteria to show whether the false bottom effects are sensitive to criteria selection. To calculate these quantities (forces/moments/waves), a mathematical model, which is the boundary value problem (BVP), needs to be established. The boundary element method (BEM) based on potential flow theory will be used to calculate these qualities. Based on the assumptions for the potential flow theory, it neglects the viscosity and compressibility of the flow. Therefore, the fluid domain can be described by using a disturbance velocity potential φ, which represents the presence of the ship in the fluid domain. In the fluid domain, the potential φ satisfies the Laplace equation:

$$\frac{\partial^2 \varphi}{\partial x^2} + \frac{\partial^2 \varphi}{\partial y^2} + \frac{\partial^2 \varphi}{\partial z^2} = 0 \tag{2.1}$$

In the body-fixed frame, the kinematic boundary condition on the free surface can be expressed as

$$g\zeta - U\frac{\partial \varphi}{\partial x} + \frac{1}{2}\left(\frac{\partial^2 \varphi}{\partial x^2} + \frac{\partial^2 \varphi}{\partial y^2} + \frac{\partial^2 \varphi}{\partial z^2}\right) = 0 \tag{2.2}$$

where the U defined as the ship speed. The dynamic boundary condition on the free surface is

$$-U\frac{\partial \zeta}{\partial x} + \frac{\partial \varphi}{\partial x}\frac{\partial \zeta}{\partial x} + \frac{\partial \varphi}{\partial y}\frac{\partial \zeta}{\partial y} = \frac{\partial \varphi}{\partial z} \tag{2.3}$$

where $\zeta(x, y, t)$ is the free surface wave elevation. By applying a Taylor series expanded about $z_0 = 0$ and assuming the disturbance of the fluid is small, the non-linear terms may be neglected when substituting Equation 2.2 into Equation 2.1. In the steady study, it can be simplified to the well-known linearized steady Neumann-Kelvin free surface condition (Newman, 1977), which can be written as

$$U^2\frac{\partial^2 \varphi}{\partial x^2} + g\frac{\partial \varphi}{\partial z} = 0 \tag{2.4}$$

where g is the acceleration due to gravity. Apart from the free surface condition, there should be no flow through the wetted surface S_B, which is the body surface boundary condition:

$$\frac{\partial \varphi}{\partial n} = Un \tag{2.5}$$

where $n = (n_1, n_2, n_3)$ is the unit normal vector inward on the wetted body surface. Besides, a radiation condition is imposed on the control surface to ensure that waves vanish at upstream infinity:

$$\varphi \longrightarrow 0,\ \zeta \longrightarrow 0\ as\ \sqrt{x^2 + y^2} \longrightarrow \infty \tag{2.6}$$

By the same reasoning, the boundary condition on the sea bottom and false bottom can be expressed as

$$\frac{\partial \varphi}{\partial n} = 0 \tag{2.7}$$

Equation 2.4 to 2.7 form a completed set of BVP. Each set of BVP is independent and can be solved by the Rankine source panel method. Once the unknown potential φ is solved, the pressure over the body surface can be obtained from linearized Bernoulli's equation

$$p = -\rho U \frac{\partial \varphi}{\partial x} \tag{2.8}$$

By integrating the pressure over the hull surface, the forces (or moments) can be obtained by

$$F_i = \iint_S p n_i ds, \ i = 1, \ 2, \ ..., \ 6 \tag{2.9}$$

where i represents the force in surge, sway, heave, roll, pitch and yaw directions. The wave elevation on the free surface can be obtained from the dynamic free surface boundary condition in Equation 2.3 in the form

$$\zeta(x, y) = \frac{U}{g} \frac{\partial \varphi}{\partial x} \tag{2.10}$$

2.2.3 Numerical implementation

To solve the BVP, the in-house-developed numerical program MHydro will be used. In numerical calculations, one cannot consider an infinite free surface domain. Thus, the computational domain needs to be truncated at a distance away from the ship hull in order to eliminate the wave reflection from the truncated boundaries and to improve the numerical stability in the computational domain. In the present study, a 2^{nd}-order upwind difference scheme is applied on the free surface to obtain the spatial derivatives of the velocity potential:

$$\frac{\partial^2 \varphi}{\partial x^2}(x_i) = \frac{1}{\Delta x^2} \left[\frac{1}{4}\phi(x_{i+4}) - 2\phi(x_{i+3}) + \frac{11}{2}\phi(x_{i+2}) - 6\phi(x_{i+1}) + \frac{9}{4}\phi(x_i) \right] \tag{2.11}$$

where i denotes the element's number related to the collected point, which is influenced by four elements backwards in the stream along the x-direction.

2.3 Validations on the single body in open water

2.3.1 Validations of a submerged prolate

The case of a submerged ellipsoid has already been studied by Doctors and Beck (Doctors and Beck, 1987) and Farell and Guven (Farell and Guven, 1973). The present 3D numerical results of wave resistance are compared with Doctors, who carried out two types of numerical approach, the collocation method and the Galerkin method for the Neumann-Kelvin problem of the submerged body. Farell (1973) conducted Towing-tank measurements of the resistance components of a spheroid model. It is defined as same as the Doctors that the dimeter-to-length ratio $D/L = 0.2$ and the Froude number is equal to $F_n = U\sqrt{gL}$. The basic coordinate system and panelling definition are shown in Figure 2.2. Two different submerged depth-to-submergence ratios $H/L = 0.16,\ 0.2454$ is taken as the factor for the effects of the model depths in the water. The non-dimensionalized coefficients of surge force are shown below,

$$C_w = \frac{R_w}{(1/2)\rho U^2 S} \tag{2.12}$$

where S is the area of the wet body surface and R_w denotes the wave-making resistance, which equals F_1 in Equation. 2.12

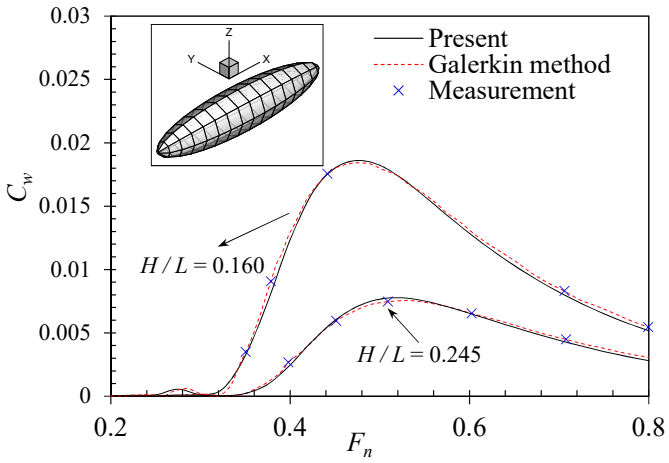

Figure 2.2: Comparison of wave resistance for submerged prolate ellipsoid with (a). numerical calculation of Galerkin method by Doctors (Doctors and Beck, 1987) and (b). experimental measurements (Farell and Guven, 1973) at different H/L.

Coefficients of the wave resistance acting on single submerged prolate ellipsoid compare with other calculations by Galerkin method and experiment at different submerged depth showed in Figure 2.2. The results obtained by the present numerical computations have satisfied agreements with other values. It is accurate for our present code to implement it into the simulation of the ship model. From the Figure 2.2, it indicates that the effect of the free surface on the wave resistance acting on the ellipsoid is significant due to the amplitude of the curves has a great increase at $H/L = 0.16$. We note that the wave resistance has an extreme value corresponding to Froude number $F_n = 0.5$.

2.3.2 Validations of the Wigley III hull

In the present study, we use a benchmark model Wigley III hull in the case studies. In the numerical modelling, the panels are not only distributed on the free surface and wetted body surface of the ship hull, but also on the false bottom. The mesh of the computational domain is shown in Figure 2.3. In the presented study, due to the symmetrical characteristic of the domain, only half of the computation domain is modelled. It allows a reduction of the total number of the panels required in the solution, hence saving computation time. The main particulars of a model scale Wigley III hull are listed in Table 2.2.

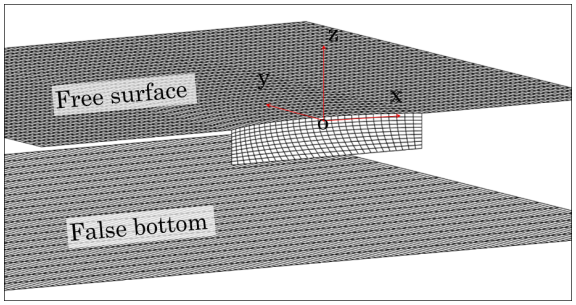

Figure 2.3: Panel distribution on the computation domain of a Wigley III model advancing in a tank equipped with a false bottom. There are in total 7354 panels distributed on the total computation domain in this simulation: 4,654 panels distributed on the free surface S_F, 300 on the wetted body surface $_H$ and 2400 on the false bottom S_B. The computational domain is truncated at $1.2L$ upstream, $1L$ sideways and $2L$ downstream.

Table 2.2: Principal dimensions of the Wigley III model

Dimensions Item	Value
Length (m)	3.0
Breadth (m)	0.3
Draft (m)	0.1875

To validate the present methodology and numerical method, we calculated the wave-making resistance coefficients C_w and wave profile ζ at the starboard of the ship model. The numerical results of the wave resistance coefficient and wave elevation are obtained and compared with the experimental results from different institutions (Kajitani et al., 1983) as well as the numerical results from Huang et al. (2013) obtained from Neumann-Michell theory, as shown in Figure 2.4 (a) and (b), respectively. The results show that a satisfactory agreement is achieved between the numerical predictions and experimental measurements. The waves at both the bow and stern areas are underestimated due to the linear assumption of the present method. The non-linear effect cannot be estimated by using the present linear method.

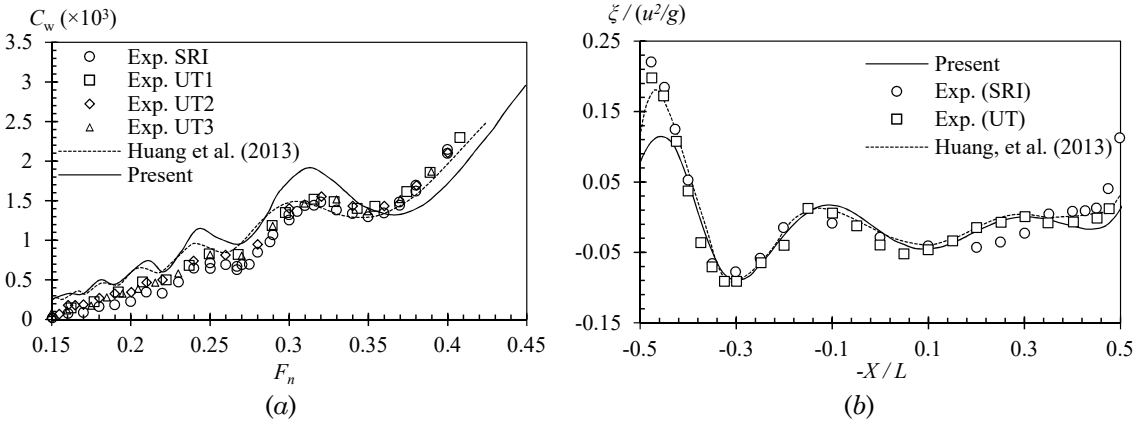

Figure 2.4: Validations of the present results. (a) Wave-making resistance coefficient C_w; (b) Wave profile along the Wigley III hull at $F_n = 0.25$. The separation distance is $d_t = 5.0b$. Validation of the numerical model in shallow water

2.4 Results and discussions

2.4.1 Effect of B_d and H

In this section, only the steady effects of a false bottom are discussed. It indicates that the false bottom covers the full length of the tank. Based on this assumption, the BVP can be treated as a steady problem, and all the quantities, including the velocity potential and the pressure, are time-independent. The parameters which determine the false-bottom effect will include the breadth B_d (or non-dimensional breadth B_d/B_t) and submerged depth H (or non-dimensional submerged depth H/D) of the false bottom, and the towing speed of the ship model U (or non-dimensional speed , which is called Froude number F_n). B_d/B_t varies from 0 to 1, in which B_d/B_t=0 indicates the false bottom doesn't exist, and B_d/B_t=1 indicates the false bottom covers a full breadth of the tank. H/D varies from 1 to infinite, in which H/D =1 indicates the under keel clearance (UKC) is zero, and $H/D = inf.$ indicates deep water. The Froude number varies from 0.1 to 0.7, which covers the most common towing speeds. Before quantifying the effect of false-bottom breadth, we have to find the cases that the false bottom with the full-breadth (B_d/B_t=1) as the standard criterion. In the next few sections, the results at B_d/B_t=1 will be used as a comparative database. Figure 2.5 shows the calculated wave-making resistance coefficient C_w of a Wigley model moving at different H/D. The results show that the wave-making resistance is heavily affected by the water depth. As the water depth decreases, the amplitude of the wave-making resistance coefficient increases rapidly, and the peaks of C_w shift towards lower Froude numbers. These peaks usually appear at the critical speed range, where the water depth Froude number approaches 1.

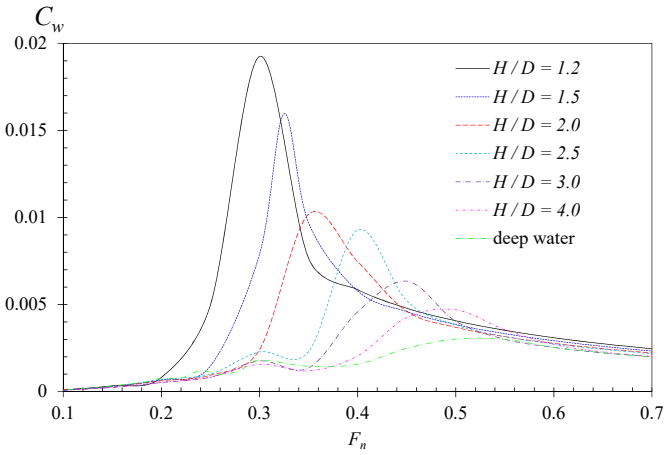

Figure 2.5: Comparison of wave-making resistance coefficient C_w at different H/D when the false bottom covers a full tank breadth.

Figure 2.6 shows the results of the wave-making resistance coefficient at different false-bottom breadths. Two typical submerged depths are studied here, H/D =4.0 and 10.0, which represent the boundary between deep and shallow water and (infinite) deep water, respectively. It can be concluded from Figure 2.6 (a) that in infinite deep water (H/D = 10.0), the effect of the false bottom's breadth is minimal. The differences are mainly observed at the peak region of C_w curves, with the Froude number ranging from 0.5 to 0.7. However, the false-bottom effects are more critical at the boundary of shallow water ($H/D = 4.0$). The results in Figure 2.6 indicate that, when conducting shallow water tests by using a false bottom facility, the test results are susceptible to the breadth of the false bottom near the critical speed. It can also be found that the difference of C_w induced by the limited-breadth of the false bottom varies with the towing speed. At low and very high Froude number ($F_n < 0.4$ and $F_n > 0.8$), the test results are less sensitive to the breadth of the false bottom. Particular attention should be paid to the shallow water tests in the near-critical region at $0.8 < Fh < 1.2$, ($F_h = U/\sqrt{gH}$ is the water depth Froude number). The test results are significantly affected by the breadth of the false bottom.

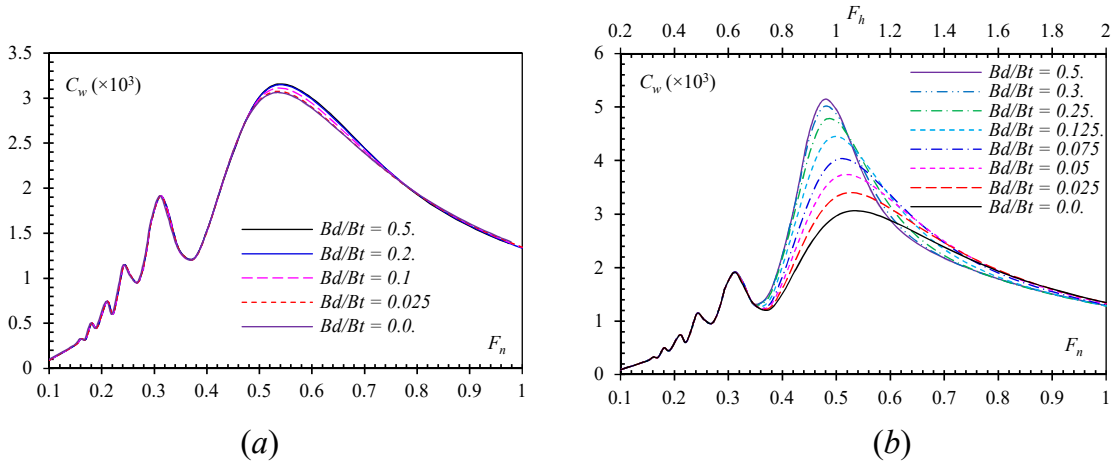

Figure 2.6: Comparison of wave-making resistance coefficient at different B_d/B_t. (a) H/D = 10.0; (b) H/D = 4.0.

2.4.2 False-bottom effect contour

It is clearly shown in Figure 2.6 that all of the three parameters $(H/D, B_d/B_t, and F_n)$ play an important role when determining the false-bottom effect. In this section, we will investigate the false-bottom effect induced by the combination of all these three parameters. To quantify the test errors (in percentage) induced by the limited breadth of the false bottom, we define a test error coefficient C_{rw} based on the wave-making resistance as following:

$$C_{rw} = \frac{C_w^{B_d/B_t} - C_w^{inf}}{C_w^{inf}} \times 100\% \tag{2.13}$$

where $C_w^{B_d/B_t}$ is the wave-making resistance coefficient Cw at B_d/B_t, and $C_w^i nf$ is the wave-making resistance coefficient by using a full-breadth bottom (B_d/B_t = 1) in the same water depth as $C_w^{B_d/B_t}$. It has been shown that the shallow water effects become very critical at $H/D < 4$ (Vantorre, 2003). Hence, we consider the effect of the false bottom at a depth ranging at $1.2 < H/D < 3.4$. Figure 2.6 shows that the difference between the results at Bd/Bt = 0.3 and B_d/B_t = 0.5 is negligible for most of the Froude numbers. Therefore, the present study only investigates the false bottom effect at $B_d/B_t < 0.35$. Particularly, $B_d/B_t = 0$ indicates the results in a given water depth without a false bottom. Table 2.3 lists the non-dimensional parameters of all test cases.

Table 2.3: Test cases of the non-dimensionalised parameters

Test items	Value range
B_d/B_t	0.0-0.35
H/D	1.2-3.4
F_n	0.06-0.4

Figure 2.7 presents the 3D contour of the error coefficient C_{rw} as a function of the non-dimensional false bottom depth H/D and non-dimensional breadth B_d/B_t. Figure 2.7 (a) to (f) show the results under subcritical speed $F_h < 0.73$ ($F_h = 0.73$ is based on the minimum water depth at $H/D = 1.2$). The false bottom effect is minimal in most of the areas and the test error C_{rw} will not exceed 10% in all test cases. It can be concluded that when conducting ship model tests at speed below $F_h < 0.75$, the false-bottom effect is small ($< 10\%$). As long as the breadth of the false bottom is larger than 10 times the ship breadth, the test results by using the false-bottom facility can represent the real shallow water and the deviation will decrease with increasing width of the false bottom. This conclusion is consistent with the wave-making resistance shown in Figure 2.6 (b) when $F_h < 0.75$.

As F_h gradually approaches the critical speed ($F_h = 1$), as shown in Figure 2.7 $(g)-(i)$, the test error coefficient C_{rw} increases rapidly. At $F_h = 0.91$, as shown in Figure2.7 (g), the maximum error caused by the false bottom effect can reach 80%. However, these errors are mainly concentrated in the lower-left corner where $H/D < 1.8$ and $B_d/B_t < 0.1$. As long as the breadth of the false bottom is larger than 8 times of the ship breadth ($B_d/B > 8$), the false-bottom effect can be neglected.

As F_h becomes larger than critical speed ($F_h > 1$), which for displacement ships is only a theoretical condition, as shown in Figure 2.7 (h) and (i), the false-bottom effect is expanded to cover a larger area. In order to get accurate shallow water test result without false-bottom effect, the breadth of the false bottom should be at least 15 times as that of the ship ($B_d/B > 15$, or $B_d/B_t > 0.25$), It should be noted that there are two sensitive regions in these two figures, presented in red and blue in the contour figure. These two regions (the red region is positive and blue region is negative) represent a very large test error induced by the false bottom. It can be explained from the results shown in Figure

2.5. It can be found that when the speed of the advancing ship is at the supercritical speed, the wave-making coefficient C_w has a decreasing trend until reaching a constant value. Due to the phase lag of the peaks at different H/D, the values of the C_w at deeper water may be larger than that in shallower water at the same speed.

In general, the results seem to agree well with the recommendations issued by ITTC in their procedure 7.5-02-06-02 Captive Model Test. The test speed should be limited to 80% of the critical Froude number:

$$F_{h,crit} = \left[2sin(\frac{arcsin(1-m)}{2})\right]^{\frac{3}{2}} \tag{2.14}$$

and the influence width,

$$y_{infl} = 5B(F_h + 1) \tag{2.15}$$

which represents the lateral reach needed to avoid restricted water effects, also seems to provide a safe limit for the lateral range of a false bottom, which needs to be larger at higher test speeds and decreasing water depths, hence, at increasing depth Froude numbers.

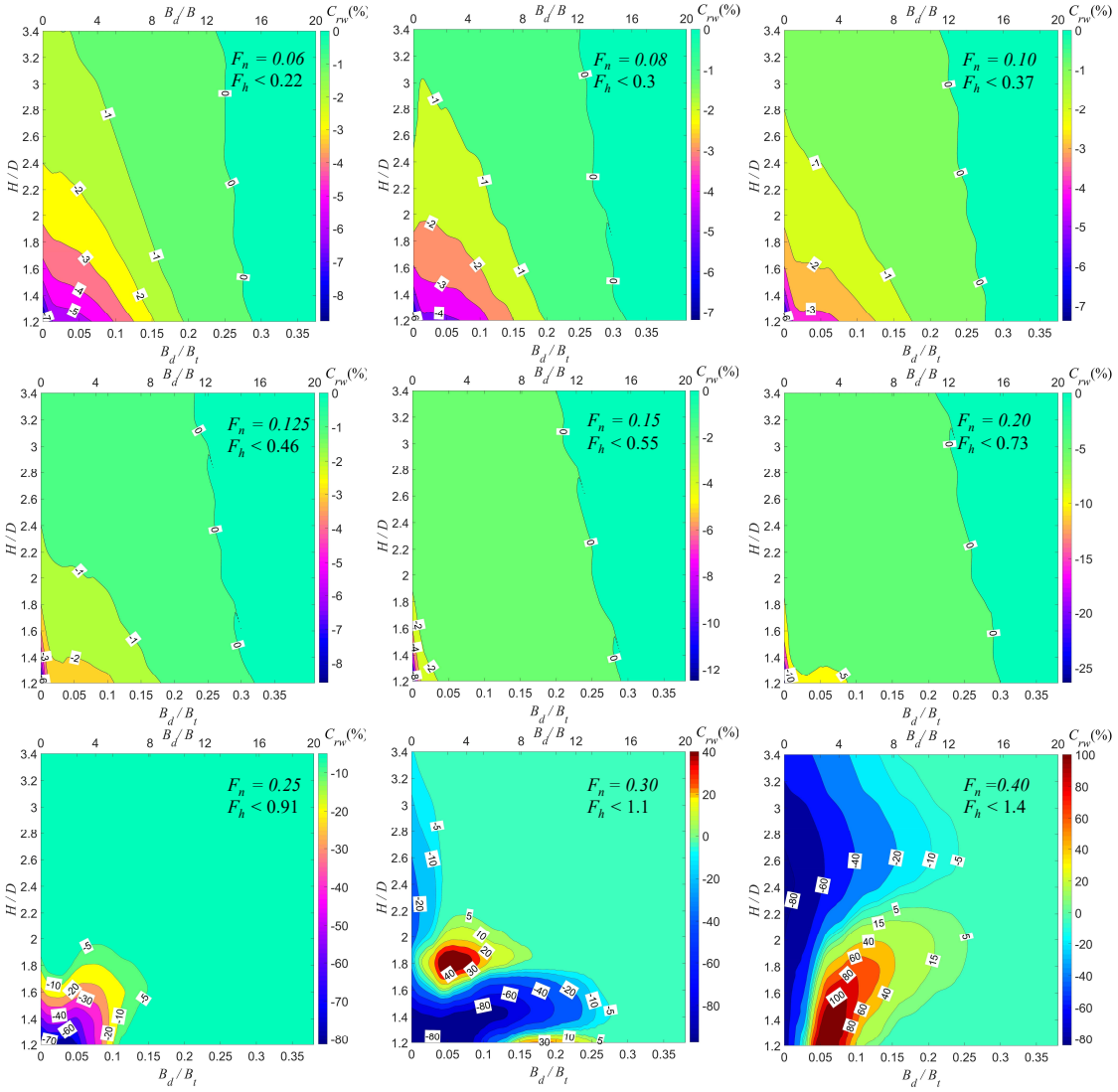

Figure 2.7: 3-D surface contour of the error coefficient C_{rw}w as a function of H/D and B_d/B_t. The upper x-axis in each figure is the false bottom breadth to the ship breadth ratio.

2.5 Summary

The false bottom facilities installed in a towing tank can improve the efficiency to measure the hydrodynamic forces of a ship moving in the shallow water. However, our understanding of the configuration and size of the false bottom is limited as concerned. It is important to quantify the false-bottom effect before the false bottoms are widely equipped in towing

tanks. In our numerical study, we investigate the steady false-bottom effect. If the false bottom is infinitely long (the same length as the towing tank), the false-bottom effects can be neglected when the breadth of the false bottom is larger than 15 times of the ship breadth ($B_d/B > 15$). The presently proposed influence width formula by the ITTC, $y_{infl} = 5B(F_h + 1)$, proposes a safe estimation of the necessary width of the false bottom and suggests a false bottom breadth of 15 times the ship breadth at $F_h = 0.5$.

Chapter 3

Steady hydrodynamic interaction between multiple moving bodies

3.1 Introduction

Pioneering studies have provided fundamental insight into the interactions between a group of animals travelling in formation. The studies on ducklings swimming in formation (Fish, 1994, 1995), fish in schools (Weihs, 1973) and birds flying in a 'V' formation or single-file line (Badgerow and Hainsworth, 1981; Lissaman and Shollenberger, 1970; May, 1979; Portugal et al., 2014; Weimerskirch et al., 2001) have found the energy consumption of individuals during group locomotion could be reduced. The 'aid' that the animal acquired from its companions varies by species. For schooling fish and flying birds, the downwash wake produced by a leader may be utilized by its followers as a propelling aid (Cutts and Speakman, 1994; Hainsworth, 1987; Hummel, 1983; Liao et al., 2003; Maeng et al., 2013; Portugal et al., 2014; Weimerskirch et al., 2001). However, for the ducklings swimming in formation on the free water surface, they benefit from utilizing the waves generated by the mother duck. Inspired by the behaviour of animals in formation, human runners and cyclists use pace lines as the most important race tactic. By traveling in a group, the racing cyclists can increase their speed about $0.9 - 1.8m/s$, while runners can improve about $0.1m/s$ (Blocken et al., 2013; Broker et al., 1999; Kyle, 1979; Olds, 1998). These studies shed a light on the performance of human competitive swimmers. Can the follow-

ing swimmers (referred to as the 'drafter' hereafter) benefit from the wakes of the leading swimmers (referred to as the 'leader' hereafter), thus reducing the drag and conserving the energy cost? Here we study the hydrodynamic interaction between two or three swimmers swimming at the same speed and explain the interaction in terms of the wave interference phenomenon.

For a single competitive swimmer, the drag (resistance) is considered to be one of the most important factors which determine his/her swimming performance. In most of the competitive swimming styles (apart from butterfly stroke), the total drag R_T of a swimmer is mainly made up of three components: wave drag R_w due to wave-making, and skin-friction drag R_f due to fluid viscosity, and pressure drag R_p arising as a result of distortion of flow outside of the boundary layer (Toussaint and Truijens, 2005). Of course, the spray could also induce a drag. But the spray drag is only pronounced in butterfly stroke. In competitive swimming, success or failure is usually measured in seconds (long course) or even in hundredths seconds (short course). Therefore, reducing the drag would improve performance. Most of the studies on drag reduction focus on swimmer's body position (Cortesi et al., 2014; Marinho et al., 2009; Zaidi et al., 2008), morphology (Huijing et al., 1988; Kjendlie and Stallman, 2011), swimming technique (Berger et al., 1995; Bober and Czabanski, 1975; Counsilman, 1968; Maglisho, 1982; Toussaint and Beek, 1992) and swimwear technology (Cortesi et al., 2014; Gatta et al., 2013; Mollendorf et al., 2004; Oeffner and Lauder, 2012; Toussaint et al., 1989; Toussaint et al., 2002a). Particularly, the skin-friction drag can be reduced by 2 to 10 % according to Toussaint et al. (Toussaint et al., 2002a) and Koeltzsch et al. (Koeltzsch et al., 2002). Considering the contribution of the skin-friction drag component to the total drag is up to 5 % given the high Reynolds numbers ($> 10^5$) that occur during swimming (Polidori et al., 2006; Toussaint et al., 1988), the drag reduced by wearing fast-skin suits is non-significant comparing with the wave drag component. The contribution of the other two drag components depends highly on gliding depth. Lyttle et al. (Lyttle et al., 1999; Lyttle et al., 1998) found that there was no significant wave drag when a swimmer was gliding at least 0.6 m underwater. However, the wave drag increases quickly as the swimmer swims closer to the free water surface. It contributes around 50 to 60 % to the total drag force in elite swimmers when swimming

at the surface (Vennell et al., 2006). It indicates that if we are able to minimize the wave drag, the total drag can be reduced significantly and the performance of the swimmers can be improved consequently.

The wave drag is associated with the waves generated by an advancing swimmer. To reduce the wave amplitude, one effective way is to improve the swimmer's technique. The examples include increasing gliding depth, as mentioned earlier, changing breaststroke technique (Bober and Czabanski, 1975), and optimizing head or finger positions (Cortesi and Gatta, 2015; Marinho et al., 2009; Vilas-Boas et al., 2015). Alternatively, a swimmer (drafter) may 'ride' the waves generated by his/her adjacent competitors (leaders). By positioning drafter's fore part in wave trough and aft part in wave crest, the wave-cancellation effect occurs, which will reduce the waves generated by the drafter and minimize the drag. The drag reduction of a drafter has been confirmed by experiments by Chatard and Wilson (Chatard and Wilson, 2003). It has also been confirmed in naval architecture that the wave-cancellation effect is beneficial for drag reduction of multihull vessels (Faltinsen, 2005; Soding, 1997; Tuck and Lazauskas, 1998). To demonstrate this wave-cancellation effect, we calculated the waves generated by a single translating source point (Figure 3.1 (a)), and the waves generated by three source points in an optimal V-shape configuration (Figure 3.1 (b)). The transverse waves generated by the two drafters are partly cancelled by travelling in the leader's wake. As a result, the wave energy propagated to the fluid domain is conserved. When this wave-cancellation effect occurs among multiple swimmers, the reduced wave energy is equivalent to the energy saved by the drafter. Although the waves generated by a swimmer's three-dimensional body are much more complicated, as shown in Figure 3.1 (c), the wave interference phenomenon can be interpreted by the same principle. In this Chapter, the swimmer's positions during the moving are keeping constant, so that all the test cases are steady.

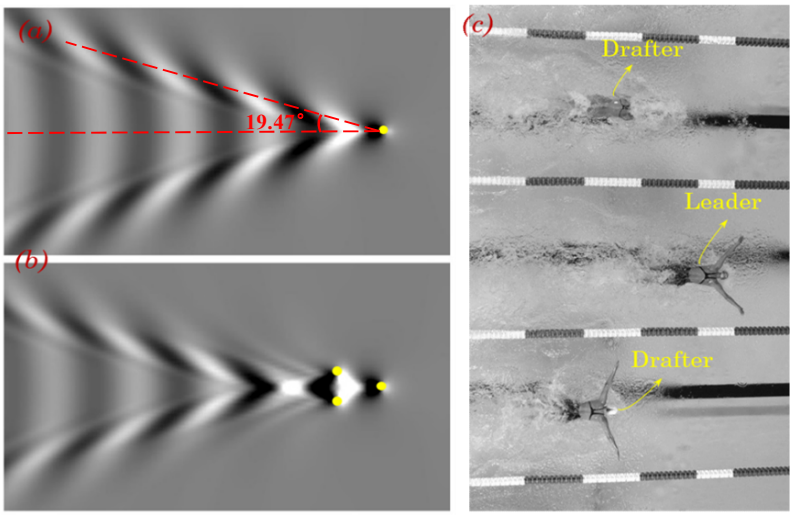

Figure 3.1: (a) The wave pattern generated by a single source point submerged at $H = 0.3U^2/g$; (b) destructive wave pattern generated by three source points submerged at $H = 0.3U^2/g$ in a V-shape configuration; (c) the formation of three swimmers in competitive swimming.(https://accidentalokie. files. wordpress. com/2012/07/11239827-essay.jpg)

3.2 Methods

In this Chapter, we are only interested in the wave drag component. No attempt is made here to analyse the other drag components due to the viscosity of the fluid. The main purpose of this Chapter is to quantify the drag-reduction in formation swimming and find the mechanism of the hydrodynamic interaction between human swimmers. To make the goals achievable, we make the following assumptions:

1. The skin-fictional drag R_f and pressure drag R_p of a swimmer in formation swimming keep the same as those of the same swimmer swimming solely at the same speed. It is well known that the skin-fictional drag R_f and pressure drag R_p are mainly determined by three factors: the speed U, the area S_b and the shape (or drag coefficient C_d) of the swimmer's immersed body surface. For the same swimmer swimming at the same speed, these three factors can be regarded as the same in single and formation swimming. Therefore, the difference in total drag in single and formation swimming is mainly caused by wave-making. This assumption coincides with the theory adopted by naval architects in catamaran design (Soding, 1997; Tuck

and Lazauskas, 1998).

2. The swimmer, either the drafter or the leader, is assumed to be a rigid and smooth body. The local movement of different parts of the body is not taken into account. The flexibility of the swimmer's body and the local movement of different body parts will definitely bring changes to the drag. However, this effect is consistent in single and formation swimming. Thus, this assumption will not violate the relative drag-reduction.

3. The gliding depth keeps constant. Neither sinkage nor trim will be considered in our calculations.

4. The swimmers are assumed to swim in open water. No attempts are made here to calculate the wave absorbing effect by lane ropes. As a result, the hydrodynamic interaction predicted in this study will be amplified.

5. Only the primary characters of the swimmer's body shape are reflected in our 3D model. The detailed geometry, e.g. fingers, hands, ears, is not considered in the calculation.

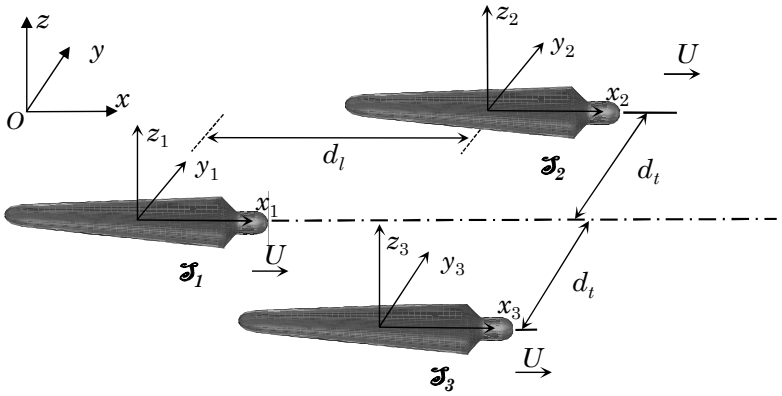

Figure 3.2: Coordinate systems of two swimmers in open water.

A 3D potential flow theory, which is widely used in ship hydrodynamics, can be used in the present study to calculate the wave drag of a swimmer. It should be noted that the drafter S_1 and leader S_2, S_3 are assumed to swim at the same speed U and the same

direction in formation swimming. Thus, the overtaking or encountering situation will not occur. Two kinds of reference systems are established with the global earth-fixed $O-xyz$ and local body-fixed $o-x_iy_iz_i$, (i=1, 2, 3...) references in Figure 3.2. The lateral and longitudinal separation distance between the drafter S_1 and leader S_2 is defined as d_t and d_l, respectively. The depth of the water is 2 m, which can be regarded as deep water in the calculations. The velocity potential is time-independent in the moving frame. It implies the hydrodynamic interaction can be treated as a steady problem, as the swimming speed is constant. In this simulation, the longitudinal separation d_l is measured in body-fixed frame on Leader swimmer.

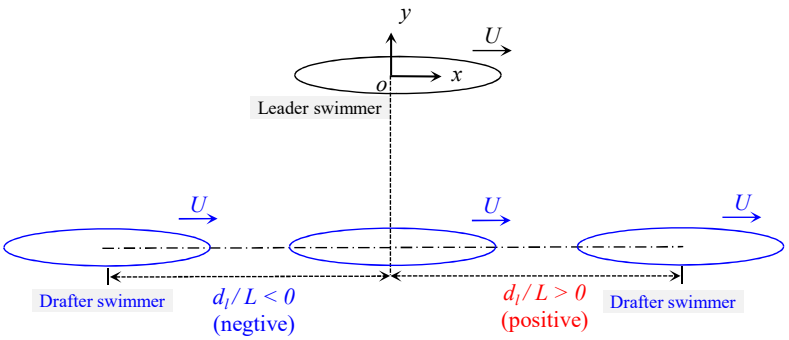

Figure 3.3: Definition of the sign d_l/L corresponding to the drafter position.

Based on the above assumptions, the fluid domain can be described by using a velocity potential φ. Furthermore, if the water is assumed to be incompressible, it follows that the velocity potential φ has to satisfy the Laplace equation:

$$\frac{\partial^2\varphi}{\partial x^2}+\frac{\partial^2\varphi}{\partial y^2}+\frac{\partial^2\varphi}{\partial z^2}=0 \tag{3.1}$$

By combining the dynamic and kinetic free surface conditions, the time-independent linearized steady free surface condition (Newman, 1977) can be written as:

$$U^2\frac{\partial^2\varphi}{\partial x^2}+g\frac{\partial\varphi}{\partial z}=0 \tag{3.2}$$

The body surface boundary condition follows from the requirement that there be no flow through the body surface. This means:

$$\frac{\partial \varphi}{\partial n} = Un \tag{3.3}$$

where $n = (n_1, n_2, n_3)$ is the unit normal vector inward on the wetted body surface. Besides, a radiation condition is imposed on the control surface to ensure that waves vanish at upstream infinity:

$$\varphi \longrightarrow 0,\ \zeta \longrightarrow 0\ as\ \sqrt{x^2 + y^2} \longrightarrow \infty \tag{3.4}$$

A Rankine source panel method (Hess and Smith, 1964) is used to solve the boundary value problem in Equations. 3.1-3.4. The details of numerical implementation are demonstrated in Yuan et al. (2015c). The same in-house developed multibody hydrodynamic interaction programme MHydro, which has been extensively validated against ship model tests, is deployed in the present study to predict the interactions in a swimming pool. Special care should be taken to implement a suitable open boundary condition to satisfy Equation. 3.4. In numerical calculations, the computational domain is always truncated at a distance away from the moving body. A 2nd order upwind difference scheme is applied on the free surface to obtain the spatial derivatives. In this way, the waves could propagate to the far-field without reflection. Once the unknown potential φ is solved, the steady pressure distributed over the ship hull can be obtained from linearized Bernoulli's equation:

$$p = \rho U \frac{\partial \varphi}{\partial x} \tag{3.5}$$

By integrating the pressure over the hull surface, the forces (or moments) can be obtained by

$$F_i = \iint_S p n_i ds,\ i = 1,\ 2,\ ...,\ 6 \tag{3.6}$$

The wave drag R_w is equivalent to the force component in the x-direction ($i = 1$). The wave elevation on the free surface can be obtained from the dynamic free surface boundary

condition in the form

$$\zeta(x, y) = \frac{U}{g}\frac{\partial \varphi}{\partial x} \tag{3.7}$$

3.3 Description of the swimmer model

In numerical modelling of animal swimming, the animal's 3D body shape is usually idealized as some simplified geometry. This approach was used by Lang (Lang, 1966), defining the body shape of a dolphin as an ellipsoid with an added tail region. Compared with the dolphin body, the shape of the swimmer model is much more complex. Based on Tuck and Newman's slender body theory (Tuck and Newman, 1976), Weihs (Weihs, 2004) modelled a dolphin as an oblate ellipsoidal shape with an aspect ratio of about 6, in order to investigate the hydrodynamics of dolphin drafting. Westerweel et al. (Westerweel et al., 2016) conducted measurements of a scaled swimmer model by using a simplified model with the arms alongside the body. Similar simplification is made for the present swimmer model. The 3D numerical swimmer model is shown in Figure 3.4 (b). It should be noted that the total wet body surface of the numerical swimmer model is $S = 1.65$ m^2 without considering the different swimming movements. It is smaller than the area of a real competitive swimmer ($S = 1.9$ m^2) when the arms and legs are fully exposed to the water. The computational domain of the numerical model is shown in Figure 3.4 (a). All the boundaries are discretized into a number of quadrilateral panels with constant source density. To capture the far-field waves propagating downstream, the free surface is truncated at least $7L$ behind the swimmer. The water depth of the swimming pool is 2 m.

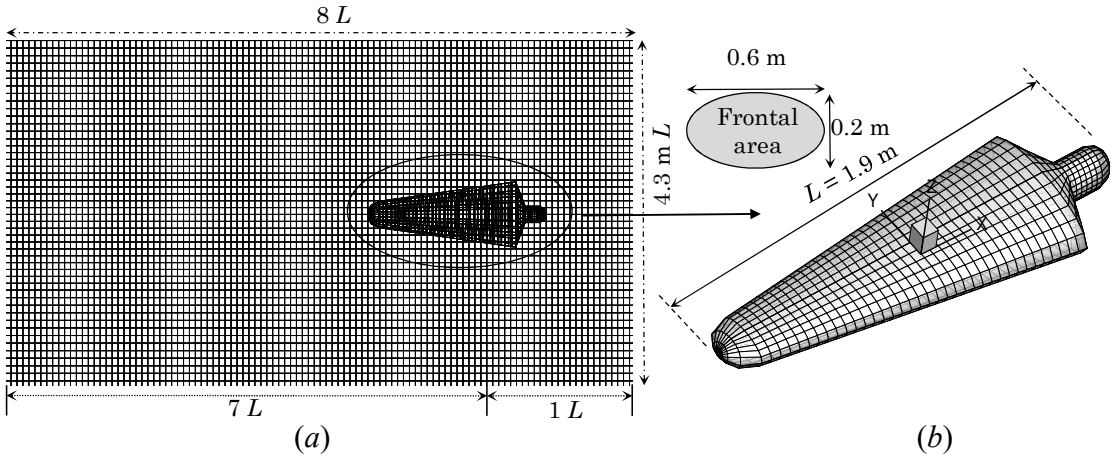

Figure 3.4: Panel distribution on the computational domain. In a single swimmer case, there are 13717 panels distributed on the entire computational domain: 2141 on the wetted body surface, 11576 on the free surface. The free surface is truncated at 1L upstream and 7L downstream with regard to the body-fixed frame on the swimmer model. The local coordinate system is fixed on the moving body with its positive x-direction pointing towards the head, positive z-direction pointing upwards and $z = 0$ on the undisturbed free surface.

The main dimension of a swimmer is shown in Table 3.1. The length of the swimmer model is 1.9 m. The frontal area with the shape of an ellipse is equal to 0.6 $\times$ 0.2 m^2. The surface area of the model is shown in Table 3.1. As for the integral boundary equations calculated above the body surface, it is significant to match the surface area of the model as same as the real human. A general surface area of the real human is about 1.9 m^2 without considering the gesture adopted in this situation that some surface is superposition. Comparing the surface area of the model with the real human, it is reasonable for our model surface area that is 1.65 m^2.

Table 3.1: Dimensions of swimmer

Length, L (m)	1.9
Breadth, B (m)	0.3
Draught, D (m)	0.2
Total area, S (m^2)	1.65

3.4 Results and discussions

To validate the accuracy of the code for the simulation of the hydrodynamic problem between two swimmers, the experimental data measured by Oltman (Oltmann, 1970) and the numerical results calculated by using a high-order panel method (Xu et al., 2016) are compared with the present calculations, as shown in Figure 3.5. The calculation starts at the position of negtive $d_l/L = -3$ and ends at the position of $d_l/L = 3$ by C_2, which is shown in Figure 3.5 (a). In Figure 3.5 (b), the positive sign of the wave drag coefficient C_w denotes as attractive. Generally, the present calculations show a good agreement with the measurements, as well as with Xu's numerical results. An interesting finding is that a very large positive wave drag (the force is pointing towards the moving direction) can be observed at $d_l/L = 0.7$. It implies that when an object (drafter) is located in the wake of the other object (leader), the hydrodynamic interaction can be utilized by the drafter as a propelling aid. Similar findings were also observed in laboratory experiments of two ships travelling side-by-side (Vantorre et al., 2002; Yuan et al., 2015a). It should be noted that the hydrodynamic interaction between two cylindroids travelling at a low Froude number in this case study is dominated by the near-field waves. In competitive swimming, the Froude number of swimmers is much higher (around 0.4 - 0.5). As a result, the far-field waves (or Kelvin waves) could be the most important factor that determines the interactive forces. This will be discussed later.

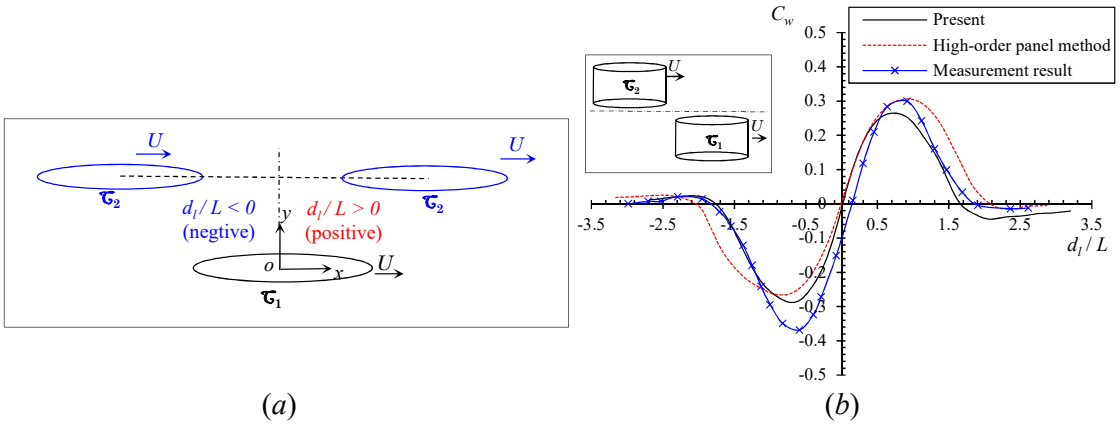

Figure 3.5: The wave drag (positive forward) on cylindroid C_1 when it is moving parallelly with C_2 located in different position at F_n= 0.217. The negative d_l values denote that C_2 is on the downstream side of C_1. As C_2 moves to the upstream side, d_l/L becomes positive. The red dash curve indicates the numerical results calculated by using a NURBS-based high-order panel method (Xu et al., 2016a). The blue crosses indicate the experimental results measured by Oltman (Oltmann, 1970). The present calculations are shown in black solid curves.

3.5 Wave drag of a single swimmer

The total drag of a single swimmer has been extensively investigated both numerically and experimentally. However, only a few studies have been conducted to quantify the wave drag component. The contribution of the wave drag to the total drag varies greatly in these studies. Vorontsov and Rumyantsev (Vorontsov and Rumyantsev, 2000) suggested that 5% of drag was due to waves at 2 m/s. Toussaint et al. (Toussaint et al., 2002b) found the wave drag amounted to 12 % of the total drag. These studies significantly underestimate the wave drag contribution. It was assumed that the wave drag was negligible when the swimming speed was below 1.6 m/s ($F_n < 0.35$). However, it is well known in naval architecture that for a surface vessel, the wave drag becomes dominant at $F_n > 0.3$ (Schultz, 2007). More specifically, the wave drag contributes up to 55 % of the total drag at $F_n = 0.35$ for a surface-piercing body. The contribution increases to more than 70 % at $F_n = 0.45$. It should be noted that the wave drag of a surface-piercing body is larger than that of a fully submerged one. Even for a fully submerged body, both experimental measurements and numerical calculations confirm that the wave drag varies

a lot at different submerged depths, as shown in Figure 3.6. In order to obtain reliable wave drag results, the submerged depths must be taken into account. Lyttle et al. (1998) investigated the effect of submerged depth and velocity on drag during the streamlined glide. Their experimental results suggest that at 2.2 m/s, the total drag is 20 % lower at 0.6m depth than at the surface. The measurements by Vennell et al. (Vennell et al., 2006) show that the wave drag is 50-60% of the total drag on elite swimmers swimming close to the surface at 2.2 m/s, which is much higher than any previous estimate. All the experimental studies mentioned above obtain the wave drag indirectly by subtracting the skin and form drag from the total measured drag. The skin and form drag is assumed to be equal to the total drag when the submerged depth is very large (Vennell et al., 2006). When the swimming speed is near 1.6 m/s (Toussaint et al., 2002b), the wave making resistance has already significantly occur at that speed. However, in ship hydrodynamics, it is straightforward to calculate the wave-making resistance (or the wave drag) by a well-established potential flow theory. As the viscosity of the fluid is not considered, the resistance calculated by solving the Laplace equation in Equation. 3.1 is equivalent to the wave drag. In the present study, the same methodology used in naval architecture will be applied to calculate the wave drag on human swimmers. The wave drag on a single swimmer is shown in Figure 3.6. When the swimmer is swimming near the free surface ($H = 0.0 \sim 0.2m$), the wave drag decreases rapidly as the submerged depth increases. The curves exhibit 'humps' and 'hollows'(which are also called amplification and cancellation effects) due to the interference between bow- and stern-waves (Yuan et al., 2018). These 'humps' and 'hollows' shift to higher velocities and become less distinct as the submerged water depth increases. For a competitive swimmer, the non-dimensional velocity (Froude number) is usually larger than 0.35. Therefore, these 'humps' and 'hollows' will not have a prominent influence on the swimmer's performance. At moderate submerged depth ($H = 0.2 \sim 0.4m$), the wave drag continues to decrease at a slower rate as the submerged depth increases. The 'humps' and 'hollows' phenomenon disappears, and the wave drag is only 10-20 % of that at H =0 m. At the submerged depth of 0.4 m or larger, the contribution of the wave drag is very small and it is usually neglected in most of the studies on human swimmers. In some experimental studies (Toussaint and Truijens, 2005;

Vennell et al., 2006), the contribution of the other two drag components (the skin-friction drag R_f and pressure drag R_p) is measured by towing the mannequin below the $H = 0.6$ m. The wave drag results of a single swimmer shown in Figure 3.6 are consistent with the experimental measurements, which will be used in the next session to non-dimensionalise the wave drag of the same swimmer when swimming alongside the other swimmers.

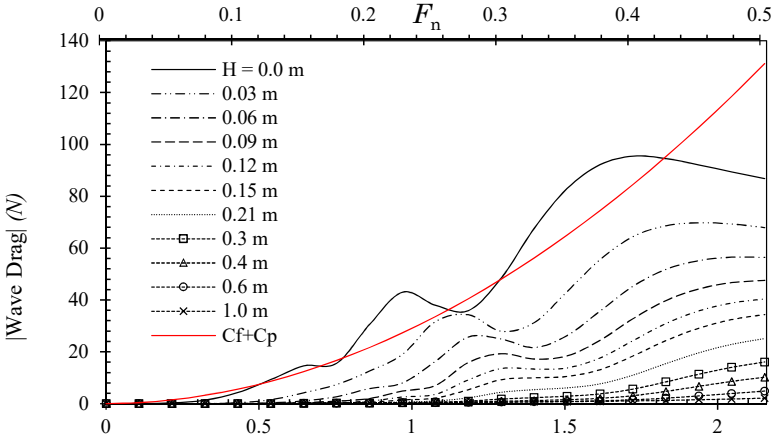

Figure 3.6: Absolute value of the wave drag of a single human swimmer. The black curves indicate the wave drag at different submerged depths. $H = 0$ indicates that the highest point on the body surface is on the free surface. The red curve indicates the sum component of the frictional and pressure drag.

To assess the contribution of the wave drag to the total drag, the contribution of the other two drag components, namely the skin-friction drag R_f and pressure drag R_p, should be quantified. The skin-friction coefficient can be determined by the ITTC 1957 correlation line for turbulent flow (ITTC, 2017).

$$C_f = \frac{0.075}{(\log(\mathrm{Re}) - 2)^2} \tag{3.8}$$

where $Re = \rho v L/\mu$ is the Reynolds number of the body, v is the kinematic viscosity of the water. The skin frictional resistance then can be calculated by

$$R_f = 0.5\rho U^2 S C_f \tag{3.9}$$

The form drag R_p is

$$R_p = 0.5\rho U^2 A_p C_p \tag{3.10}$$

where C_p is the form of drag pressure efficient. For an elliptical bluff body, C_p is defined as 0.3 (Webb et al., 2011). A_p is the projected area in the y-z plane. The curve of frictional and pressure drag in Figure 3.6 shows the increased drag with speed. When a swimmer is swimming at the free water surface ($H = 0$ m), the contribution of the wave drag and the other two components are of similar magnitudes at low swimming speed ($U < 1.3$ m/s). At medium speed (1.3–1.8 m/s), the wave drag is the largest drag, contributing up to 50–60 % of the total. It coincides with the measurements by Vennell et al. (Vennell et al., 2006). At high swimming speed ($U > 1.8$ m/s), the wave drag experiences a decrease with the speed, while the frictional and pressure drag keeps increasing and gradually larger than the wave drag. As the submerged depth increases, the contribution of the wave drag drops rapidly. The results in Figure 3.6 clearly show how the submerged depth changes the wave drag and its contribution to the total drag. In the next section, all the results and discussions are based on the submerged depth of $H = 0$ m, when the swimmer is just immersed below the free water surface. No attempts are made to investigate the surface-piercing swimmers.

3.5.1 Hydrodynamic interaction between two swimmers in formation swimming

In the last section, we obtained the wave drag of a swimmer swimming alone in open calm water, which is denoted by R_{ws}. When the same swimmer swims at a certain position around another swimmer, the wave drag is denoted by R_w. The wave drag reduction coefficient can be expressed as

$$C_{DR} = \frac{R_{ws} - R_w}{R_{ws}} \times 100\% \tag{3.11}$$

The wave drag reduction coefficient C_{DR} can be used as an indicator to show the hydrodynamic interactive effect. $C_{DR} > 0$ indicates a reduction of wave drag due to the hydrodynamic interaction; $C_{DR} < 0$ represents an increase in the wave drag of a swimmer

caused by the presence of the other swimmer(s). No interaction is expected when $C_{DR} = 0$. When $C_{DR} > 100$ %, the wave drag turns to be a thrust force, which is in the same direction of moving.

First of all, we calculate the wave drag reduction coefficient when a drafter is swimming right behind a leader (the transverse separation $d_t = 0$) by varying the longitudinal distance d_l. The result of C_{DR} is shown in Figure 3.8. The drag reduction curve exhibits distinct fluctuations when the drafter swims towards the leader from $7L$ to $1L$ downstream. The amplitude of the fluctuations becomes larger as the drafter getting closer to the leader. A maximum wave drag reduction of 140 % occurs where the drafter's head is almost touching the leader's feet at $d_l/L = -1.1$, indicating the wave drag turns to be a thrust force which pulls the drafter forward. It agrees with the experimental measurements by Chatard and Wilson (Chatard and Wilson, 2003) which concluded that the optimal distance behind the leader was between 0 and 50 cm. In this position, the drafter could significantly save energy by utilizing the waves generated by the leader. However, the hydrodynamic interaction does not have a positive effect on the drafter at all positions. When the drafter lags behind the leader slightly at $d_l/L = -1.5$, this interactive effect becomes negative. The wave drag is amplified by the interactive force, which means the drafter has to consume more energy to overcome the extra resistance. It is interesting to find that the trough and crest values of C_{DR} appear alternately with a constant interval, fluctuating around C_{DR} =0. This feature of the C_{DR} curve is very similar to harmonic water waves, which have a constant wavelength. To further investigate the relationship between C_{DR} and the free surface waves, we calculated the Kelvin waves generated by the leader, which are plotted in Figure 3.8 as the background contour. The wave profile at the central line (moving path) of the domain is also shown in the same figure. These results confirm that the interval between the trough and crest of the C_{DR} curve is the same as the wavelength of the transverse Kelvin waves, which can be calculated by $2\pi U^2/g$. However, these two curves are not in phase. The maximum wave drag reduction is observed when the drafter's fore part is in the wave trough while the aft part is in the wave crest, for example at d_l/L = -1.1. The physical observations of the wave-riding behaviour of dolphins (when chasing boat waves) and ducklings (when following the mother duck) in nature

confirm the benefit of this wave-riding configuration (Fish, 1995; Williams et al., 1992). Theoretically, it can be explained by the water wave theory. The crest on the free water surface corresponds to a relatively higher pressure under the wave crest profile, while the wave trough corresponds to lower pressure. According to Equation. 3.6, the wave drag can be calculated by the pressure integral over the body surface. As the normal vector $\overrightarrow{n}$ in the fore part of the drafter is pointing backwards, a lower pressure distribution over the fore part will lead to a smaller backward force (resistance). On the other hand, the normal vector $\overrightarrow{n}$ in the aft part is pointing forwards, a higher pressure distribution over the aft part will lead to a larger forward force (propulsion), which is shown in figure 3.7.

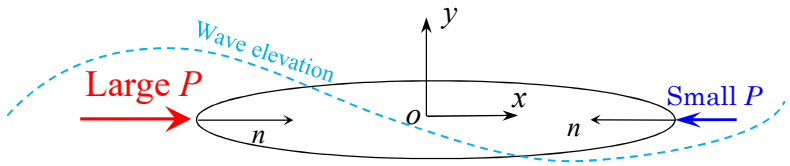

Figure 3.7: Description of the lower pressure distribution over the fore part and the higher pressure at the aft part.

If the amplitude of the thrust force integrated over the aft part is larger than the resistance integrated over the fore part, a total thrust force can be expected, which is the case shown in Figure 3.8 at d_l/L = -1.1. Conversely, if the drafter's fore part is in the wave crest while the aft part is in the wave trough, an extra resistance will be added, which gives rise to the total wave drag, as shown in Figure 3.8 at d_l/L = -3.2. The wave amplitude is damped as the waves propagate to the far-field. As a result, the amplitude of the wave drag reduction coefficient reduced as the drafter moves further away from the leader.

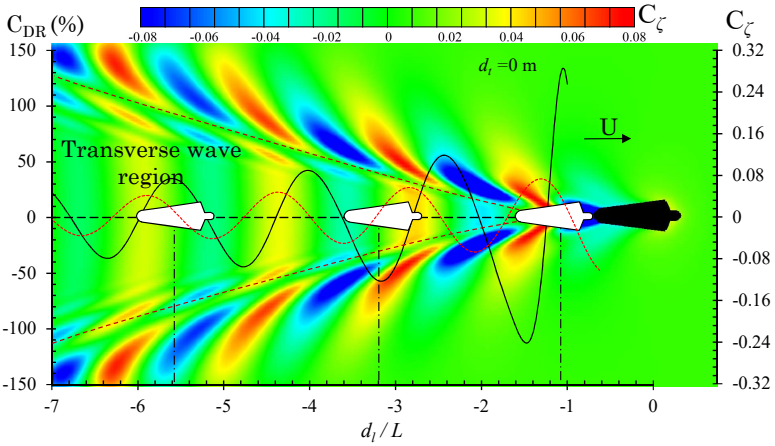

Figure 3.8: Wave drag reduction coefficient (black solid curve) when a drafter swims right behind a leader at $U = 2.16$m/s. The colour contour indicates the wave pattern generated by the leader. The red dash curve is the wave profile at the central line behind the leader. The x-axis is the non-dimensional distance d_l/L. C_ζ is the non-dimensional wave elevation, $C_\zeta = \zeta g/2\pi U^2$.

When the drafter is swimming right behind the leader, the hydrodynamic interactive force is mainly induced by the transverse wave component generated by the leader. The results in Figure 3.8 explain how these transverse waves influence the wave drag of a drafter. However, in competitive swimming, each swimmer must stay in his/her lane, swimming in parallel with a certain transverse distance dt. As shown in Figure 3.9 at $d_t = 2.5$ m, when the position of the drafter changes from -7L to -1L, the drafter has to pass through the transverse waves, the divergent waves, and eventually reach a non-disturbed region. Therefore, the hydrodynamic interaction is more complicated. Figure 3.9 shows the result of C_{DR}, where the lateral separation between the drafter and leader is $d_t = 2.5$ m. By varying the longitudinal position, the C_{DR} curve exhibits fluctuations around $C_{DR} = 0$. However, the curve does not fluctuate harmonically, especially at $-7 < d_l/L < -4.8$. This corresponds to a special region where the interference between bow- and stern-waves occurs. A maximum wave drag reduction of 55 % can be found at $d_l/L = -4.2$ where the drafter's fore part is in the wave trough while the aft part in wave crest. From the results shown in Figure 3.6, it is found that the wave drag comprises about 40 % of the total drag at $U = 2.16$ m/s. Then it can be concluded that the drafter can save up to 22 % of the total drag if he/she is located in the wave-riding position after a leader.

Of course, this conclusion is based on the open water assumption, where the lane ropes are not considered. An increased wave drag of 80 % is observed if the drafter swims at $d_l/L = -3.6$ due to undesired interaction. The amplitude of the C_{DR} curve is not as large as that shown in Figure 3.8, indicating the hydrodynamic interaction induced by the leader's transverse waves is more prominent than that induced by the divergent waves. The interactive force gradually vanishes after the drafter is completely out of the Kelvin wake. At $d_l/L > -1$, the hydrodynamic interaction can be negligible. When the drafter and leader are swimming side-by-side ($d_l/L = 0$), no hydrodynamic interaction is observed. The results shown in Figure 3.9 confirm the importance of the position in formation swimming. In competitive swimming, the drafter is supposed to be able to sense the drag difference and reposition him/herself to a drag-reduced region to preserve energy during competition.

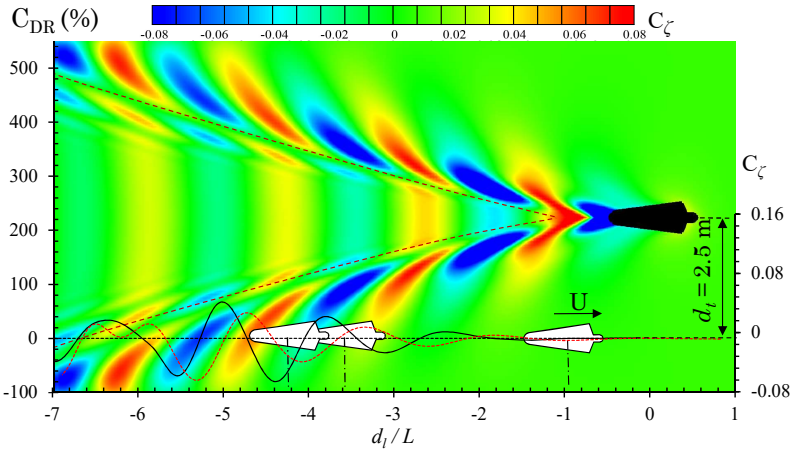

Figure 3.9: Wave drag reduction coefficient (black solid curve) of a drafter when he/she swims alongside a leader at $U = 2.16$m/s. The colour contour indicates the wave pattern generated by the leader. The red dash curve is the wave profile at the moving path of the drafter.

The lanes of the World Championship pools are usually 2.5 metres wide. If the adjacent swimmers maintain their courses at the mid-lane, the lateral separation between them is 2.5 m; this is the case showed in Figure 3.9. However, it is commonly observed in competitive swimming that the swimmers may not able to keep their course at the mid-lane. In order to find how the transverse separation alters the hydrodynamic interaction,

we calculate the wave drag reduction coefficient of a drafter at various d_t. The results are shown in Figure 3.10. Similar to the result of $d_t = 2.5$ m shown in Figure 3.9, the C_{DR} curve exhibits fluctuations around $C_{DR} = 0$. The most significant disturbance occurs when the drafter swims at the leader's divergent wave region. At different lateral separations, the drafter encounters the leader's divergent wave at a different longitudinal position. From the colour contour shown in Figure 3.10, it can be seen that as dt increases, the longitudinal position of entering the divergent wave region is shifted towards larger d_l/L. As a result, a phase shift of C_DR curves can be observed at different d_t. At small lateral separation, for example, $d_t = 1.5$-1.7 m, a minimum C_{DR} of -103 % is found in region B, while the maximum C_{DR} is found in region C. When the lateral separation increases, for example, $d_t > 1.9$ m, the maximum C_{DR} remains in region C, while the minimum value shifts from region B to region D. In a swimming competition, the most interesting position is in region C, where the drafter can experience the maximum wave drag reduction. In region C, the peak value of C_{DR} curves varies from 60 % to 70 %. The discrepancy between the peak values at different dt is not very obvious in region C, indicating that the maximum wave drag reduction is not sensitive to the lateral separation.

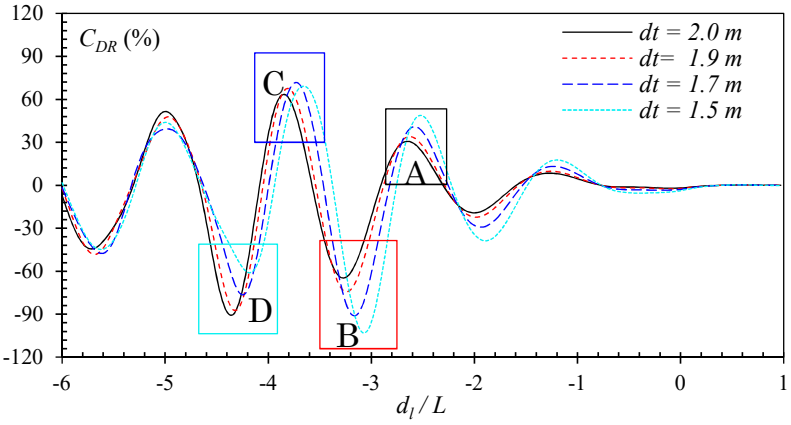

Figure 3.10: Wave drag reduction coefficient of a drafter when he/she swims alongside a leader at different transverse distances at $U = 2.0$ m/s. The x-axis is the non-dimensional longitudinal distance.

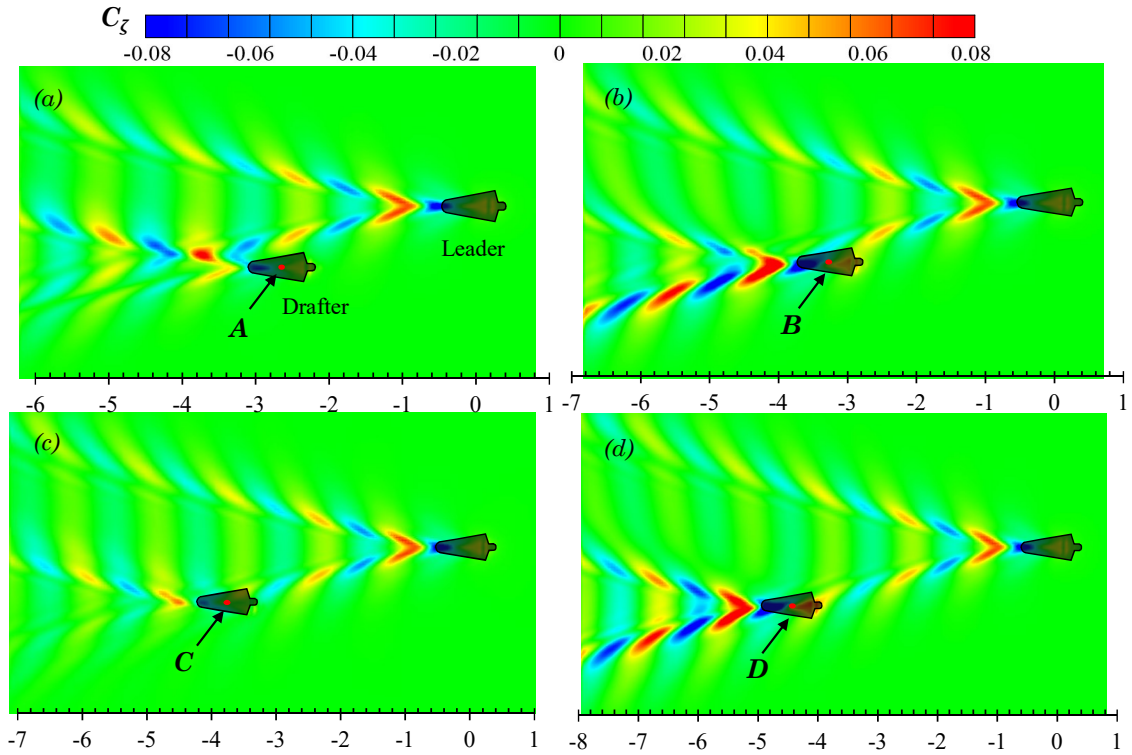

Figure 3.11: Wave patterns generated by two swimmers at $d_t = 2.0$ m and $U = 2.0$ m/s. The x-axis is the non-dimensional longitudinal distance d_l/L. Four typical positions are selected, namely $A, B, C, and\ D$, which represent the peak values in corresponding boxed regions in Figure 3.10.

The results in Figure 3.8 and Figure 3.9 show that when a drafter is located in the wave-riding position, the wave drag reduction coefficient reaches the maximum value. It can be explained by the pressure integral based on the potential flow theory, which has been explained previously. Here, the attempts are made to explain this drag-reducing and drag-increasing phenomenon from another perspective: wave interference. The work is done by a swimmer to overcome the wave drag can be transferred into the energy of the Kelvin waves on the free water surface, which is proportional to ζ^2. For a swimmer swimming alone in unrestricted water, ζ is mainly determined by swimmer's body shape, posture, speed, and submerged depth. The relative position becomes another factor that affects the free surface elevation if two or more swimmers are swimming in close proximity. The results in Figure 3.11 clearly show how the wave patterns are affected by the drafter's position. Four typical positions are selected, namely $A, B, C, and\ D$, which represent the peak

values in corresponding boxed regions of Figure 3.10. In positions *A and C*, the drafter takes advantage of the wave-riding position to achieve maximum wave drag reduction. In these two positions, a destructive wave interference phenomenon can be observed, where the waves generated by the swimmers are 180° out of phase. The starboard divergent waves of the leader are partly cancelled by the drafter's starboard divergent waves. This effect can be referred to as partial divergent wave cancellation. As a result, the free surface elevation in the starboard wake of the drafter is reduced, hence conserving energy. This wave cancellation effect has been proved to have a beneficial effect on multihull configuration in order to minimize the wave resistance of a multihull vessel (Soding, 1997; Tuck, 1987). Conversely, if the drafter is located in positions *B and D*, the starboard divergent waves generated by the swimmers are in phase. More energy is dissipated in terms of the amplified waves, which requires the drafter to do extra work in order to overcome the increased wave drag. Obviously, positions *B and D* are the most undesirable positions in formation swimming. To 'escape' from these drag-increased positions, the drafter has to generate an additional thrust to move towards positions *A and C* where the wave drag can be minimized. The portside divergent waves generated by the two swimmers propagate in parallel to the far field, and they never overlap. However, the portside divergent waves generated by the drafter could also interact with the transverse waves generated by the leader. These two wave systems have different properties in terms of propagation direction and wave length. As a result of superposition, the portside divergent waves of the drafter may be amplified (see Figure 3.11 (a) and (d)) or cancelled (see Figure 3.11 (b) and (c)). For the high-speed moving body ($F_n > 0.4$), the divergent wave energy is much higher than the transverse wave energy. Thus, the magnitude of the divergent-transverse wave interference is less than the divergent-divergent wave interference.

3.5.2 Formation swimming of three swimmers

In a swimming competition, the hydrodynamic interaction does not only occur between two swimmers. Apart from the swimmers at the first and last lanes, a swimmer usually interacts with the other two adjacent swimmers. The hydrodynamic interaction between three swimmers is very interesting. There are various possible configurations of three

swimmers in a formation, among which the V-shape configuration is of particular interest. As shown in Figure 3.2, when a drafter is located in the wake of two leaders on both sides, he/she may achieve more wave drag reduction by utilising the waves produced by two leaders. The results of C_{DR} in a V-shape configuration are shown in Figure 3.12. Similar fluctuations of C_{DR} curves are observed in V-shape formation swimming. Compared with the two-swimmer case (see Figure 3.10), the amplitudes of the C_{DR} curves shown in Figure 3.12 are much higher. For example, at $d_t = 2.0$ m, the maximum and minimum wave drag reductions are 110 % and -162 % respectively in the three-swimmer case, while in the two-swimmer case, the maximum and minimum values are 58 % and -86 %. The corresponding longitudinal separations in the three-swimmer and two-swimmer cases are consistent. The most interesting position is also found in region C, where the drafter can experience a maximum wave drag reduction of up to 110-120 %. As indicated in Equation. 3.11, when the wave drag reduction is larger than 100 %, the wave drag turns to be a thrust force, which pushes the drafter forward. The results in Figure 3.12 indicate the drafter could potentially save more energy by following two side-by-side leaders. From the results shown in Figure 3.6, it is found that the wave drag comprises about 43 % of the total drag at $U = 2.0$ m/s. Then it can be concluded that in open water conditions, the drafter can save up to 50 % of the total drag if he/she is swimming in the right position in a V-shape configuration.

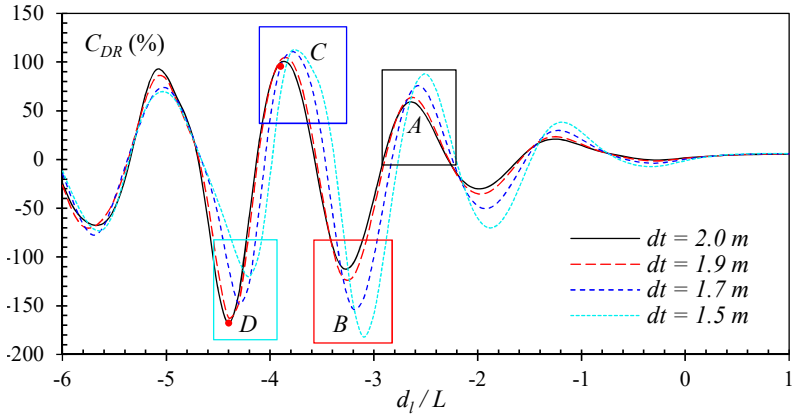

Figure 3.12: Wave drag reduction coefficient of a drafter swimming in the wake of two side-by-side leaders at both sides at $U = 2.0$ m/s. Different curves correspond to various transverse distances. The x-axis is the non-dimensional longitudinal distance between the leaders and the drafter.

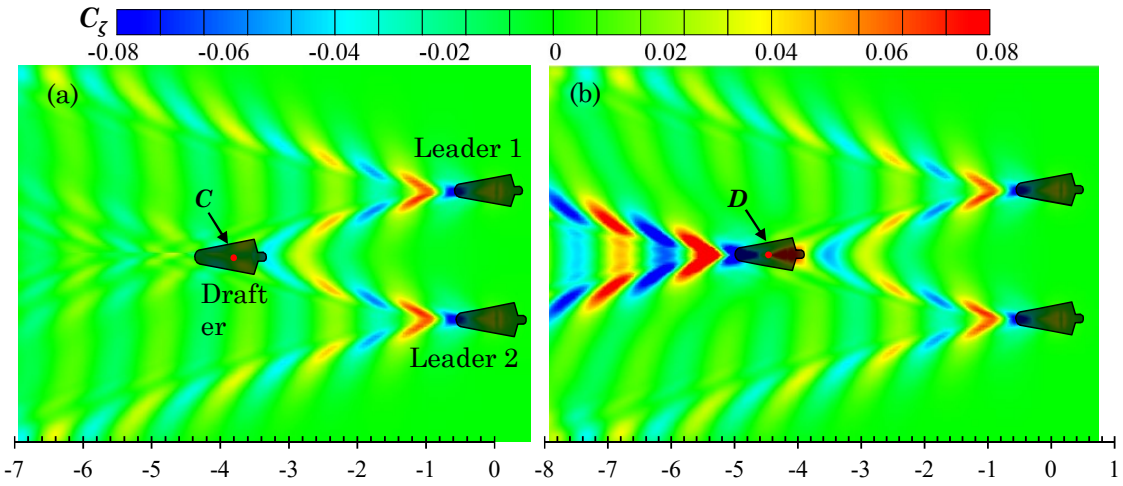

Figure 3.13: Wave patterns generated by three swimmers in a V-shape configuration at $d_t = 2.0$ m and $U = 2.0$ m/s. (a) The drafter is located at position C; (b) drafter is located at position D. The x-axis is the non-dimensional longitudinal distance d_l/L.

The results in Figure 3.12 show that the drafter can save 110 % of wave drag at $d_l/L = -3.8$ (position C). The wave drag increases 162 % when the drafter is located at $d_l/L = -4.4$ (position D). As discussed before, the wave drag reduction and wave drag increase can be explained by the wave interference phenomenon on the free water surface. Figure 3.13 compares the wave patterns generated by three swimmers in a V-shape configuration when the drafter is located at C *and* D respectively. The destructive wave phenomenon can

be observed in Figure 3.13 (a) when the drafter takes the wave-riding position. With the head and shoulders located in the troughs of the divergent waves generated by the leaders, the drafter generates a divergent wave system, which is 180° out of phase with Leader 1's starboard divergent waves and Leader 2's portside divergent waves. Because of superposition, the divergent wave system behind the drafter can hardly be observed. This effect can be referred to as full divergent wave cancellation. Compared with the partial divergent wave cancellation effect in two-swimmer formation swimming, it is obvious that the full divergent wave cancellation could achieve a higher wave drag reduction (almost twice), hence saving more of the drafter's energy. On the contrary, if the drafter is located in position D, the divergent waves generated by the three swimmers are in phase. The amplified waves will dissipate more energy, which requires the drafter to do more work in order to overcome the increased wave drag. The results in Figure 3.12 and Figure 3.13 confirm that the interaction between three swimmers could be more significant than that between two swimmers.

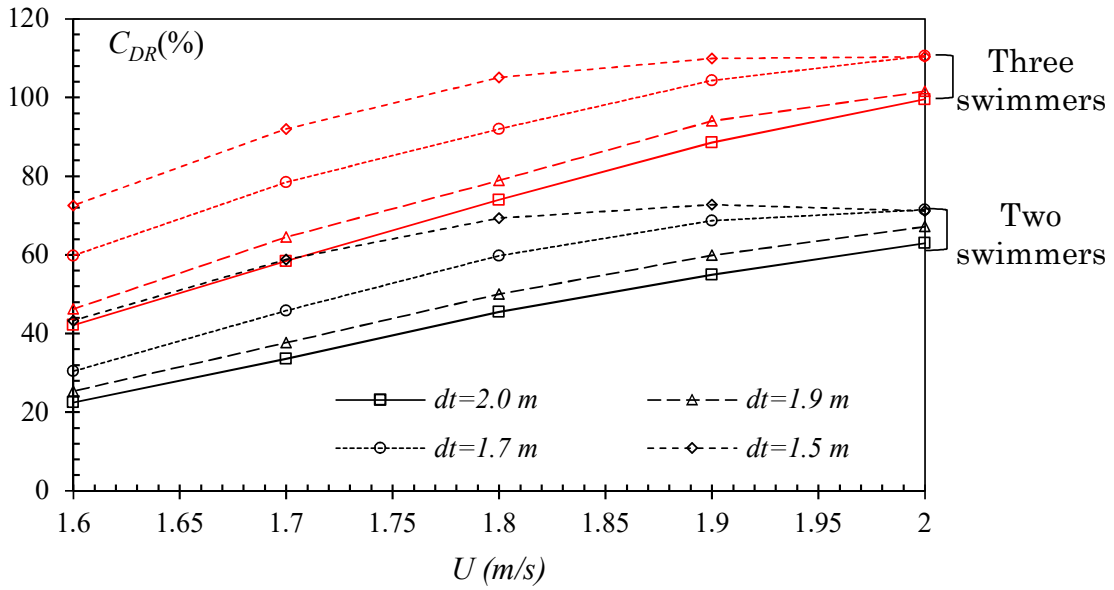

Figure 3.14: Maximum wave drags reduction coefficient of a drafter in formation swimming. The black curves indicate the maximum C_{DR} of a drafter swimming in region C in a two-swimmer configuration; the red curves indicate the maximum C_{DR} of a drafter swimming in region C in a three-swimmer configuration.

The results in Figure 3.14 show the maximum wave drag reduction in formation swimming,

varying with constant speed U and constant transverse separation d_t. The two groups of curves (red and black), representing two and three-swimmer configurations, show a similar trend. As the swimming speed increases, the drafter experiences an increased wave drag reduction. A higher speed will result in larger wave amplitudes, and the drafter could extract more energy from the waves generated by the leader. At a larger transverse distance, e.g. $d_t = 2.0$ m, C_{DR} increases linearly with the swimming speed. At a smaller transverse distance, e.g. $d_t = 1.5$ m, C_{DR} increases very slowly at $U > 1.8$ m/s. In the two-swimmer case, the wave drag reduction at $U = 2.0$ m/s is even smaller than that at $U = 1.9$ m/s. This is because the wave drag reduction is not only determined by the wave amplitude, but also by the wavelength. Increased speed will bring a larger wave amplitude, as well as longer waves. At $U = 1.9$ m/s, a better wave-riding configuration is achieved than at $U = 2.0$ m/s. The results also show that when the swimmers are getting closer, the drafter could achieve a higher wave drag reduction. However, at a very high swimming speed, the drag reduction becomes less sensitive to the transverse separation.

3.6 Summary

Returning to our central questions: 1) what mechanism determines the interaction; 2) which positions experience drag reduction or drag increase; 3) how much can drag be reduced or increased in 'drafting'? To answer these questions, we established a mathematical and numerical model and calculated the wave drag of a swimmer swimming alone and in formation in open water. Though the answers are highly dependent on the specific swimmer and swimming event, the findings in this study shed a light on the importance of the wave interference effects on competitive swimming. The interaction between human swimmers is determined by the wave interference on the free water surface. The energy-saving position of the drafter is determined by the wave drag reduction. The maximum wave drag reduction is observed when the drafter's fore part is in the wave trough while the aft part is in the wave crest. By taking this wave-riding position, a destructive wave interference phenomenon can be observed, where the waves generated by the swimmers are 180° out of phase. As a result of the wave cancellation effect, the wave drag can be minimized. In a two-swimmer configuration, the maximum wave drag reduction of the

drafter swimming at $U = 2.16$ m/s is 55 % when the partial wave cancellation effect occurs. In a three-swimmer configuration, a full wave cancellation effect can be observed, where the maximum wave drag reduction achievable is 110 %. In this case, the wave drag turns to be a thrust force, pushing the drafter forward. The above conclusions are based on wave drag computations for a simplified model. The viscous effects were not taken into account. According to the wave drag results of a single swimmer, the wave drag contributes 40–60 % of the total drag when he/she swims with high speed near the free surface. Considering the existence of the lane ropes, up to 70 % of the waves could be attenuated before they propagate to the adjacent lanes. It indicates the drafter could potentially save 6 - 10 % of the total drag by following a leader, or 13 - 20 % by following two leaders on either side. Of course, if the immersed depth of the swimmers increases slightly, the percentage of the drag reduction in a formation could be further reduced. The principle finding of this work is that the competitive swimmers could experience a strong hydrodynamic interaction when swimming in formation. By swimming in an optimum position behind one/two leading swimmers, the drafter could utilize the Kelvin waves as a propelling aid to preserve energy, hence improving the swimming performance.

Chapter 4

Unsteady waves generated by a single ship in shallow water

4.1 Introduction

Surface vessels, which are accelerated from the rest to a constant speed, can generate persistent unsteady waves. The wave-making resistance induced by these unsteady waves usually fluctuates around the steady wave resistance. This nature of the oscillations initiated by the unsteady effect during the acceleration phase has been observed in the towing tank experiments (Day et al., 2009; Doctors et al., 2008). The aims to propose a numerical method to predict this unsteady problem due to the acceleration of a ship from the rest in shallow water. The steady problem of a ship moving with a constant speed has been widely studied (Nakos et al., 1994; Raven, 1998; Sclavounos and Nakos; Tarafder and Suzuki, 2008; Yuan et al., 2019). However, the unsteady wave resistance of an accelerating ship, particularly in shallow water, was rarely investigated. Some pioneer works in the early 1950s shed light on the unsteady wave resistance. Lunde (1951) developed an unsteady theory to analyze the ship-wave problem. Based on Lunde's theory, Wehausen (1961) proposed asymptotic formulas to predict the unsteady wave resistance of a ship. The experiments conducted by Doctors et al. (2008) showed that the linearized theory (Doctors, 1975) provided well predictions of the acceleration effect on the resistance. However, he did not analyse the effect of different water depth on the unsteady waves generated

by the accelerated ship. The inland ships are most likely to maneuvre in shallow water. The behaviour of a ship in shallow water was investigated by slender-body theory (Chen and Sharma, 1995; Gourlay, 2008; Tuck, 1966a) and experimental measurements (Kijima and Nakiri, 1990). Apart from the theory method or experiments, with the development of higher performance computers, many numerical methods have been implemented to solve the shallow water problem. Terziev et al. (2018)used CFD (Computational Fluid Dynamics) to study the hydrodynamic interaction between the hull and the seabed. The steady sinkage, trim, and resistance of a Duisburg Test Case (DTC) container ship was simulated by using the software StarCCM+. However, the numerical method of CFD is time and resource consuming. Their research only investigated the steady problem of a ship moving with constant speed. The unsteady problem of an accelerating ship remains a challenging issue. The shallow water equation (Boussinesq equations) has been used numerically to simulate the waves generated by a ship at critical speed in limited water depths. Torsvik et al. (2006) investigated the speed effects on the waves generated by a ship passing through the transcritical speed region in shallow water based on Boussinesq equations. In their simulations, they examined the amplitude of the waves generated by a ship with various Froude number near critical speeds. Li and Sclavounos (2002) used modified Boussinesq equations to calculate the nonlinear long waves generated by a disturbance moving at critical speed. However, they did not consider the unsteady effects when a vessel is accelerated from the rest. The objective of the present study is to investigate the unsteady ship-bottom interaction when a ship model starts from the rest. The oscillation amplitude error (in percentage) is quantified at different acceleration a and water depth H. To achieve this goal, in this Chapter, the boundary integral methods employing simple Rankine singularities to implicitly solve the unsteady nonlinear free surface equations in an iterative solution methodology. Dawson (1977) firstly introduced the Rankine panel method in a practical form to linearize the free surface condition. The major advantages of the Rankine singularities method include the simplicity of the source singularity and the potential of employing the nonlinear free surface condition. Thus, Raven (1998) extended Dawson ‘s linearized free surface condition to the fully nonlinear one. To account for the unsteady free surface conditions, a developed linear free surface

condition was used to calculate the unsteady hydrodynamic force by using the Rankine source method (Yasukawa, 1990). Kring (1994b) selected a linear multistep integration scheme of a fourth-order predictor-corrector to investigate the time domain motions of a ship traveling with a constant velocity in waves by a bi-quadratic Rankine panel method. In order to predict the unsteady ship motion, some researchers investigated a ship moving from the rest to a constant speed in infinite water depth (Kring, 1994a; Nakos et al., 1994; Ohring and Telste, 1997). However, the effect of acceleration and water depth was not considered in their studies. In the present study, a 3D panel method based on Rankine type Green function will be used to solve the unsteady hydrodynamic problem of a ship accelerating with various acceleration a in different water depths H. The numerical method based on an implicit finite-difference algorithm will be described in Section 2. In Section 3, the validations of the numerical method are performed. After the validations, the method is applied to investigate the acceleration effect on the wave resistance of a ship in deep or shallow water (Section 4). Finally, the curves of wave resistance versus time and the wave patterns during the unsteady oscillation are presented and discussed.

4.2 Methodology

4.3 Problem definition

The present study aims to investigate the unsteady effects arising from a vessel accelerating from the rest in the presence of a free surface. Figure 4.1 shows the sketch of the problem in the present study. For a ship with forwarding speed, two right-handed coordinate systems are used: a global reference frame $O - x_0y_0z_0$ fixed to the earth, and a local reference frame $o - xyz$ fixed to the body. Both frames have positive x-direction pointing towards the bow, positive z direction pointing upwards. The local body-fixed $o - xyz$, as shown in Figure 4.1, is set on the undisturbed free surface. The water depth is H, ship length is L and towing speed is $U(t)$. The general form of the velocity history is depicted in Figure 4.6. The length of the sea bottom is assumed to be flat and sufficiently long.

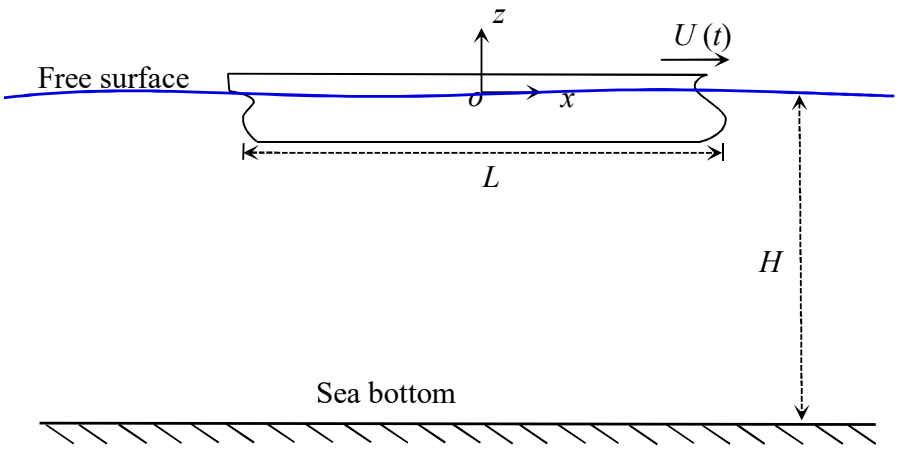

Figure 4.1: The sketch of the problem.

To calculate the hydrodynamic forces and the waves, a mathematical model of the boundary value problem (BVP) needs to be established. Within the framework of potential flow theory, it neglects the viscosity and compressibility of the flow. Therefore, the fluid domain can be described by using a disturbance velocity potential φ. In the fluid domain, the velocity potential φ satisfies the Laplace equation:

$$\frac{\partial^2 \varphi}{\partial x^2} + \frac{\partial^2 \varphi}{\partial y^2} + \frac{\partial^2 \varphi}{\partial z^2} = 0 \tag{4.1}$$

In order to account for the unsteady effect, an unsteady nonlinear free surface condition should be applied. In order to account for the unsteady effect, the unsteady nonlinear free surface condition is applied in the $o - xyz$ coordinates as following

$$\zeta_t - U(t)\zeta_x + \varphi_x \zeta_x + \varphi_y \zeta_y - \varphi_z = 0, \text{ on } z = \zeta \tag{4.2}$$

$$\varphi_t + g\zeta - U(t)\varphi_x + \frac{1}{2}(\varphi_x^2 + \varphi_y^2 + \varphi_z^2) = 0, \text{ on } z = \zeta \tag{4.3}$$

where $\zeta(x, y, t)$ is the free surface elevation and g is the acceleration due to the gravity. ζ_t and ϕ_t are the time derivative of the ζ and ϕ. ζ_x and ϕ_x are the x-derivative of the the ζ and ϕ, respectively as well as the definition in y-derivative and z-derivative. Equations 4.2 and 4.3 include some higher-order terms on the left-hand side. These terms should

be considered as they make a significant contribution to the unsteady problem to be investigated. The free surface condition is satisfied on the unknown surface $z = \zeta$. Apart from the free surface condition, the normal velocity of the flow should equal to the velocity of the moving body, which is the body surface boundary condition:

$$\frac{\partial \varphi}{\partial n} = U(t) n_1 \tag{4.4}$$

where $n = (n_1, n_2, n_3)$ is the unit normal vector inward on the wetted body surface. By the same reasoning, the boundary condition on the sea bottom and false bottom can be expressed as

$$\frac{\partial \varphi}{\partial n} = 0 \tag{4.5}$$

Besides, a radiation condition is imposed on the control surface to ensure that waves vanish at upstream infinity:

$$\varphi \longrightarrow 0,\ \zeta \longrightarrow 0\ as\ \sqrt{x^2 + y^2} \longrightarrow \infty \tag{4.6}$$

Equation 4.2 to 4.5 form a completed set of BVP. To solve the nonlinear unsteady BVP, the in-house-developed Rankine source program MHydro (Yuan et al., 2015b) needs to be extended. The BVP is solved iteratively and the detailed algorithm will be illustrated in the following section. Once the unknown potential φ is solved, the time-dependent pressure over the body-surface can be obtained from nonlinearized Bernoulli's equation

$$p = -\rho\Big(\varphi_t - U(t)\varphi_x - \frac{1}{2}(\varphi_x^2 + \varphi_y^2 + \varphi_z^2)\Big) \tag{4.7}$$

By integrating the pressure over the hull surface, the forces (or moments) can be obtained by

$$F_i = \iint_S p n_i ds,\ i = 1,\ 2,\ ...,\ 6 \tag{4.8}$$

where i represents the force in surge, sway, heave, roll, pitch and yaw directions. The wave elevation on the free surface can be obtained from the dynamic free surface boundary

condition in Equation 4.3 in the form

$$\zeta(x,y) = \frac{1}{g}(\varphi_t - U(t)\varphi_x + \frac{1}{2}(\varphi_x^2 + \varphi_y^2 + \varphi_z^2)) \tag{4.9}$$

4.3.1 Discretization of free surface condition

In this Chapter, an iterative algorithm with the implicit finite-difference scheme is developed to solve this unsteady nonlinear BVP. The nonlinear equation 4.2 and 4.3 is of a fully implicit type. The solution of these two equations can be obtained iteratively. The initial value of the variables φ and ζ at the time $t = 0$ are given by the solutions of the classic steady-state Neumann-Kelvin problem (Newman, 1977). At $t = 0$, the acceleration is applied to the ship model and the model speed is 0. Therefore, the initial value of φ^0 and ζ^0 are both set to be 0. At $t = \Delta t$, small ship speed is developed and the steady-state Neumann-Kelvin problem is solved at this time step to obtain the φ^1 and ζ^1. After that, an iterative scheme, which will be introduced later, is used to solve the time-dependent non-linearized free surface condition in equations 4.2 and 4.3:

$$U(t)^2\varphi_{xx} + g\varphi_z = 0 \tag{4.10}$$

The time derivatives in the free surface condition have to be discretized. The three-time-level scheme is used to obtain the first derivatives of φ and ζ.

$$(\varphi_t)_{i,j}^{n+1} = \frac{1}{\Delta t}\Big[\frac{3}{2}(\varphi)_{i,j}^{n+1} - 2(\varphi)_{i,j}^{n} + \frac{1}{2}(\varphi)_{i,j}^{n-1}\Big] \tag{4.11}$$

$$(\zeta_t)_{i,j}^{n+1} = \frac{1}{\Delta t}\Big[\frac{3}{2}(\zeta)_{i,j}^{n+1} - 2(\zeta)_{i,j}^{n} + \frac{1}{2}(\zeta)_{i,j}^{n-1}\Big] \tag{4.12}$$

where the subscript i, j indicates the index of the longitudinal and transverse elements respectively on the free surface. At each iterative step k, the linear terms of $x-$derivative in equation 4.2 are approximated implicitly on the left-hand side (LHS) terms. The rest nonlinear terms and cross-derivatives are put on the right-hand sides (RHS) as the knowns for the next iteration $t = t_{n+1}$ to update the wave elevation ζ. The dynamic condition in equation 4.3 is then satisfied through an implicit method using the present solution

at t_n to update potential φ at t_{n+1}. All variables are then updated by the latest values from the iteration as k is advanced. Residual errors of time derivatives of $|(\varphi_{i,j}^{n+1,k})^* - \varphi_{i,j}^{n+1,k}|$ & $|(\zeta_{i,j}^{n+1,k})^* - \zeta_{i,j}^{n+1,k}|$ can be evaluated. If both the $|(\varphi_{i,j}^{n+1,k})^* - \varphi_{i,j}^{n+1,k}| < \epsilon$ and $|(\zeta_{i,j}^{n+1,k})^* - \zeta_{i,j}^{n+1,k}| < \epsilon$, the iteration stops and $\varphi_{i,j}^{n+1,k}$ and $\zeta_{i,j}^{n+1,k}$ will be used to calculated the pressure. Otherwise, $\varphi_{i,j}^{n,k}$ in equation 4.13 will be replaced by $\varphi_{i,j}^{n+1,k}$. It is known that the iterative scheme has advantages of high accuracy and good numerical stability. At each iterative step k,

$$\frac{3\zeta_{i,j}^{n+1,k} - 4\zeta_{i,j}^{n,k} + \zeta_{i,j}^{n-1,k}}{2\Delta t} - U(t) \cdot (\zeta_x)_{i,j}^{n+1,k} = - (\varphi_x)_{i,j}^{n,k} \cdot (\zeta_x)_{i,j}^{n,k} - (\varphi_y)_{i,j}^{n,k} \cdot (\zeta_y)_{i,j}^{n,k} + (\varphi_z)_{i,j}^{n,k} \tag{4.13}$$

$$\frac{3\varphi_{i,j}^{n+1,k} - 4\varphi_{i,j}^{n,k} + \varphi_{i,j}^{n-1,k}}{2\Delta t} - U(t) \cdot (\varphi_x)_{i,j}^{n+1,k} = - g \cdot (\zeta)_{i,j}^{n+1,k} - \frac{1}{2}\Big[(\varphi_x \cdot \varphi_x)_{i,j}^{n,k} + (\varphi_y \cdot \varphi_y)_{i,j}^{n,k} + (\varphi_z \cdot \varphi_z)_{i,j}^{n,k}\Big] \tag{4.14}$$

In which $\varphi_{i,j}^{n+1,k}$ and $\zeta_{i,j}^{n+1,k}$ are the predicted values of $\varphi_{i,j}^{n,k}$ and $\zeta_{i,j}^{n,k}$ after the kth iteration. In order to obtain more stable numerical results, the 2nd-order up-wind difference scheme was implemented to obtain the spatial derivatives of the and on the LHS of the Equation 4.13 and 4.14 (Kring, 1994b). The transverse derivatives and the vertical derivatives of the nonlinear items are evaluated by using a central difference scheme. The implicit scheme is unconditionally stable, and its temporal and spatial accuracy is of second order, *i.e.*, $O(\Delta t^2), O(\Delta x^2, \Delta y^2)$.

4.3.2 Description of numerical simulation

In the present study, a benchmark model Wigley III hull is used in all of the case studies. In the numerical modelling, the panels are not only distributed on the free surface and wetted body surface of the ship hull, but also on the sea bottom. Thus, when the water depth changes, the shallow water effects can be accounted for directly in the BVP. The mesh of the computational domain is shown in Figure 4.2. In the presented study, due

to the symmetrical characteristic of the domain, only half of the computational domain is modelled. It allows a reduction of the total number of the panels required in the solution, hence saving computation time. Although the mirror method for the shallow water has been adopted by many researchers (Yuan et al., 2015b), it is not used in this Chapter as the present method will be extended to investigate the uneven sea bottom problem.

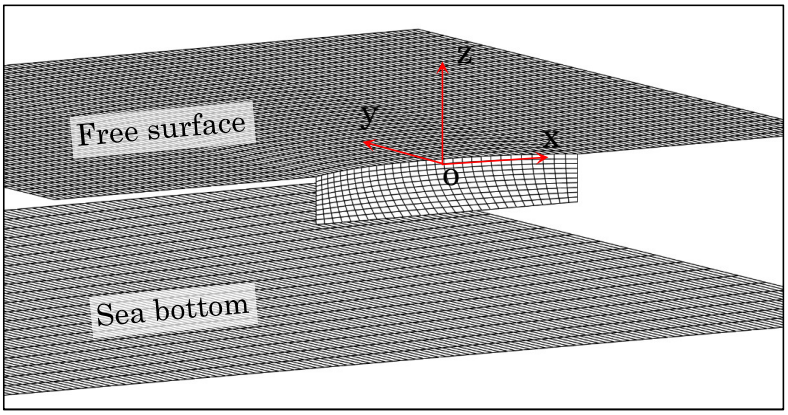

Figure 4.2: Panel distribution on the computation domain of a Wigley III model advancing on the sea bottom. There are in total 7354 panels distributed on the total computation domain in this simulation: 4,654 panels distributed on the free surface S_F, 300 on the wetted body surface S_H and 2400 on the sea bottom S_B. The computational domain is truncated at 1.2 L upstream, 1L sideways and 2L downstream. Typically, we worked with 7,354 unknowns and solved the linear system by Gauss_Seidel.

4.4 Results and discussions

4.4.1 Unsteady waves generated by a source point

Firstly, in order to validate the developed unsteady numerical method, the source point moving accelerating from the rest to a constant Froude number is investigated. The source is moving at and submerged at a depth of H, taken as $\frac{1}{4}$ steady wavelength, i.e., $H = 0.5\pi U^2/g$. The acceleration is equal to $a = 0.04g$. For the linear problem, it shall make use of the exact solution,

$$\begin{aligned}\zeta(x,y) = &-\frac{\epsilon F_n^2 sgn(x)}{\pi^2}\int_0^{\frac{\pi}{2}} cos\theta \int_0^{\infty} \frac{ke^{k|x|}cos(kysin\theta)g(k,\theta)}{F_n^4k^2 + cos^2\theta}dkd\theta \\ &+ \frac{\epsilon H(x)}{\pi}\int_{-\infty}^{\infty} ocs(x\xi)cos(y\xi\lambda)d\lambda\end{aligned} \tag{4.15}$$

by Peters (Peters, 1949), where

$$g(k,\theta) = F_n^2 k sin(kcos\theta) + cos\theta cos(kcos\theta) \tag{4.16}$$

$$\xi(\lambda) = \sqrt{\lambda^2 + 1}/F_n^2 \tag{4.17}$$

$sgn(x)$ is the sign function, and $H(x)$ is the Heaviside function. The integrals in this exact solution are evaluated numerically to obtain the free surface profile for a given Froude number. Generally, with careful numerics, this type of Rankine source panel method provides good agreement with the analytical solutions. As the waves propagate to the far-field downstream, a phase shift gradually appears, which is caused by the numerical dispersion and dissipation of the algorithm. This is not concerned in this Chapter due to it can be neglected in our study. A comparison between the waves in deep water and that in shallow water, as shown in Figure 4.3 (b) and (c), both the wave length and amplitude are different. One can imagine that the waves will eventually approach those of the steady shallow-water waves when the transit time is long enough. However, before the waves reach a new steady phase, they must experience a transition phase that is oscillatory in time. In the present work, we are interested in this unsteady, transition phase.

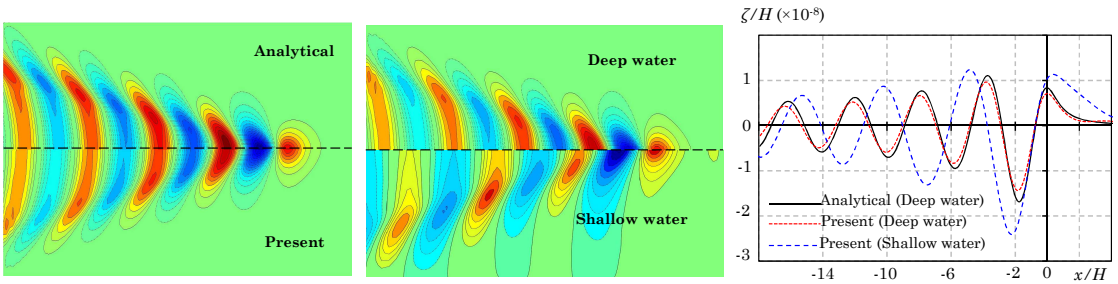

Figure 4.3: (a) Comparison of deep water wave pattern between analytical solution and the present calculations; (b) Comparison of the wave patterns in deep water and shallow water (The water depth is $h = 1.05H$ and the depth Froude number is $F_h = 0.78(F_h = U/\sqrt{gh})$; ($c$) Comparison of the wave profile at the centreline: $y = 0$.

4.4.2 Unsteady waves generated by a source point over a step bank

In practical operations when a ship maneuvers in a port/harbour/lock environment. Under this circumstance, a ship is likely to travel in close proximity to waterway boundaries that have abrupt change, *i.e.* a step-change in bank dimension or bottom depth; However, the circumstances have been less well studied, with the exception of Alam and Mei (2008), particularly the interesting unsteady three-dimensional wave fields. This focuses on the unsteady waves generated by a ship moving over a step bottom. The wave field behaviour, even though three-dimensional, is now more amenable to expedient numerical treatment with the use of Green's theorem for the full fluid domain (see Yeung (1982); Kring (1994b)).

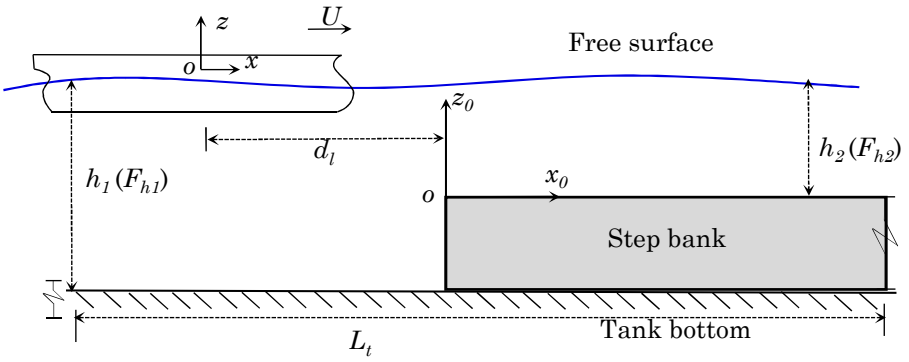

Figure 4.4: The sketch of the problem and the definition of the coordinate systems.

Two right-handed coordinate systems are used: a global reference frame $O - x_0y_0z_0$ fixed to the leading corner of the step bottom, and a local reference frame $o - xyz$ fixed to the body, as shown in Figure 4.4. Figure 4.5 shows the time history of the pressure acting on a source point when it passes over a step bottom of different depths. Before the source point reaches the leading edge of the step bottom, the pressure is nearly steady. After that, interestingly, this pressure starts to oscillate almost periodically. The oscillation of the pressure persists for a long time before it decays to a steady-state value, which corresponds to the steady pressure on the source moving in constant-depth shallow water. From a separate analysis (ITTC, 2017), one can show the appropriate normalized time scale to be used $tg/(8\pi)u$. The amplitude and the period of the oscillation are highly dependent on the water-depth ratio at the step bottom: a shallower water depth will

induce oscillation of larger amplitude and longer period and vice versa.

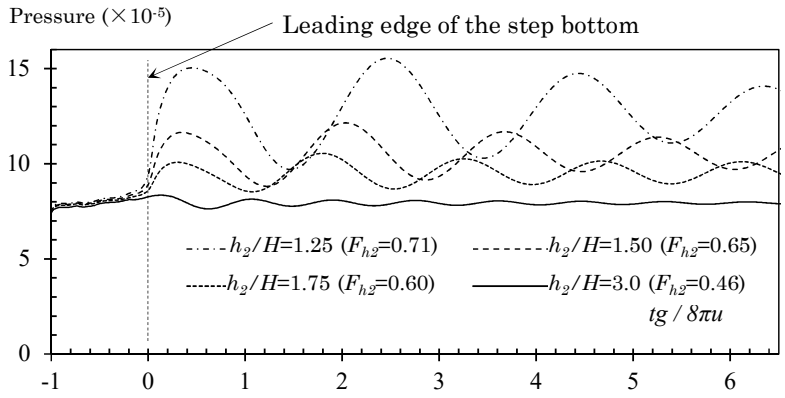

Figure 4.5: Time histories of the (non-dimensional) pressure ($p/rhou^2$/source strength) at $(x, y, z) = (0, 0, 0)$ when it moves from deep to shallow water (passing over a step bottom). H is the submerged depth of the source point, defined in Figure 4.4 and h_2 is the water depth at the step bottom. $t = 0$ corresponds to the instant when the source point reaches the leading edge of the step bottom.

Replacing the source point with a ship hull, which is of more practical interest, one can obtain the time history of the wave-making resistance by pressure integral of Equation 4.8. A similar oscillation phenomenon is observed, as shown in Figure 4.5. The wave-making resistance oscillates periodically around a mean steady resistance. A decay of the oscillation amplitude can be found. Obviously, the oscillation decays very slowly, indicating the oscillation will eventually vanish only if the time is sufficiently large. To quantify the unsteady effects, we separate the unsteady component R_u and ζ_u from the total wave-making resistance and wave elevation as

$$R_u = R_w - R_s,\ \zeta_u = \zeta - \zeta_s \tag{4.18}$$

where R_w and ζ is the total wave-making resistance calculated by solving the unsteady BVP. R_s and ζ_s are the corresponding quantities for the steady solution when the ship moves in shallow water $F_{h2} = 0.85$ obtained by solving the steady-state BVP. As shown in Figure 4.6, the fluctuation of the unsteady wave-making resistance component in the first three oscillations is factually larger than the mean steady component, which should attract particular attention in practical maneuvres. Of interest, we find some negative wave-

making resistance momentarily (acting in the same direction of ship movement) after the ship passes the leading edge of the step bottom, *e.g.*, at the time instants of $tg/8\pi U = 2.8$ and 6.0. The periodic oscillation of the wave-making resistance is significantly correlated with the unsteady waves.

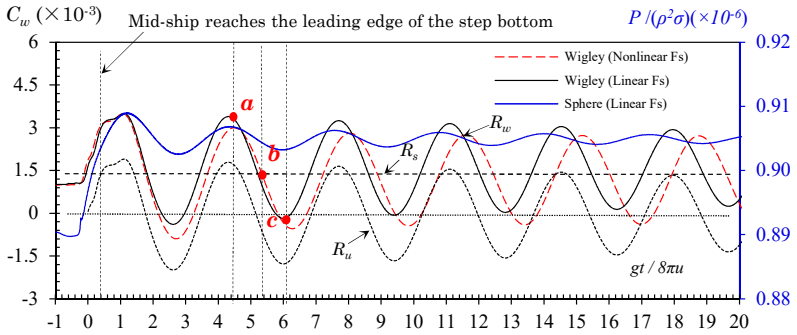

Figure 4.6: Time histories of the wave-making resistance coefficient, where ρ is the water density and S is the wetted surface area of the hull) of a Wigley III hull passing over a step bottom from $F_{h1} = 0.3$ to $F_{h2} = 0.85$. The total resistance time-dependent Rw is the sum of the steady resistance R_s and unsteady resistance R_u. The blue curve is the average non-dimensional pressure on a very small sphere ($R/H = 0.2$) submerged at $H = 0.25\pi u^2/g$, travelling from $F_{h1} = 0.3$ to $F_{h2} = 0.85$.

4.4.3 Unsteady waves and resistance in deep water

This section investigates the unsteady oscillation of the wave resistance induced by the accelerating ship in open water. The simulations aim to demonstrate how the oscillation components varying with the Froude number F_n in a constant acceleration phase. The acceleration is set to be the ratio of the ship's acceleration to the acceleration of gravity: $a = U(t) = 0.08g$. The ship model is constrained in sinkage and trim. Three Froude numbers $F_n = 0.2$, 0.3, 0.4 were investigated. The velocity histories of these three Froude numbers are shown in Figure 4.7. These data are based on the input signal to the carriage-drive system by Doctors et al. (2008) in their tests.

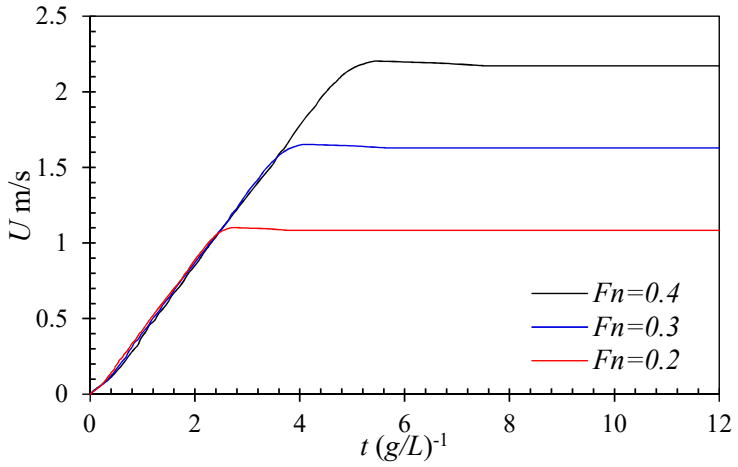

Figure 4.7: Velocity histories used in the present numerical studies.

The results of the time convergence study are shown in Figure 4.8. The non-dimensional wave-making resistance coefficient is defined as R_ω/W, in which W is the weight of the ship model. The different time steps (d_t) is adopted in Figure 4.8. X/L denotes the non-dimensional distance to the origin point at the initial time $t = 0$. The panel size to ship length ratio at each Froude number is fixed at $\Delta x/L = 1/\kappa$. The time then can be non-dimensionalized by

$$t' = \Delta x/U_0 = \frac{1}{\kappa F_n}\sqrt{\frac{L}{g}} \tag{4.19}$$

where the U_0 is the constant speed after the accelerating phase. In the present study, $\kappa = 30$. It can be found that the wave resistance is converged when the time step $d_t = 0.2t'$. The results in Figure 4.8 also show that the time history of the resistance can be divided into three phases. Phase I is the acceleration phase, in which the ship model is accelerated from the rest to the designed speed. In Phase I, the wave-making resistance gradually increases as the speed increases. Phase II starts at the moment when the ship reaches the target speed. As the acceleration disappears, the wave-making resistance does not reach a constant value. It experiences a transition phase before it enters into a periodic oscillation phase, which is Phase III. In Phase III, the wave-making resistance oscillates harmonically with a constant period. However, the oscillation curve may experience decay in amplitude. In the present study, we are mainly interested in Phase III.

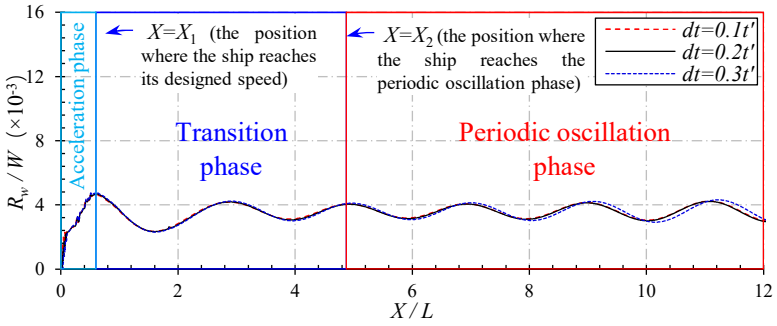

Figure 4.8: Time convergence study on the wave-making resistance. The Wigley III hull moves from the rest to the target speed at $F_n = 0.3$ with the acceleration $a = 0.08g$.

Figure 4.9 shows the unsteady wave-making resistance at $F_n = 0.3$ and $F_n = 0.4$. It can be found that the resistance Rw increases gradually during the acceleration phase until the ship reaches X_1, which is the position where the ship reaches the designed speed. After this acceleration phase, a short transition phase is observed before the ship model enters into the periodic oscillation phase. It indicates that the periodic oscillation of the R_w is initiated by the acceleration. In order to predict the effect of the nonlinear FSBC (free surface boundary condition), the wave resistance simulated by the nonlinear free surface condition is comparing with that of the linear free surface condition. From Figure 4.9 and Figure 4.10, it shows that the difference between these two FSBC close to each other, except for the very shallow $F_h = 0.85$. It can be found that the nonlinear effect is very dominant in very shallow water. It should be noted that the calculation of the linear results of the wave resistance is acceptable. As a result, the linear FSBC is adopted in the simulations.

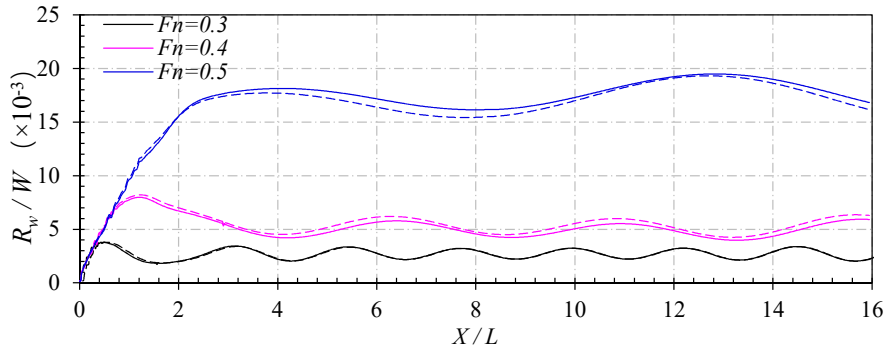

Figure 4.9: Comparing the wave resistance coefficient of the ship calculated by the nonlinear FSBC (solid line) with the linear FSBC (dashed line) at $F_n = 0.3$, 0.4 and 0.5 in deep water. The tank width is the same as the value in Doctors et al. (2008) that is $B_t/L = 1.5$. The acceleration is $a = 0.08g$.

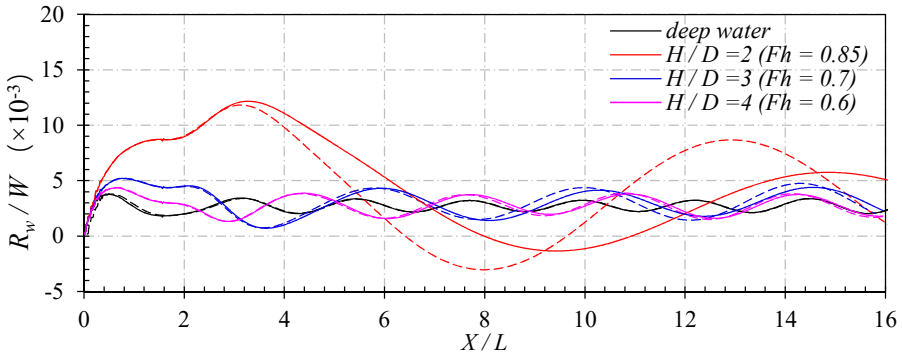

Figure 4.10: Comparing the wave resistance coefficient calculated of the accelerating ship by the nonlinear FSBC (solid line) with the linear FSBC (dashed line) at $F_n = 0.3$, 0.4 and 0.5 in deep water. The tank width is the same as the value in Doctors et al. (2008) that is $B_t/L = 1.5$. The acceleration is $a = 0.08g$.

The present results are compared with the experimental measurements conducted by Doctors et al. (2008). The ship is traveling from the rest to the target Fn with the acceleration $a = 0.08g$. Doctors et al. (2008) investigated the oscillations of the wave resistance during the periodic oscillation phase. The results calculated by their thin-ship theory are also included in the comparison, as shown in blue curves. The horizontal dash line denotes the steady wave resistance measured by the Ship Research Institution (SRI) and the University of Tokyo (UT) (Kajitani et al., 1983) at each Froude number. From Figure 4.11, it can be seen that the oscillation amplitude of the wave-making resistance predicted by the present method has a better agreement with the experimental results at $F_n = 0.3$. In

terms of the oscillation period T, the present prediction also shows a satisfactory agreement with the experimental measurements. However, it can be observed that there is a phase shift between these two results. Although there is some discrepancy in magnitude at $F_n = 0.3$, the presented results has a better agreement with the experiments. The difference could be attributed to the fact that the ship model is free to sink and trim in the experimental measurements conducted by Doctors et al. (2008), while in the present calculations, the ship is constrained in sinkage and trim. Observing the oscillation amplitude of the present predictions, it can be seen that there is limited decay in the present calculation, which is different from the experimental measurements. In fact, the oscillation should experience decay due to the damping effect. This damping effect is mainly attributed to two sources: hydrodynamic damping in terms of the radiation waves and the viscous damping. In the experimental tests, the model is free to sink and trim, and as a result, some energy is damped due to the oscillation motions in sinkage and trim. The viscous damping in the experimental tests will also decay the oscillation amplitude. In the present study, there is no hydrodynamic damping due to the ship motion (the motion here is referred as the oscillation motion), since all the degrees of freedom (DoF) are fixed. Moreover, the present potential flow solver does not take the viscous effect into account. Therefore, the present calculations cannot capture the decay property of the wave-making resistance. As F_n increases to 0.4, the oscillation amplitude becomes smaller, while the oscillation period becomes larger. The unsteady wave-making resistance still fluctuates around a mean value, which corresponds to the steady resistance under the target speed. It can be concluded from Figure 4.11 that the oscillations of the resistance initiated by the acceleration decay very slowly. This is may due to the wave reflection induced by the side-wall effect. For a ship model of 3 meters, the oscillations are still obvious after travelling 48 meters in the towing tank. It indicates that when conducting a towing test starting with acceleration in deep water, the measurements may not be stable and this unsteady effect will retain for a long time. The post-processing of the data should be very careful. As suggested by ITTC (2011), it is recommended to use at least five oscillations to find the mean wave-making resistance.

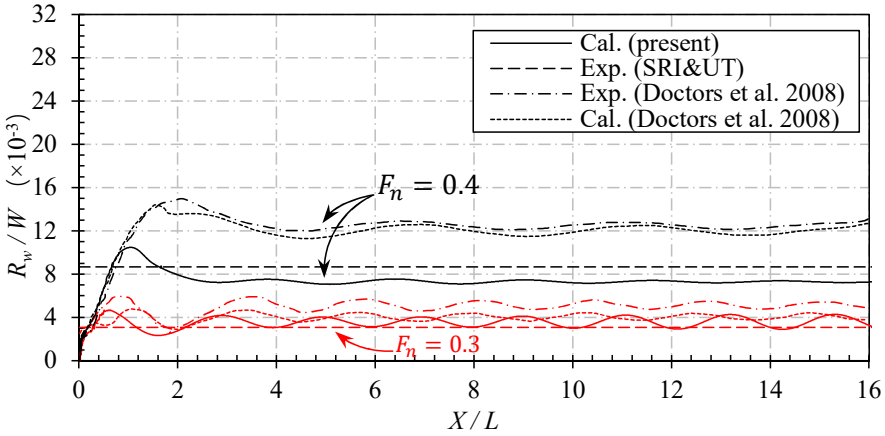

Figure 4.11: Wave resistance coefficient at $F_n = 0.3, 0.4$. 'Exp. (Doctors)' is the unsteady experimental data by Doctor et al. (2008). 'Exp. (SRI & UT)' is the data from the steady tests conducted by the Ship Research Institution (SRI) and the University of Tokyo (UT) (Kajitani et al., 1983).

To quantify the unsteady effects, we separate the unsteady component R_u from the total wave-making resistance as

$$R_u = R_w - R_s, \tag{4.20}$$

where R_w is the total wave-making resistance calculated by solving the unsteady BVP in Equations. 4.1-4.6. R_w is the steady wave-making resistance obtained by solving the steady BVP. Figure 4.12 shows the comparison of the steady and unsteady wave-making resistance at Fn =0.3. Four typical positions are selected to represent the evolution of the unsteady waves: a, $X/L = 0.25$ (Phase I), where the ship model is just accelerated and the target speed is not yet achieved; b, $X/L = 0.56$ (Phase II), where a considerable wave-making resistance is observed; c, $X/L = 2.9$ (Phase III), where a crest of the wave-making resistance is found; and d, $X/L = 3.9$ (Phase III), where a trough of the wave-making resistance is found. Figure 4.13 displays the transient wave patterns of the Wigley model moving at these four different positions after a start-up at $F_n = 0.3$. It can be observed how the wave patterns are developed during the acceleration phase. The contour represents the pressure distributed under the free water surface: the crests (in red) indicate a relatively high-pressure region, and the troughs (in blue) indicate a lower pressure region. According to the equation. 4.8, the wave-making resistance can be calculated by the pressure integral

over the wetted surface. At position a, the divergent and transverse waves are not fully developed and the waves are mainly initiated in the bow and stern area. At positions b, the transverse and divergent waves are gradually developed. At this position, the pressure distributed in the bow area is high, and the pressure distributed in the after part of the ship is low. As a result of pressure integral, the wave-making resistance reaches a very large positive value, as shown in Figure 4.12. When the ship model enters into Phase III (positions c and d), the Kelvin waves are fully developed. Comparing the wave patterns in these two positions, it can be found that the wave length is the same, while the wave amplitude is slightly different. Obviously, the crest (higher pressure) in ship bow area at positions c is higher than that in positions d, while the trough (lower pressure) in ship stern area at positions c is higher than that in positions d. As a result, the total wave-making resistance in positions c is higher than that in positions d, as shown in Figure 4.12.

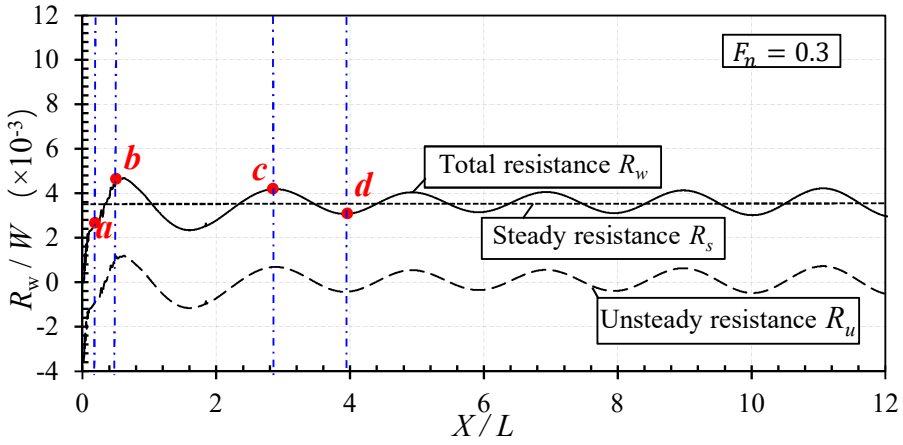

Figure 4.12: The steady and unsteady components of the wave-making resistance of the Wigley hull accelerated from the rest to the target Froude number $F_n = 0.3$ in deep water. The target speed is achieved at $X/L = 0.54$.

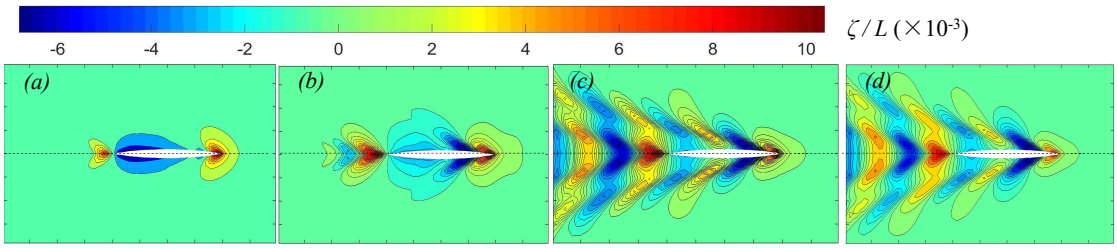

Figure 4.13: Transient wave patterns generated by a Wigley III hull accelerated from the rest to the target Froude number F_n= 0.3 in deep water. The wave elevation ζ is non-dimensionalised as $\zeta/L.(a)X/L = 0.25; (b)X/L = 0.56; (c)X/L = 2.9; (d)X/L = 3.9$.

The unsteady wave patterns in Figure 4.13 vary with the time, which shows very similar property to the radiation waves. Therefore, it will be very interesting to look at the radiation frequency of the unsteady wave. This radiation frequency can be represented by the oscillation frequency of the wave-making resistance, as shown in Figure 4.13. Figure 4.14 compares the present calculated frequency with those from Doctors' experimental measurement, as well as from the calculations by Nakos et al. (1994). Generally, the present results agree with the numerical results (Nakos et al., 1994) very well at various Froude numbers. However, there are some differences between the numerical calculations and the experimental measurements. As discussed before, it can be attributed to the fact that the ship model is constrained in sinkage and trim, and the viscous effects are not considered in the numerical calculations. The results in Figure 4.13 also shows that the oscillation frequency decreases as the Froude number increases.

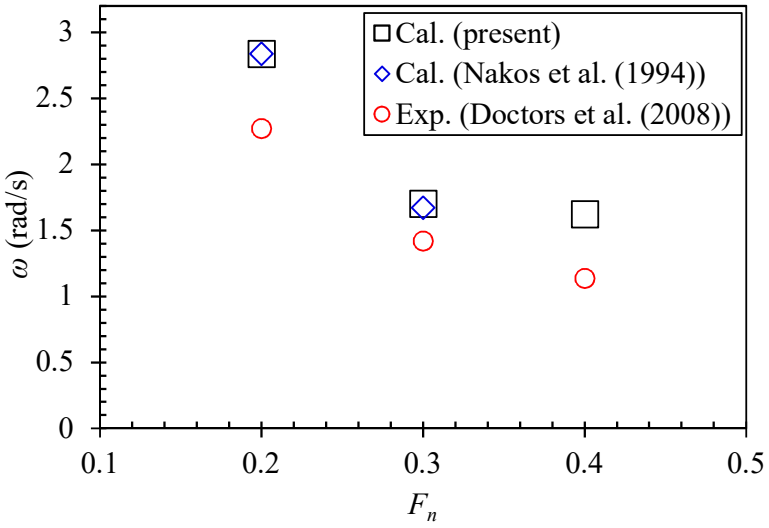

Figure 4.14: The oscillation frequency ω calculated by the present method compared with the experimental results (Doctors et al., 2008) and numerical results (Nakos et al., 1994) at different Froude number F_n.

4.4.4 Discussions on the acceleration

To achieve the target speed, we can give the carriage a large acceleration, hence reducing the time in the accelerating phase. Alternatively, we can use a smaller acceleration, which means a longer time to reach the target speed. The former solution may result in a larger oscillation amplitude of the data, due to the significant unsteady effect induced by the large acceleration. The later solution may bring a smaller oscillation amplitude due to the slow acceleration process. However, it takes more time to reach the target speed. It will be interesting to compare these two solutions and discuss the effect of acceleration. In the case studies, we select four typical acceleration, varying from $0.02g$ to $0.08g$. To reach the target speed, it takes different time. Figure 4.15 shows the sample time history of the carriage speed of a Wigley model with the target Froude number of $F_n = 0.2$.

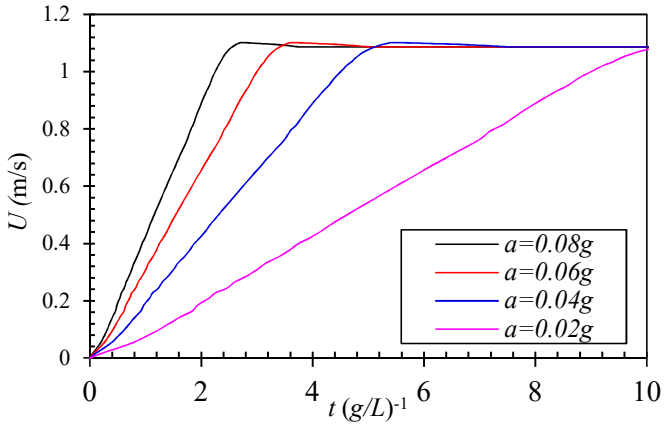

Figure 4.15: Time histories of the ship model velocity at $F_n = 0.2$ with different constant acceleration $a = 0.08g,\ 0.06g,\ 0.04g,\ 0.02g$.

Figure 4.16 shows the time history of the wave-making resistance of the Wigley III hull at different target Froude numbers: (a) $F_n = 0.2$; (b) $F_n = 0.3$; (c) $F_n = 0.4$. To achieve these target Froude numbers, the ship model is accelerating with different accelerations varying from $0.02g$ to $0.08g$. Compare the results of different Froude numbers, it can be found that the oscillations become less prominent as the target speed increases. Special attention should be paid to the low-speed tests. It can also be found that as the speed increases, the oscillation period becomes larger. Comparing the oscillations with different accelerations, it can be found that the oscillation amplitude increases as the acceleration increases. However, the oscillation period is hardly affected by the acceleration. It should be noted that when performing tests the acceleration is normally reduced when the speed is reduced. Therefore, investigation of the low acceleration effect on the slow ship is important for the towing tank experiment. At low target speed, e.g., $F_n = 0.2$, after a short accelerating phase, the wave-making resistance enters into the periodic oscillations. An interesting finding is that the oscillation amplitude does not follow a constant value or a decaying trend. The reason for this irregular oscillation is unknown. As the target speed becomes higher, e.g., $F_n = 0.3$ and $F_n = 0.4$, this irregular phenomenon gradually disappears.

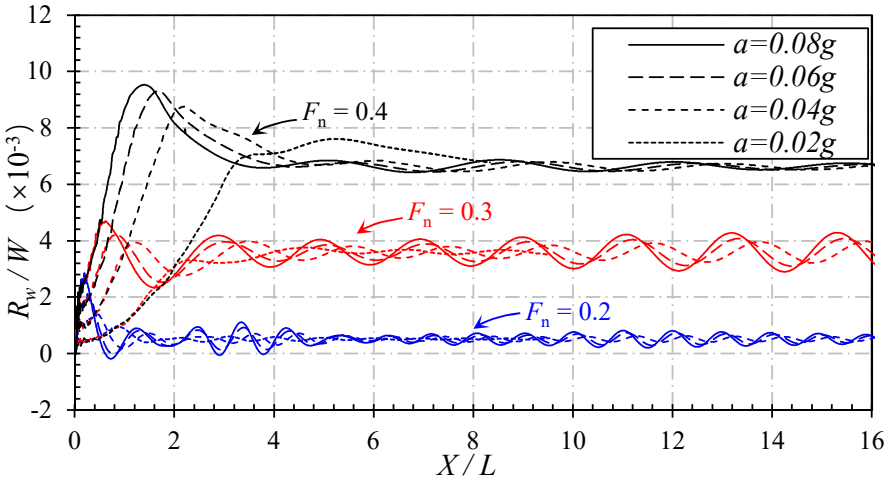

Figure 4.16: Time history of the wave-making resistance at $F_n = 0.2,\ 0.3,\ 0.4$ with different constant acceleration $a = 0.08g,\ 0.06g,\ 0.04g,\ 0.02g$.

To quantify the effect of acceleration, we need to introduce a coefficient which can be used to descript the oscillation of the wave-making resistance. Figure 4.17 shows a typical result of the wave-making resistance. The very large peak value is usually observed shortly after the ship model's target speed is reached. Thereafter, the result will experience periodic oscillations. As shown in Figure 4.17, we use $R_n\ (a)$ to represent each peak value in the wave-making resistance curve, where n is the series number of each peak and a is the acceleration variable. R_s denotes the mean wave-making resistance in the periodic oscillating phase after the target speed is achieved. A_R, which is the coefficient used to descript the n-th nondimensional oscillation amplitude, is defined by

$$A_{Rn}(a) = \frac{R_n(a) - R_s}{R_s} \times 100\%, \tag{4.21}$$

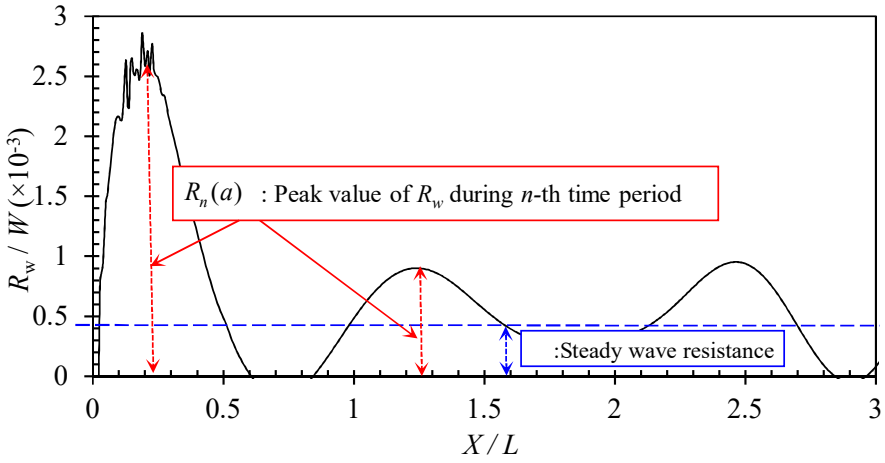

Figure 4.17: Definition of the peak value $R_n(a)$ and the steady wave-making resistance R_s in Equation. 4.21.

$A_R = 0$ indicates there is no oscillation of wave-making resistance. $A_R = 0.1$ indicates that the amplitude of the oscillation takes up 10 % of the steady wave-making resistance. Therefore, A_R (in percentage) can be used to quantify the unsteady effects, and a smaller A_R implies a more stable measurement. Plotting A_R against the travelling distance X/L can help to quantify how stable the measurements are. The results of A_R are shown in Figure 4.18. Generally, to achieve a smaller A_R, a smaller acceleration is desired. However, at high Froude number of $F_n = 0.4$, when a very small acceleration of $a = 0.02g$ is applied, the ship has to travel a distance of 13 times of the ship length before it enters periodic oscillating phase. It can be concluded from Figure 4.18 that when conducting a ship resistance test in a towing tank, a small acceleration should be applied to the low Froude number, while a relatively larger acceleration is suggested to be applied to higher Froude numbers.

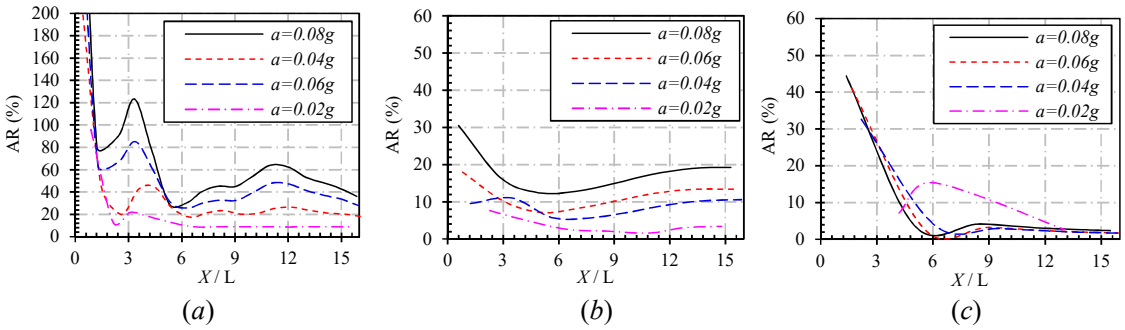

Figure 4.18: The nondimensional oscillation amplitude coefficient A_R at $F_n = (a)$ 0.2, (b) 0.3, (c) 0.4 with different constant acceleration $a = 0.08g$, $0.06g$, $0.04g$, $0.02g$.

4.4.5 Unsteady waves and resistance in shallow water

The unsteady waves generated by an accelerating ship in shallow water have never been studied by the works of literature. The methodology developed in Section 2 is extended in this section to investigate the shallow water effects. In the simulations, the acceleration applied to the ship model is $a = 0.08g$ at all of the water depths. Three water depths are selected: $H/D = 2$, $H/D = 4$ and $H/D = 6$. The Froude number varies from 0.1 to 0.4, and the depth Froude number Fh covers a range from the subcritical speed to the supercritical speed. It should be noted that the present study will not investigate the soliton wave generated at the critical speed $F_h = 1.0$ (Li and Sclavounos, 2002).

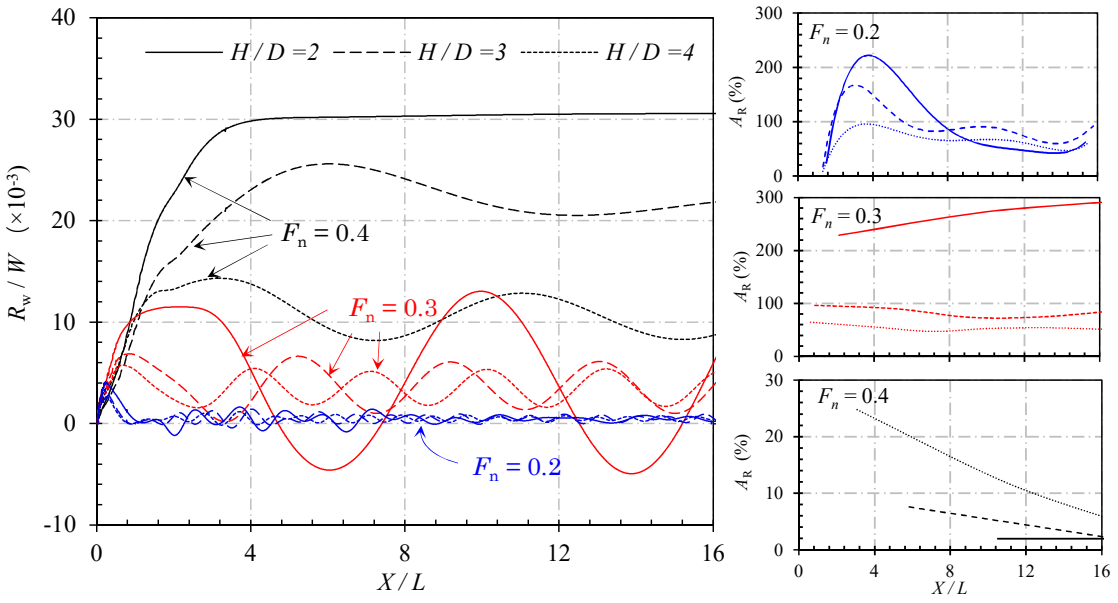

Figure 4.19: Time history of the wave-making resistance and the nondimensional oscillation amplitude AR at different water depths and different Froude numbers. The tank width is $B_t/L = 4$.

Figure 4.19 shows the wave-making resistance in shallow water obtained by using the present time-domain Rankine panel method. All the curves are oscillating about a mean value (the steady wave-making resistance at the given speeds and water depths). Comparing the results with different Froude numbers, it can be seen that the unsteady effect becomes less prominent as the speed increases. As the speed increases, the oscillation period increases due to the longer radiation waves excited by the acceleration. Similar to the deep water cases, the wave resistance at $F_n = 0.2$ in the periodic oscillation phase experiences some irregular oscillations. However, at $F_n = 0.2$, the wave-resistance is very small. The viscous component is the main contribution to the total resistance. Therefore, in the towing tank test, these oscillations with irregular amplitude can hardly be identified. This irregular amplitude phenomenon becomes less obvious as the speed increases (it still exists). Comparing the results at deferent water depths, it can be found that at $F_n = 0.2$ and $F_n = 0.3$, the unsteady effect is amplified by the shallow water effect. However, as the Froude number increases to $F_n = 0.4$, an interesting phenomenon is observed: the oscillation amplitude is reduced as the water depth decreases. At $F_n = 0.4$

and $H/D = 2$ ($F_h = 1.13$, which is in supercritical speed), the wave-making resistance enters into a near-steady phase shortly after the accelerating phase. When the ship model is accelerated to the critical speed ($F_h = 1.0$), the travelling speed of the unsteady wave is the same as the ship speed. As the shipping speed keeps increasing to the target speed ($F_h = 1.13$), the unsteady waves travel slower than the ship model and the steady Kelvin wave (steady wave pattern related to the $F_h = 1.13$). These unsteady waves propagate only in the downstream direction. They will not interact with the steady waves around the ship hull. As a result, the pressure distributed over the vessel remains steady and the total wave-making resistance enters into a near-steady phase at $F_h > 1.0$. This phenomenon is also observed by Chio and Mei (Choi and Mei, 1989). Thus, in the resistance test of a ship at supercritical speed, the unsteady effect excited in the acceleration phase can be negligible. At $F_n = 0.2$ and $F_n = 0.3$, for all the given water depths, the speed is considered to be subcritical and the ship model travels slower than the surface wave. Particularly, at $F_n = 0.3$ and $H/D = 2$ ($F_h = 0.85$), the unsteady waves travel slightly faster than the ship model. The relative speed between the unsteady wave and the ship model is very small. It takes a longer time for the unsteady waves to travel a distance of a wave length. Therefore, the wave-resistance fluctuates with a very large amplitude and period. At $X/L = 6$ and 14, the wave-making resistance is found to be negative, which indicates that at these two positions, the direction of the wave-making resistance will be the same as the moving direction. This interesting phenomenon can be explained by the interaction between steady and unsteady waves, which will be discussed later. In the ITTC procedure (ITTC, 2011), some procedures of testing and data acquisition are proposed for resistance tests by considering the unsteady effect excited in the accelerating phase. It is suggested to use at least five periods of oscillation to find the mean values of the resistance. These procedures works fine in deep water, as the amplitude of any 5 continuous periodic oscillations is fluctuating around a steady mean resistance. However, for the lower speed test in shallow water, *e.g.*, $F_n = 0.2$ and $H/D = 2$, the oscillation amplitude of the resistance is irregular and it is hard to find the mean values in only five oscillations. Special attention should be paid to these tests.

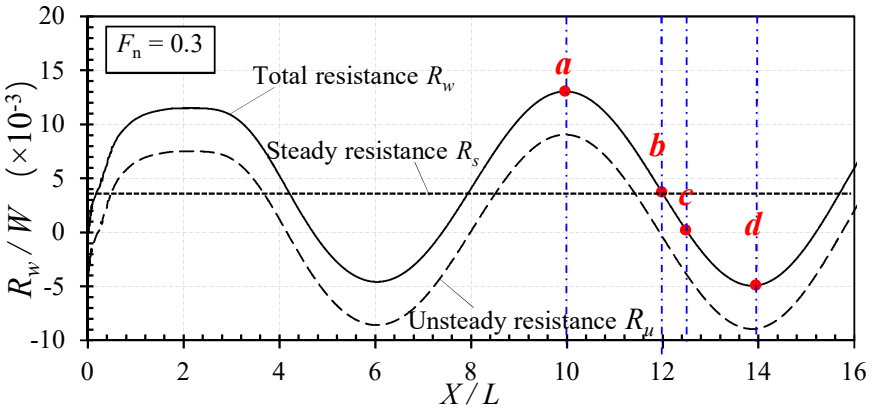

Figure 4.20: Time history of the wave-making resistance at $F_n = 0.3$ at $H/D = 2$.

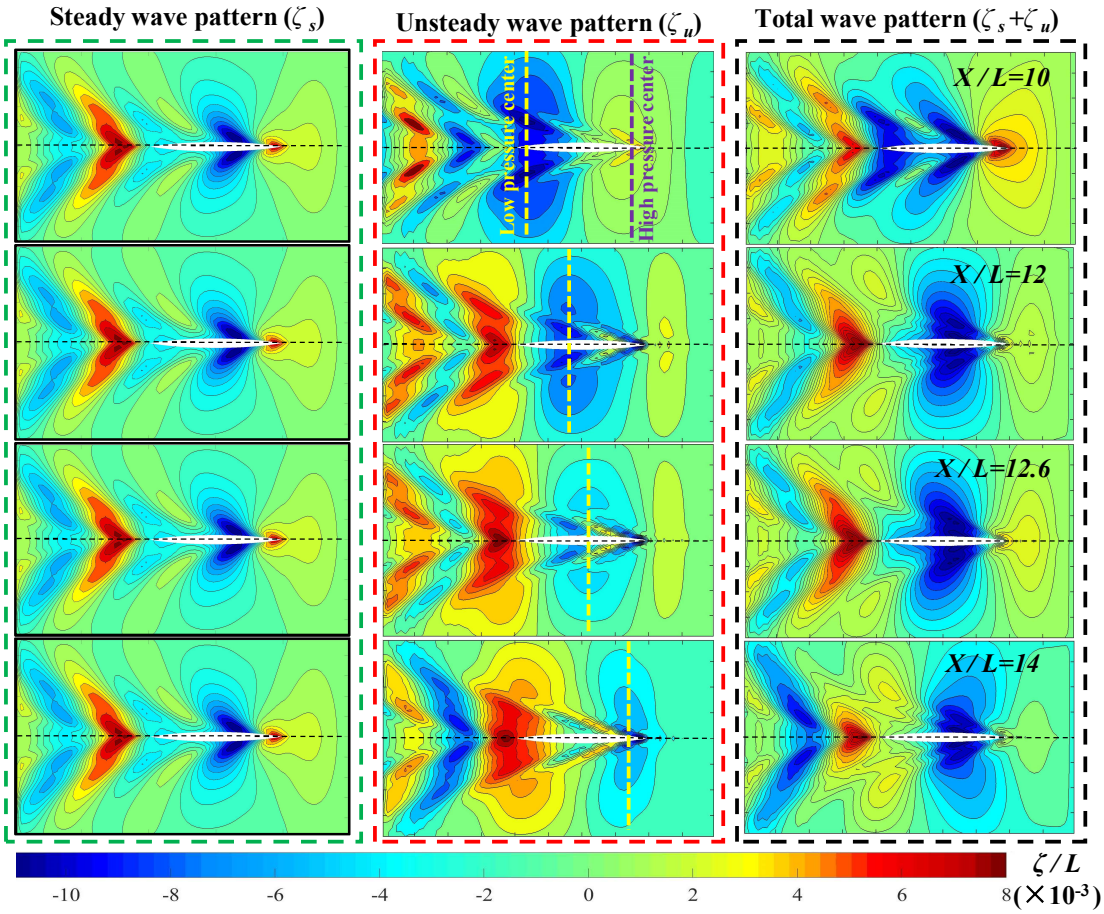

Figure 4.21: The steady and unsteady transient wave contours at four selected positions. The Froude number is $F_n = 0.3$ and the water is $H/D = 2.0$.

To quantify the unsteady wave component, we separate the unsteady component ζ_u from the total wave elevation which is solved by the unsteady BVP

$$\zeta_u = \zeta - \zeta_s \tag{4.22}$$

Where ζ_s denotes the steady wave elevation obtained by solving the steady BVP. The unsteady wave elevation ζ_u defines artificially as the difference between the steady wave elevation ζ_s and total wave elevation ζ. Figure 4.20 shows the comparison of the steady and unsteady wave-making resistance. As discussed before, the total resistance enters into the periodic oscillation quickly after the acceleration phase. Since the amplitude of the unsteady oscillation is larger than that of the steady resistance, a negative total wave-making resistance can be observed at $X/L = 6$ and 14. As the resistance time history is a near-harmonic curve, it would be interesting to investigate the evolution of the unsteady waves in a half period. Here we select a half period from $X/L = 10$ to $X/L = 14$. Four typical positions are highlighted: *a*. $X/L = 10$, where the maximum unsteady wave-making resistance is found; *b*. $X/L = 12$, where the unsteady wave-making resistance is zero (the total wave-making resistance is the same as the steady component); *c*. $X/L = 12.6$, where the total wave-making resistance is zero (the unsteady component has the same magnitude, but an opposite sign of the steady component); *d*, $X/L = 14$, where the minimum unsteady wave-making resistance is observed. Figure 4.21 shows the wave contour at these four positions. The first column presents the steady wave pattern generated by the ship model at $F_n = 0.3$ and $H/D = 2$ ($F_h = 0.85$). As the BVP does not involve time variable at the body-fixed coordinate system, the steady wave pattern is time-independent at all these four positions. From the steady wave pattern, we can find that a wave crest is observed at the ship bow area, while a wave trough is observed at the ship stern area. Wave crests represent high-pressure region under the free water surface and the wave troughs represent low-pressure distribution. Therefore, a positive wave-making resistance can be obtained by pressure integral over the wet body surface, as shown in Figure 4.20. The middle column shows the unsteady wave pattern generated at the selected positions. Generally, the unsteady waves have the same wave length as those of the steady waves. However, due to the speed difference (the unsteady waves

travels faster than the steady wave at $F_h = 0.85$), a clear forward-propagating property can be observed in the body-fixed coordinate system. At position a, high pressure is distributed over the ship bow area, while low pressure is distributed over the ship stern area. It is in phase with the steady pressure. The total wave elevation is amplified due to the constructive interference between steady and unsteady waves, and the total wave-making resistance, therefore, reaches its maximum by the superposition of the steady and unsteady components. As the time moves forward when the ship model reaches position b at $X/L = 12$, the lower pressure centre at the stern and the high-pressure centre at the bow move forward. As a result, the unsteady pressure distributed over the stern and bow are in balance, and the unsteady wave-making resistance at this position is zero. The low-pressure centre keeps moving forward to the mid-ship at position c, while the high-pressure centre has moved ahead of the vessel. At the same time, another high pressure is approaching the ship stern from backward, which modifies the pressure distribution at the stern. As a result, a negative unsteady wave-making resistance can be observed, as shown in Figure 4.20. At position d, the low-pressure centre is propagating to the ship bow, while the ship stern is dominated by high pressure. This is a wave-riding case, where a ship experiences an unsteady resistance with the same direction of moving. At this moment, the transient unsteady waves are out of phase with the steady waves. Due to the destructive wave interference, a minimum wave-making resistance can be observed. Moreover, as the magnitude of the unsteady waves is larger than that of the steady waves in the ship bow and stern area, the total wave-making resistance becomes negative, which pushes the ship to move forward. It can be foreseen and in the following half period, the unsteady wave-making resistance will experience an increase as the unsteady waves propagate forward. Figure 4.22 shows the frequency of the unsteady waves. As the travel speed increases, the radiation frequency decreases. It indicates the radiation waves have to take a longer time to 'catch' the ship model. It can also be found that like shallow water, the radiation wave will travel with a lower frequency.

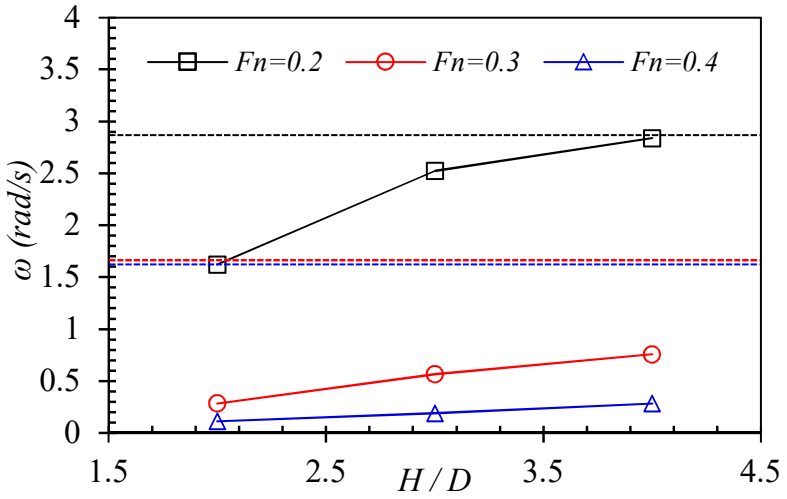

Figure 4.22: Unsteady wave frequency ω at different water depths. The dash lines are the frequency at deep water at each corresponding Froude number.

4.5 Summary

In the present study, we proposed an unsteady potential flow solver to investigate the unsteady phenomenon involved in ship model tests in shallow water. By imposing an unsteady non-linear free surface condition to the BVP, we successfully captured the unsteady waves initiated by a ship that was towed from the rest to target speed. Generally, the wave-making resistance experiences three phases: acceleration phase (Phase I), transition phase (Phase II) and periodic oscillation phase (Phase III). In Phase I, the wave-making resistance gradually increases as the speed increases. After the ship model reaches the target speed, the wave-making resistance will keep increasing until it reaches its maximum. It experiences a transition phase before it enters into Phase III: periodic oscillating. The duration of the first two phases is usually short, and we are more interested in Phase III, in which the mean steady wave-making resistance is found. Therefore, it is important to know the amplitude and period of the oscillating wave-making resistance in Phase III. The oscillation amplitude and period are mainly determined by three factors: speed, acceleration, and water depth.

4.5.1 Speed effect:

At low speed ($F_n <= 0.2$), the resistance experiences high-frequency oscillation. The amplitude of the oscillation could be larger than the steady resistance. The wave-making resistance is dominant by the unsteady component. At medium speed ($0.2 < F_n < 0.4$), the amplitude of oscillation is smaller than the mean steady wave-making resistance, and the oscillation period is longer. However, the oscillations are still very obvious in the measured signal. At high speed ($F_n >= 0.4$), the resistance curve is dominant by the steady component and the oscillation of the signal is very small with a very large period. Therefore, particular caution should be paid to the low-speed wave-making resistance test.

4.5.2 Acceleration effect:

To achieve the target speed, we can either give the carriage a larger acceleration that requires less time to reach Phase II or a smaller acceleration which means a longer time to reach the target speed. Our simulations showed that the oscillation period was hardly affected by the acceleration. At low and medium target speed, *e.g.* $F_n = 0.2$ and 0.3, the amplitude of the oscillations in Phase III increases as the acceleration increases. Therefore, a small acceleration is suggested at low and medium speed tests. At high target speed, *e.g.* $F_n = 0.4$, the oscillation is hardly affected by the acceleration. Therefore, a larger acceleration is suggested, in order to reduce the time in Phase I and Phase II.

4.5.3 Shallow water effect

The unsteady effect is amplified by the shallow water effect. At low and medium target speed, e.g. $F_n = 0.2$ and 0.3, the total wave-making resistance is dominant by the unsteady component. Due to the large amplitude of the unsteady component, some negative wave-making resistance was observed, which can be explained by the destructive interference between the steady and unsteady waves. When the ship model is accelerated to the supercritical speed ($F_h > 1.0$), the unsteady waves travel slower than the ship model and the steady Kelvin wave, and they will not interact with the steady waves around the ship

hull. As a result, the pressure distributed over the vessel remains steady and the total wave-making resistance enters into a near-steady phase. Thus, in the resistance test of a ship at supercritical speed, the unsteady effect excited in the acceleration phase can be negligible.

Apart from the above conclusions, we also encountered some issues that could not be explained, to the best of our knowledge. In Phase III, the oscillation amplitude is supposed to be decayed after the ship model travels a sufficiently long time. However, this decay is not observed in the present calculation due to the non-viscous assumption. Besides, some irregular oscillations were observed. At a certain duration of time, the oscillation amplitude is subject to an increase, rather than decay. The reason for this phenomenon is unknown, and further study is therefore required.

Chapter 5

Unsteady interaction between multiple ships travelling with different speeds

5.1 Introduction

Hydrodynamic interaction occurs when a ship is overtaking (or being overtaken) other ships. Because of the confined nature of the realistic environment, operating safety and accurate control of the vessel require the knowledge of the hydrodynamic forces acting on it. A numerical technology is developed and applied to this unsteady interaction problem for determining the magnitude of such forces or moments. Pioneering studies have provided fundamental insight into the problem of the interaction between multiple ships since the 1960s. The slender-body theory has been widely popular during the 1960s-1990s (Collatz, 1963a; Dand, 1975b; Kijima and Yasukawa, 1984; Tuck and Newman, 1976; Tuck, 1966a; Varyani et al., 1998a; Yeung, 1978b). For the ship travelling at relatively low speed, the numerical calculations based on strip theory showed a good prediction of the force and moment on ships during the passing or overtaking process. Then, due to the assumption adopted in these studies mentioned above includes that the ships are slender, thus, to account for the three-dimensional effects Korsmeyer et al. (1993b) adopted a 3D panel method for any number of arbitrarily shaped bodies. However, his model neglected the

free surface effect. More recently, the three-dimensional panel method has been more commonly used (Söding et al., 2005; Xiang and Faltinsen, 2011; Xu et al., 2016; Zhou et al., 2012b). They have not yet investigated the effects of unsteady free surface waves on interaction forces. However, they draw the conclusion that the potential flow has provided a good prediction of interaction forces on ships travelling at relatively low speed. With the development of computational technology, CFD (Computational Fluid Dynamics) is used to investigate the viscous effects on the ship to ship problems by various turbulence models (Zou and Larsson, 2013). However, no results were made to investigate the free surface effects or treated as a steady problem. The long-time unsteady free surface waves are still not including in their research. The URANS simulations are running by Mousaviraad et al. (2016), in which the free surface boundary condition was considered. However, these studies focus more on hydrodynamic forces. The results of free surface elevation were neither measured in the model tests nor presented in the CFD simulations. The demand for computational power when more than one ship is passing can be the bottleneck if real-time applications should be needed. All the studies as mentioned above adopted the assumption that the encountering or overtaking speed is low. Thus, it can neglect the unsteady free surface wave effect. This assumption significantly reduces the complexity of unsteady ship to ship problems. However, in realistic practice, the encounter overtaking speed is not very low adopted by the researchers mentioned before. The importance of the free surface effect is determined by whether the far-field waves generated by a ship could propagate to the other vessels. The main challenge of imposing a non-rigid free surface condition arises from the speed term in the body boundary condition. The main objective of the chapter is to propose a rational superposition method to handle the unsteady free surface boundary condition containing two or more speed terms, and validate its feasibility in investigating the hydrodynamic behaviour of the ships during overtaking or encountering operations. A superposition method can be applied to account for the velocity field induced by each vessel with its own and unique speed, which has been introduced in Chapter 4. The numerical procedure is extended based on the previous section in Chapter 4. Waves generated and forces (or moments) are calculated when ships are overtaking or passing each other.

5.2 Methodology

5.2.1 Problem definition

Consider two vessels denoted as body B_1 and body B_2 are moving parallel at speed U_1 and $U_2(U_1 > U_2)$. Thus, B_1 eventually overtakes body B_2 in the process. As mentioned previously in Chapter 3, two reference systems are established with the global earth-fixed $o - xyz$ and local body-fixed $o - x_i y_i z_i$, $(i = 1, 2)$ references in Figure 5.1. Then, the separation distance and longitudinal distance between body B_1 and body B_2 are defined as d_t and d_l, respectively. The depth of the water is H. Besides, the velocity potential is time-dependent in the moving frame. It implies the hydrodynamic interaction will be investigated based on the unsteady situation in this section.

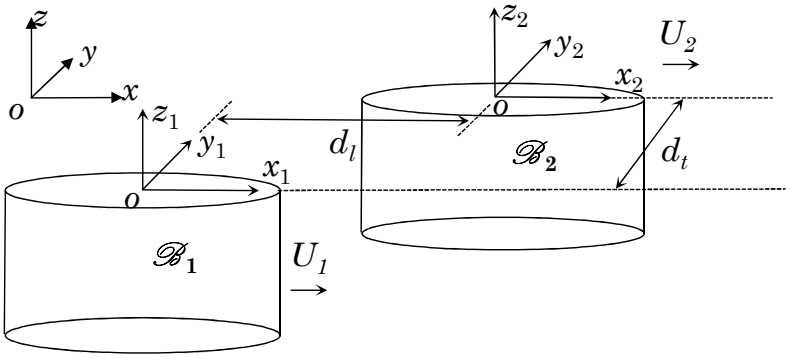

Figure 5.1: Coordinate systems of two bodies in open water.

Boundary element method (BEM) is based on the boundary integral partial differential equation to compute the boundary value problem (Martin. 1987). The advantage of BEM is that it can decrease the computation in 3D into a 2D plane element, which can implement the numerical scheme easily and effectively. $\Phi(x, t)$ is defined as the total velocity potential in the flow domain to describe the disturbance due to the forward motion of the vessels. Assuming the disturbance is small, it represents the total velocity potential produced by the presence of all hulls in the fluid domain in a space-fixed frame to satisfy the following

superposition principle:

$$\Phi(x,t) = \sum_{j=1}^{N} \Phi_j(x,t),\ j = 1,\ 2,\ ...,\ N \tag{5.1}$$

where $\Phi_j(x,\ t)$ is the velocity potential produced by the presence of body B_j moving with U_j, while the remaining ships are stationary in this frame. The coordinate system fixed in the body $x_j = (x_j,\ y_j,\ z_j)(j = 1,\ 2,\ \ldots,\ N)$ is used to solve the boundary value problem (BVP) for multi-players in concurrent motion. The relation between the body- and the space-fixed coordinate system is Galilean transformation.

$$x_j = x - U_j t,\ j = 1,\ 2,\ ...,\ N \tag{5.2}$$

Let $\Phi_j(x_j, t)$ represents $\Phi_j(x,t)$ in the body-fixed coordinate system, the following relation can be obtained

$$\frac{d\Phi_j}{dt} = \Big(\frac{\partial}{\partial t} - U_j \frac{\partial}{\partial x_j}\Big)\varphi_j \tag{5.3}$$

The velocity potential φj satisfies the Laplace equation and body 'exact' boundary condition:

$$\nabla^2 \varphi_j(x_j,\ t) = 0,\ j = 1,\ 2,\ ...,\ N \tag{5.4}$$

$$\frac{\partial \varphi_j}{\partial n} = \delta_{ij} U_j (n_x)_j,\ \text{where } j = 1,\ 2,\ ...,\ N \tag{5.5}$$

The Kronecker delta δ_{ij} is the quantity defined by

$$\delta_{ij} = \begin{cases} 1 & i = j \\ 0 & i \neq j \end{cases} \tag{5.6}$$

The unsteady nonlinear kinematic and dynamic free surface condition can be written as follows

$$(\varphi_j)_t + g(\zeta_j) - (U_j)(\varphi_j)_x + \frac{1}{2}\Big[(\varphi_j)_x \cdot (\varphi_j)_x + (\varphi_j)_y \cdot (\varphi_j)_y - (\varphi_j)_z \cdot (\varphi_j)_z\Big] = 0,\ on\ z = \zeta \tag{5.7}$$

$$(\zeta_j)_t - (U_j)(\zeta_j)_x + (\varphi_j)_x(\zeta_j)_x + (\varphi_j)_y(\zeta_j)_y - (\varphi_j)_z = 0,\ on\ z = \zeta \tag{5.8}$$

ζ_t and ϕ_t are the time derivative of the ζ and ϕ. ζ_x and ϕ_x are the x-derivative of the the ζ and ϕ, respectively as well as the definition in y-derivative and z-derivative. The boundary condition on the sea bottom and sidewalls can be expressed as

$$\frac{\partial \varphi_j}{\partial n} = 0 \tag{5.9}$$

Besides, a radiation condition is imposed on each control surface to ensure that waves vanish at infinity

$$\varphi_j \longrightarrow 0,\ \zeta_j \longrightarrow 0\ as\ \sqrt{x_j^2 + y_j^2} \longrightarrow \infty \tag{5.10}$$

Equation. 5.1 - 5.10 forms a completed set of BVP. Here, only a single speed of ship j appears in the free surface condition in Equation. 5.7 - 5.8, and the coupled problem is decoupled into N independent sets of BVPs. The unsteady free surface boundary condition will be investigated in the time domain by an iteration scheme. Once the unknown potential φ_j is solved, the unsteady pressure components under its individual coordinate system can be obtained from linearized Bernoulli's equation

$$p_j\Big|_{x_j} = -\rho\Big[\frac{\partial \varphi_j}{\partial t}\Big|_{x_j} - U_j \frac{\partial \varphi_j}{\partial x_j}\Big|_{x_j}\Big],\ \text{where } j = 1,\ 2,\ ...,\ N \tag{5.11}$$

Due to the first unsteady term in Equation. 5.11, the total pressure P_j in the coordinate system x_j cannot be expressed directly as the sum of all the pressure components in each local frame. To transfer the pressure from the coordinate system x_i to x_j, the following relation can be obtained

$$\frac{d\varphi_i}{dt}\Big|_{x_j} = \Big(\frac{\partial}{\partial t} - (U_j - U_i)\frac{\partial}{\partial x_i}\Big)\varphi_i\Big|_{x_j},\ \text{where } i,\ j = 1,\ 2,\ ...,\ N \tag{5.12}$$

It should be noted that the partial derivative symbol of the first term in Equation. 5.11 is retained to make it consistent with Equation. 5.3 where the potential is expressed in the body-fixed coordinate system x_j. However, here the body-fixed coordinate system x_j turns to be the reference frame for the other body-fixed coordinate system x_i. Therefore, $\frac{\partial \varphi_j}{\partial t}$ is actually calculated as a total derivative by using Equation. 5.12. The unsteady pressure in the coordinate system x_i ($i = 1,\ 2,\ \ldots,\ N,\ i \neq j$) can then be transferred to

x_j as

$$p_i\Big|_{x_j} = -\rho\Big[\Big(\frac{\partial}{\partial t} - (U_j - U_i)\frac{\partial}{\partial x_i}\Big)\varphi_i\Big|_{x_j} - U_i\frac{\partial \varphi_i}{\partial x_i}\Big|_{x_j}\Big],\ i,\ j = 1,\ 2,\ ...,\ N \tag{5.13}$$

The total pressure P_j in the coordinate system x_j can be written as

$$p_j\Big|_{x_j} = \sum_{i=1}^{N} p_i\Big|_{x_j} = -\rho\sum_{i=1}^{N}\Big(\frac{\partial}{\partial t} - U_j\frac{\partial}{\partial x_i}\Big)\varphi_i\Big|_{x_j},\ i,\ j = 1,\ 2,\ ...,\ N \tag{5.14}$$

Integral the pressure over the hull surface, the forces (or moments) can be obtained by

$$F_i^j = \iint_S p n_i ds,\ j = 1,\ 2,\ ...,\ N \tag{5.15}$$

where $i = 1,\ 2,\ \ldots,\ 6$, representing the force in surge, sway, heave, roll, pitch and yaw directions, and

$$n_i = \begin{cases} n & i = 1,\ 2,\ 3 \\ x \times n & i = 4,\ 5,\ 6 \end{cases} \tag{5.16}$$

5.2.2 Discretization of free surface condition

As discussed before in Chapter 4, the newly numerical method has been developed to simulate the unsteady wave generated by a single ship in shallow water. In this Chapter, this numerical algorithm would be extended to the unsteady interaction problem between two ships. It should be noted that this new algorithm needs to be implemented in different local reference in the body B_1 or body B_2, respectively. To determine the initial condition at $t = 0$, we assume that at the initial stage of ship-to-ship operation, the moving ships are sufficiently far apart so that their interactions are negligible. Thus, the time-dependent non-linearized free surface condition in Equation. 5.7 - 5.8 are linearized to the steady linearized free surface condition (Newman, 1977) in the body-fixed coordinate system can be obtained

$$U_j^2\frac{\partial^2 \varphi_j}{\partial x_j^2} + g\frac{\partial \varphi_j}{\partial z_j} = 0,\ on\ z = 0,\ j = 1,\ 2,\ ...,\ N \tag{5.17}$$

where the subscript j indicates the index of the ship. The time derivatives in the free surface condition have to be discretized. The three-time-level scheme is used to obtain the

first derivatives of φ_j and ζ_j.

$$(\varphi_t)_j^{n+1} = \frac{1}{\Delta t}\Big[\frac{3}{2}(\varphi)_j^{n+1} - 2(\varphi)_j^n + \frac{1}{2}(\varphi)_j^{n-1}\Big] \tag{5.18}$$

$$(\zeta_t)_j^{n+1} = \frac{1}{\Delta t}\Big[\frac{3}{2}(\zeta)_j^{n+1} - 2(\zeta)_j^n + \frac{1}{2}(\zeta)_j^{n-1}\Big] \tag{5.19}$$

At each iterative step k, the linear terms of $x-$derivative in equation 5.20 are approximated implicitly on the left-hand side (LHS) terms. The rest nonlinear terms and cross-derivatives are put on the right-hand sides (RHS) as the knowns for the next iteration $t = t_{n+1}$ to update the wave elevation ζ. The dynamic condition in equation 5.20 is then satisfied through an implicit method using the present solution in Equation. 5.21 to update potential φ at t_{n+1}. All variables are then updated by the latest values from the iteration as k is advanced. Residual errors of time derivatives of $|(\varphi_i^{n+1,k})^* - \varphi_i^{n+1,k}|$ & $|(\zeta_i^{n+1,k})^* - \zeta_i^{n+1,k}|$ can be evaluated. If both the $|(\varphi_i^{n+1,k})^* - \varphi_i^{n+1,k}| < \epsilon$ and $|(\zeta_i^{n+1,k})^* - \zeta_i^{n+1,k}| < \epsilon$, the iteration stops and $\varphi_i^{n+1,k}$ and $\zeta_i^{n+1,k}$ will be used to calculated the pressure. Otherwise, $\varphi_i^{n,k}$ in equation 5.20 will be replaced by $\varphi_i^{n+1,k}$. It is known that the iterative scheme has advantages of high accuracy and good numerical stability. At each iterative step k,

$$\begin{aligned}\frac{3\zeta_j^{n+1,k} - 4\zeta_j^{n,k} + \zeta_j^{n-1,k}}{2\Delta t} - U(t)\cdot(\zeta_x)_j^{n+1,k} = \\ -(\varphi_x)_j^{n,k}\cdot(\zeta_x)_j^{n,k} - (\varphi_y)_j^{n,k}\cdot(\zeta_y)_j^{n,k} + (\varphi_z)_j^{n,k}\end{aligned} \tag{5.20}$$

$$\begin{aligned}\frac{3\varphi_j^{n+1,k} - 4\varphi_j^{n,k} + \varphi_j^{n-1,k}}{2\Delta t} - U(t)\cdot(\varphi_x)_j^{n+1,k} = \\ -g\cdot(\zeta)_j^{n+1,k} - \frac{1}{2}\Big[(\varphi_x\cdot\varphi_x)_j^{n,k} + (\varphi_y\cdot\varphi_y)_j^{n,k} + (\varphi_z\cdot\varphi_z)_j^{n,k}\Big]\end{aligned} \tag{5.21}$$

In which $\varphi_j^{n+1,k}$ and $\zeta_j^{n+1,k}$ are the predicted values of $\varphi_j^{n,k}$ and $\zeta_j^{n,k}$ after the kth iteration. In order to obtain more stable numerical results, the 2nd-order up-wind difference scheme was implemented to obtain the spatial derivatives of the and on the LHS of the Equation 5.20 and 5.21 (Kring, 1994b). The transverse derivatives and the vertical derivatives of the nonlinear items are evaluated by using a central difference scheme. The implicit scheme

is unconditionally stable, and its temporal and spatial accuracy is of second order, *i.e.*, $O(\Delta t^2), O(\Delta x^2, \Delta y^2)$. After the unknown potential φ_j is solved, the simulation for the other unknow potential φ_i in the other body reference i will calculated based on the steady linear FSBC. It is because of the position of the elements distributed on the free surface is only fixed to the body reference j. Calculating the changing free surface in the reference i is very complicated. The unsteady pressure components under its individual coordinate system can be obtained from linearized Bernoulli's Equation 5.14. The wave elevation on the free surface can be obtained from kinematic free-surface boundary condition in Equation. 5.7. Similar to the pressure expression, the total wave elevation can be written as

$$\zeta\Big|_{x_j} = -\frac{1}{g}\sum_{i=1}^{N}\Big(\frac{\partial}{\partial t} - U_j\frac{\partial}{\partial x_i}\Big)\varphi_i\Big|_{x_j},\ i,\ j = 1,\ 2,\ ...,\ N \tag{5.22}$$

5.3 Validation of the two Cylindroids on passing tests

Model-test data on the ship to ship interaction with different speeds is rather rare. To validate the developed numerical method, firstly, two identical cylindroids model in overtaking is simulated. Figure 5.2 is the mesh distribution on the partial computational domain when Model C_1 is overtaking Model C_2. It should be noted that the sidewalls of the tank are not modelled and the longitudinal separation d_l is measured in the body-fixed frame on Model C_2. The main particulars of Model C_1 can be found in Table 5.1. The calculation starts at the position of negtive $d_l/L = -3$ and ends at the position of $d_l/L = 3$ by C_2, which is same as Chapter 3.

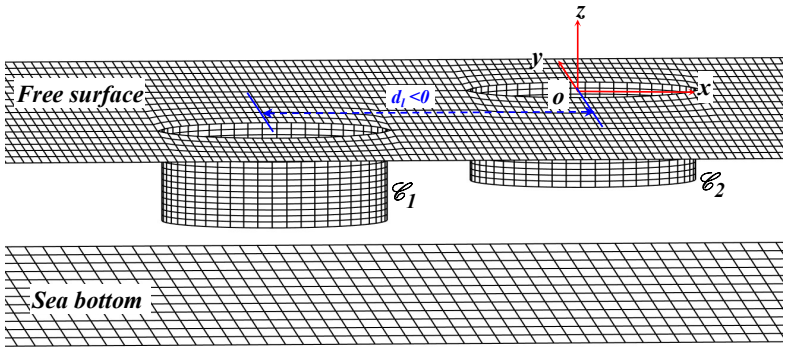

Figure 5.2: Panel distribution on the computation domain of two identical Cylindroids model in overtaking on the sea bottom. There are in total 4544 panels distributed on the total computation domain in this simulation: 2222 panels distributed on the free surface S_F, 782 on each wetted body surface S_H and 756 on the sea bottom S_B. The computational domain is truncated at $2L$ upstream, $2L$ downstream and $0.25L$ sideways with regard to the body-fixed reference frame.

Table 5.1: Principal dimensions of the Cylindroids model

Dimensions Item	Value
Length, L (m)	0.8
Breadth, B (m)	0.1
Draught, D (m)	1.47

The numerical results, comparing with the experimental measurements, are shown in Figure 5.3. Figure 5.3 shows the interaction forces (a) The wave-resistance, (b) the sway force and (c) the yaw moment on Model C_2 at $F_n = 0$ passed by Model C_1 at $Fn = 0.217$ at the water depth $H = 3$ m. Generally, the agreement between present potential flow solver and experimental measurement is very satisfied. There is some shifts in amplitude of C_w and C_n due to the lifting effect does not conclude in this computation. It indicates the developed numerical algorithm is applicable to predict the hydrodynamic interactions between two ships with different forward speeds. It should be also noted that it also compares the nonlinear free surface condition with the linear free surface condition. The results indicate that the nonlinear term in this passing problem is not very important, which can be neglected in the next simulations.

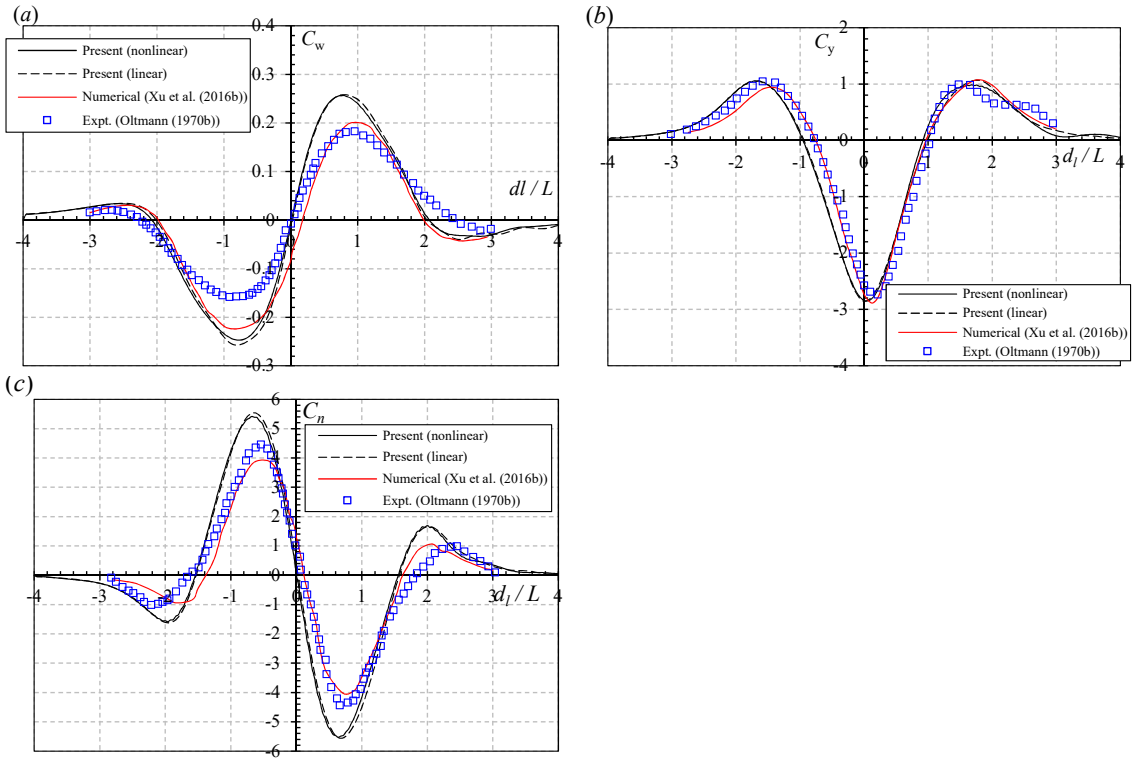

Figure 5.3: (a) The wave-resistance (positive forward), (b) the sway force (positive if repulsive) and (c) the yaw moment (positive if bow repulsed) on C_2 at the $F_n = 0$ passed by C_1 at the $F_n = 0.217$. The water depth $H = 3$ m and the separation distance is $d_t = 5.0B$. The positive dl values denote that C_1 is on the upstream side of C_2. As C_1 moves to the down-stream side, dl becomes negative. EFD results are published by Oltmann (1970) and the numerical results are calculated by the Xu et al. (2016).

5.4 Convergence tests

A convergence study is carried out under the condition of the ratio of water depth to draught $H/D = 2$ and the lateral distance between ships $d_t = 5.0B$. Convergence study of panel number on the body surface is conducted with two sets of grids, *i.e.*, 40×30, 30×20 and 20×10 panels on each of the hull in Figure 5.4. Figure 5.5 shows the result of the convergence study of panel size on the free surface. In view of computation accuracy and efficiency, the second set of grids, that is, 30 × 20 panel is suitable. The time steps of d_t = 0.005, 0.01 and 0.02 are used. Figure 5.6 shows the result converges at the time step d_t = 0.01.

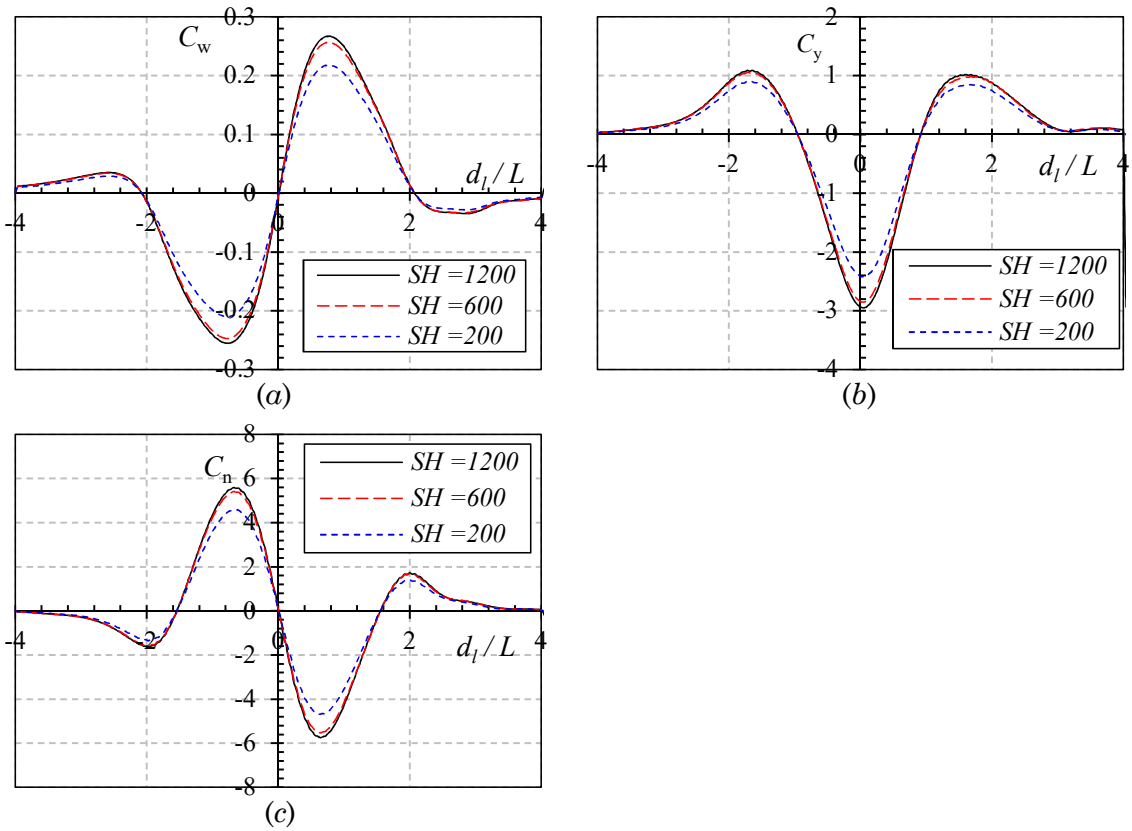

Figure 5.4: Convergence study on the two identical Cylindroids model in passing with different panel number of the body. The Cylindroid 1 passes the Cylindroid 2 with the speed $U = 0.6076$ at the water depth $H/D = 2$.

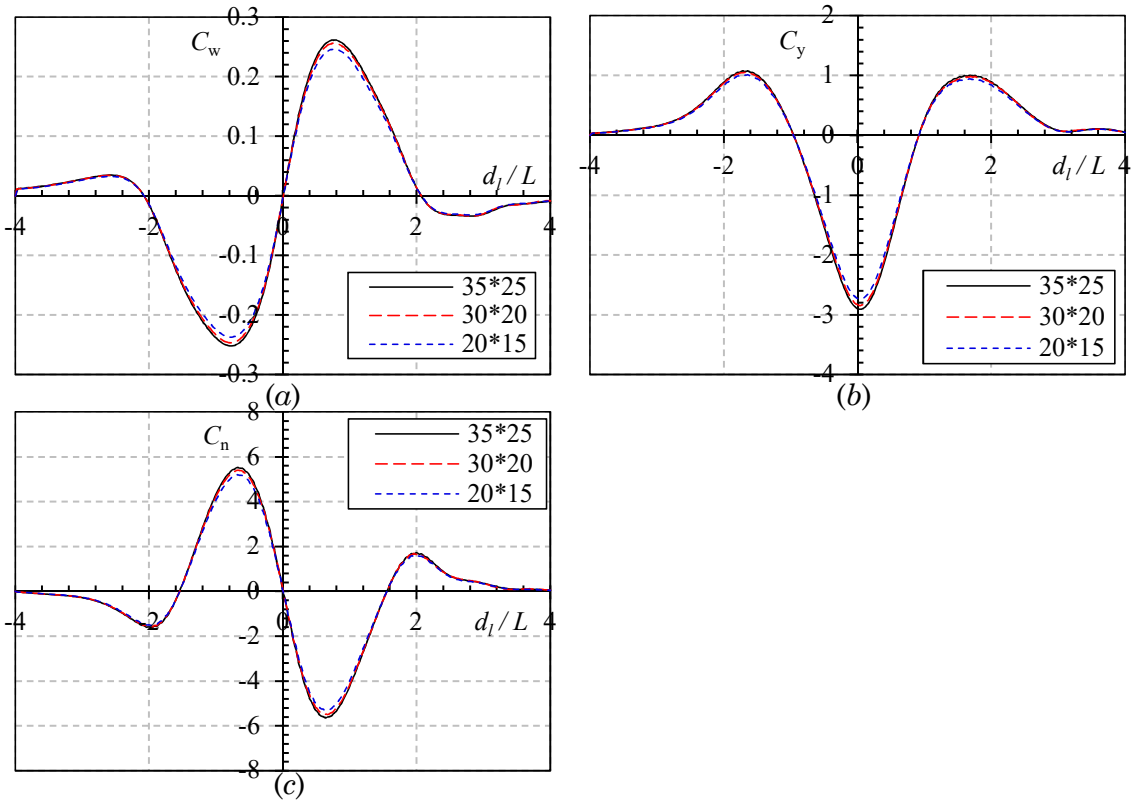

Figure 5.5: Convergence study on the two identical Cylindroids model in passing with different spatial discretization. The Cylindroid 1 passes the Cylindroid 2 with speed $U = 0.6076$ at the water depth $H/D = 2$.

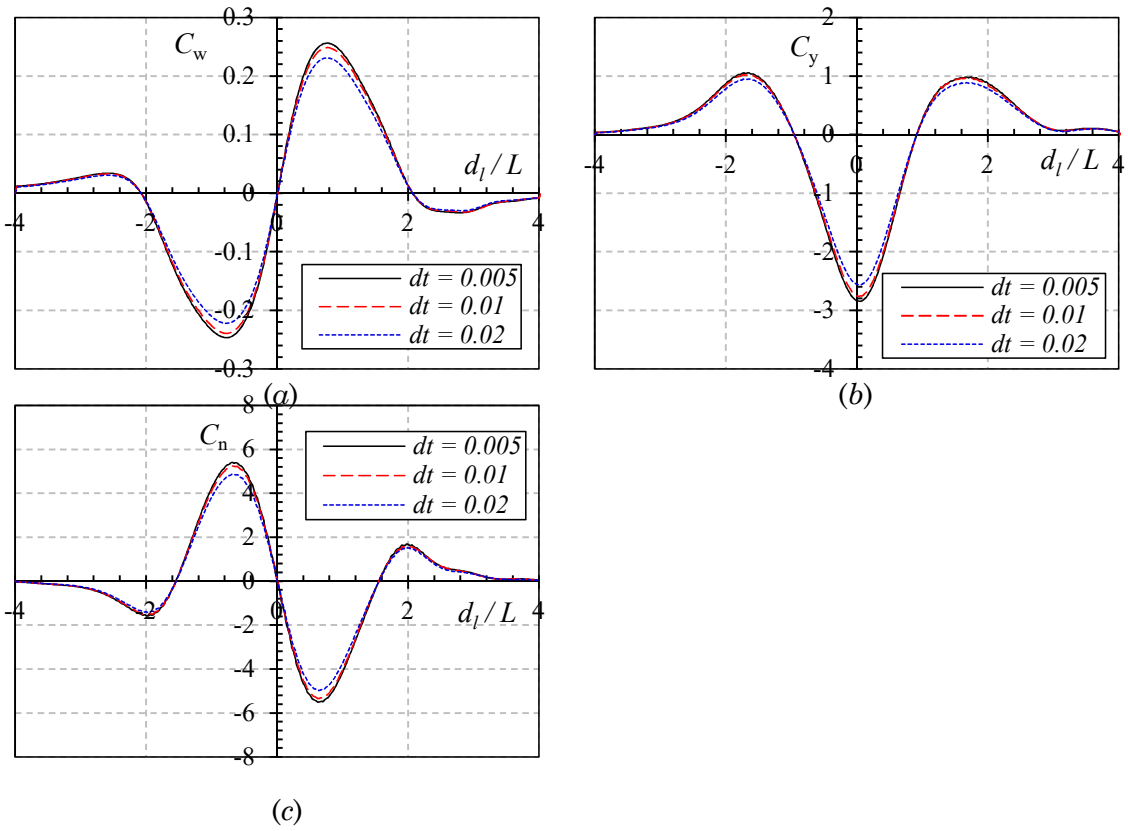

Figure 5.6: Convergence study on the two identical Cylindroids model in passing with different time steps. The Cylindroid model 1 passes the Cylindroid 2 with speed $U = 0.6076$ at the water depth $H/D = 2$.

5.5 Results and discussing

5.5.1 Validation and discussing of two Wigley III hulls on overtaking tests

Passing tests

To validate the effectiveness of the present numerical simulation method, two typical conditions of passing and overtaking without banks are investigated, and the calculated results of hydrodynamic interaction forces are compared with the corresponding results obtained by the slender-body theory or RANS-based CFD method. Figure 5.7 shows the panel distribution on the computation domain of two identical Wigley III hulls in the overtaking or passing process.

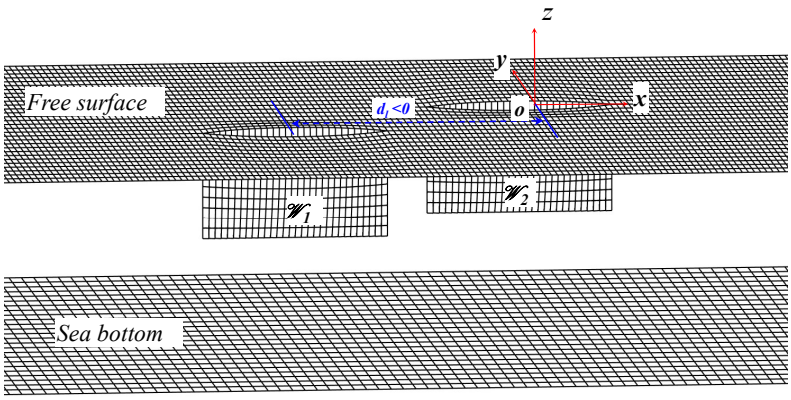

Figure 5.7: Panel distribution on the computation domain of two identical Wigley III hulls in overtaking on the sea bottom. There are in total 4544 panels distributed on the total computation domain in this simulation: 2222 panels distributed on the free surface S_F, 782 on each wetted body surface S_H and 756 on the sea bottom S_B. The computational domain is truncated at $2L$ upstream, $2L$ downstream and $0.25L$ sideways with regard to the body-fixed reference frame.

In Figure 5.8, the present numerical results are compared with those obtained by using the slender-body theory by Tuck and Newman (1976) and the high-order numerical results by the Xu et al. (2017) for a ship W_1 passing by a berthed ship W_2 in unrestricted water. It can be seen that the hydrodynamic interaction forces obtained by the present method agree well with those by using the slender-body theory. It should noted that there is some perturbations at the maxima in the computation which is complicated to explain.

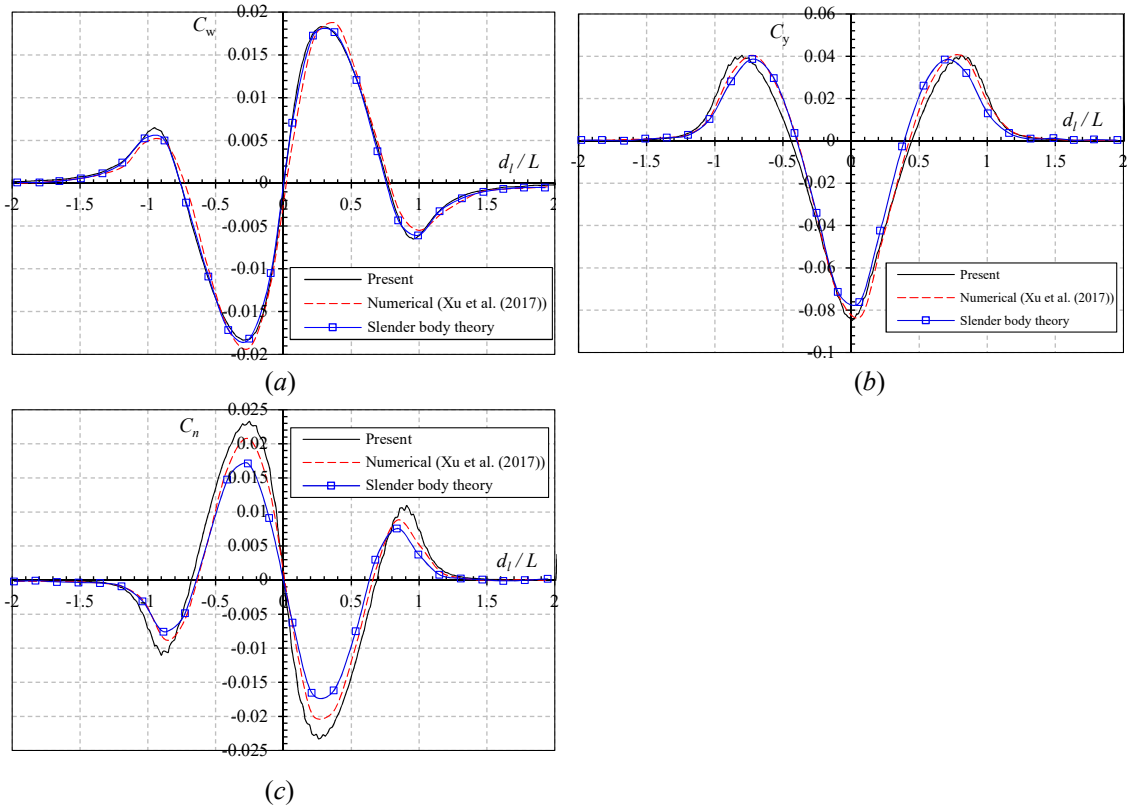

Figure 5.8: (a) The wave-resistance (positive forward), (b) the sway force (positive if repulsive) and (c) the yaw moment (positive if bow repulsed) on W_2 at the $F_n = 0$ passed by W_1 at the $F_n = 0.066$. The separation distance is $d_t = 1.5\ B$ and the water depth is infinite. The positive d_l values denote that W_1 is in the upstream side of W_2. As W_1 moves to the down-stream side, dl becomes negative. EFD results are published by slender body theory by Tuck and Newman (1976) and the numerical results are calculated by Xu et al. (2017).

Overtaking tests

Figure 5.9 shows the comparison of the presented interactions forces on Model W_2 at the F_n = 0.02 overtaken by W_1 at the $F_n = 0.066$ with the numerical results by Xu et al. (2017). The separation distance is $d_t = 2.0B$ and the water depth $H/D = 1.5$. The negative values shown in Figure 5.9.(a) represent the resistance that is opposite to the moving direction, while the positive values represent a thrust, which is the same as the moving direction. An interesting finding is that a large resistance force is observed at d_l/L = -0.5 during the passing and overtaking maneuvering. However, a thrust force (forward) is observed at $d_l/L_E = 0.5$, where the stern of W_1 approaches the midship of W_2 longitudinally. It

can be explained that before overtaking ($-1 < d_l/L < 0$), the presence of faster ship (W_1) accelerates the fluid velocity around the stern area of W_2. As a result, the pressure distributed over ship stern decreases. At the same time, the pressure distributed over the ship bow retains the same level. Increased resistance is expected by pressure integral over the hull surface of W_2. After overtaking ($0 < d_l/L < 1$), the high-pressure area transfers to the ship bow, which will correspondingly lead to a propulsion force. There are some empirical formulas established to solve the interaction moment (Vantorre et al., 2002; Varyani et al., 2002) based on these peaks. However, as those peaks are not predictable, the applicability of those empirical formulas is very limited. It has been found that in the ship-bank and ship-lock problem, the potential flow method fails to predict the sign of yaw moment due to the weak lifting force caused by the cross-flow in the stern (Yuan and Incecik, 2016). However, for the unsteady interaction problem between the ships, the hydrodynamic interaction is much more important than cross-flow effects. The predictions of yaw moment by a potential flow solver are therefore reliable.

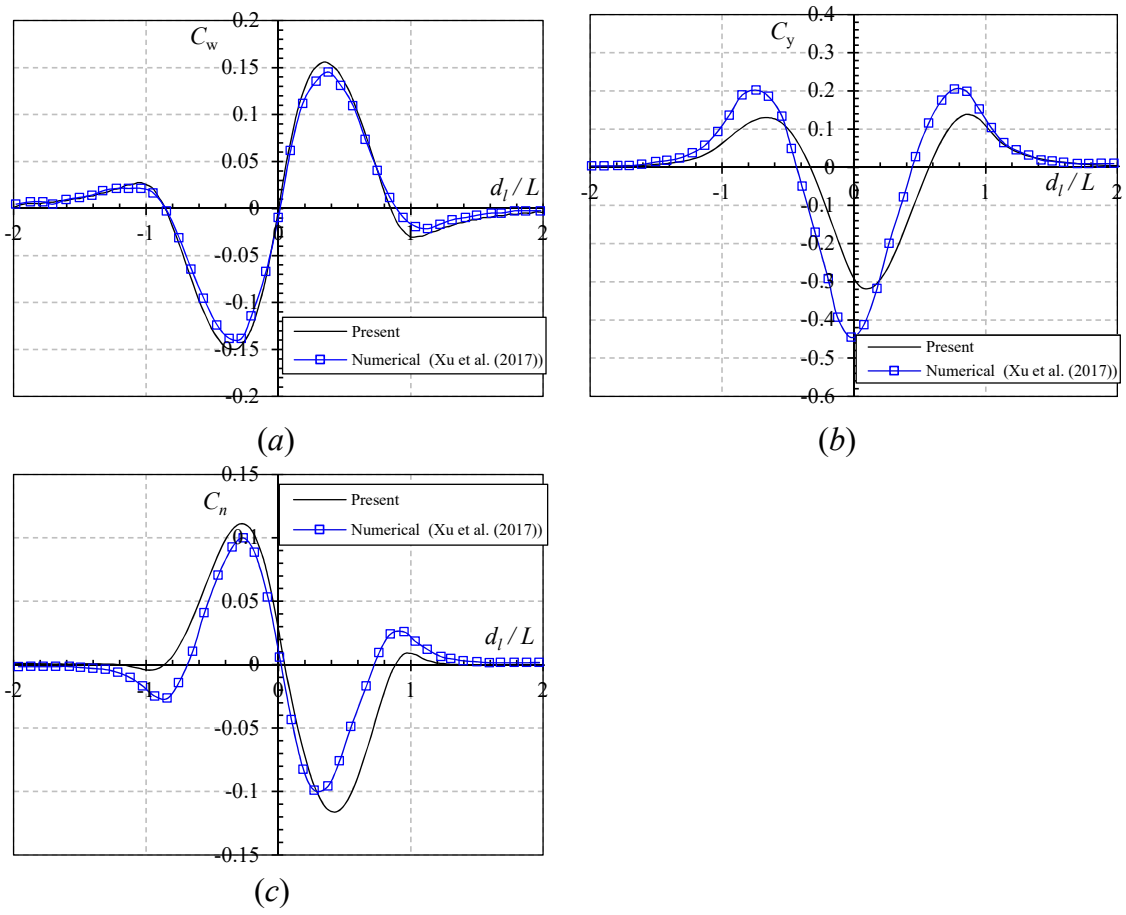

Figure 5.9: (a) The wave-resistance (positive forward), (b) the sway force (positive if repulsive) and (c) the yaw moment (positive if bow repulsed) W_2 at the $F_n = 0.02$ overtaken by W_1 at the $F_n = 0.066$. The separation distance is $d_t = 2.0\ B$ and the water depth H/D =1.5. The numerical results are calculated by Xu et al. (2017).

5.5.2 Parameters study

After validations, the present numerical algorithm with the superposition method can then be extended to investigate the effect of the different speed, separation distance and water depth. Firstly, to examine the effect of the changing speed ratio $\gamma = U1/U2$, computations of overtaking maneuvers are carried out with $F_{n2} = 0.066$, while the value of F_{n1} changes between 0.1 and 0.165. The water depth is H/D =1.5. In Figure 5.10 (a), the normalized longitudinal forces on the W_2 versus increasing instantaneous stagger of various ratio γ can be seen. Meanwhile, In Figure 5.10, the forces/moments acting on the W_2 at higher

ratio γ exhibit much more variations than the cases with lower γ after the overtaking taken place ($d_l/L > 1.0$). At this position, W_2 higher is maneuvering to the W_2 's wake region, the free surface effect in the far-field then can be observed. Besides, the peaks induced by far-field waves are unpredictable. Therefore, the empirical formulas based on low-speed model (Lataire et al., 2012; Vantorre et al., 2002; Varyani et al., 2002) is not applicable to predict the interaction forces when the free surface effect becomes important. It can be concluded that the free surface effects must be taken into account at $\gamma > 2$.

Different ratios of ship speeds

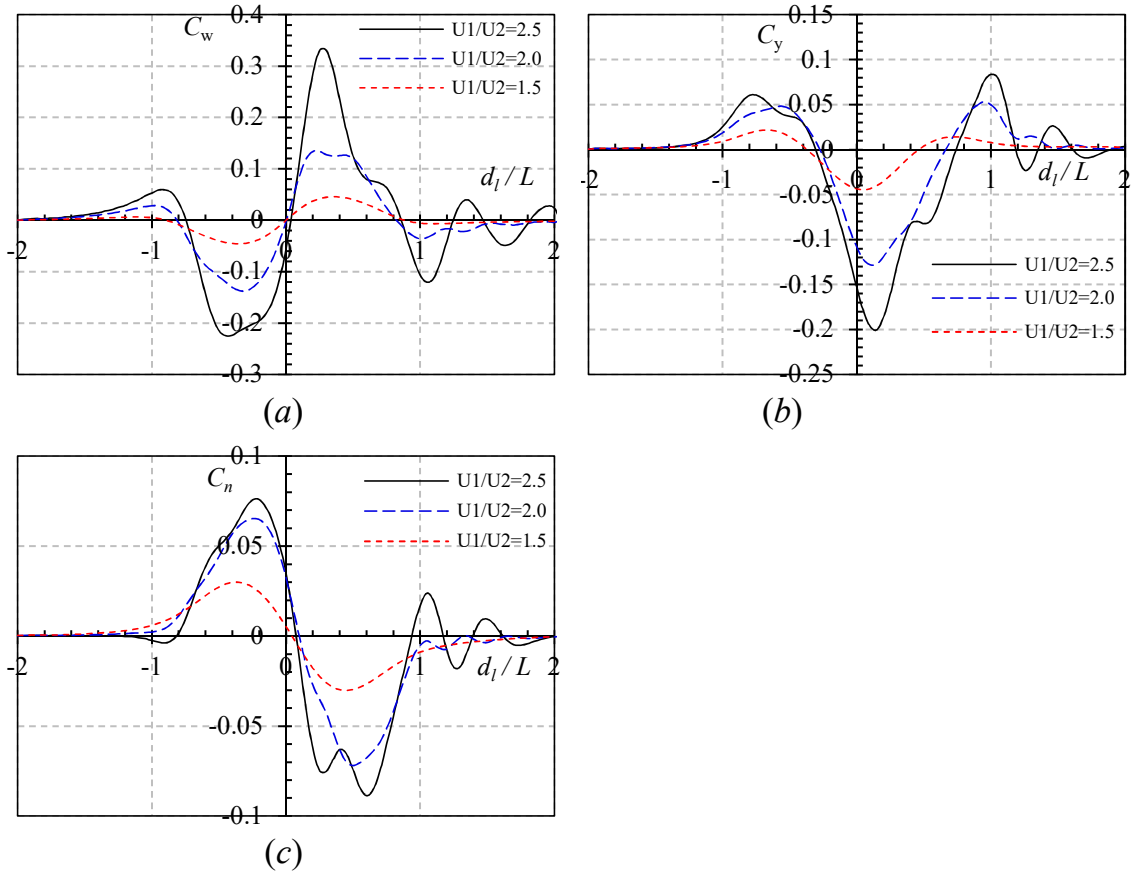

Figure 5.10: (a) The wave-resistance, (b) the sway force and (c) the yaw moment are acting on W_2 at different ratios of ship speeds during overtaking. The separation distance is $d_t = 2.0\ B$ in $H/D = 1.5$.

Different separation distance d_t between two ships

The influence factor of the lateral distance dt between the hulls also plays a crucial role

in hydrodynamic interaction. To analyse and reveal the influences of these factors, a series of calculations are carried out for two vessels in overtaking conditions. The constant speed ratio is $\gamma = U_1/U_2 = 2.0$. The calculations are conducted for $d_t = 2.0B$, $2.5B$, $3.0B$. The water depth is kept unchanged. Figure 5.11 shows the calculation results of the hydrodynamic interaction forces and yaw moment acting on W_2. It can be seen that the changing tendency is the same for different dt. The longitudinal force experiences consecutive decrease and increase. The lateral force is distinguished by initial repulsion, followed by attraction and repulsion again. The yaw moment is characterized by four phases, that is, consecutive bow attraction and bow repulsion. It should be noted that the main difference occurs at the peak points in each curve. These figures reveal that the separation distance between two hulls plays an important role in hydrodynamic interaction, and the magnitudes of the hydrodynamic interaction force and moment decrease with the increase of the lateral distance.

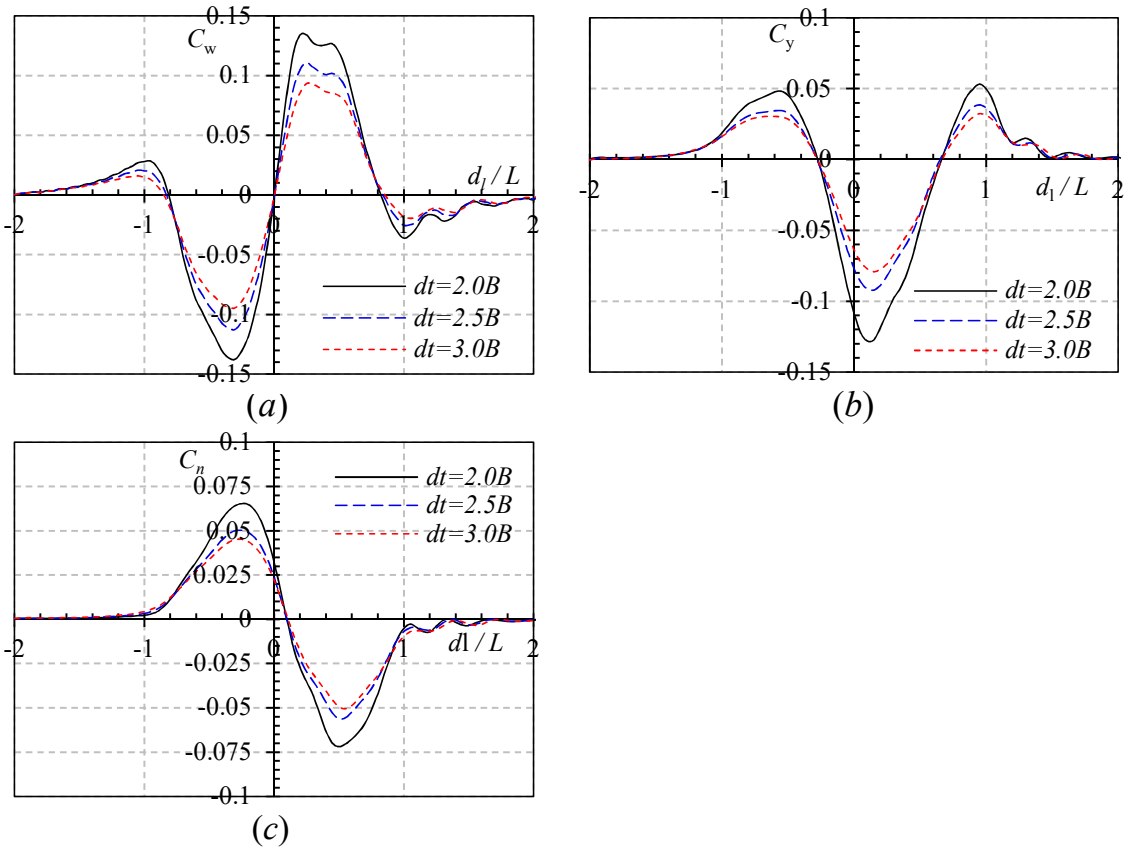

Figure 5.11: (a) The wave-resistance, (b) the sway force and (c) the yaw moment are acting on W_2 at different separation distance during overtaking. The speed ratio is $\gamma = U_1/U_2 = 2.0$ and the $H/D = 1.5$.

Different water depth H/D

To investigate the influence of water depth H/D on the hydrodynamic interaction forces of two ships in overtaking conditions, the calculations are conducted for different ratios of water depth to draught $H/D = 1.5$, 2.0 and 2.5. The lateral distance between the vessels is $d_t = 2.0B$, and the ratio of the $\gamma = U_1/U_2 = 2.0$ is kept unchanged. Figure 5.12 shows the hydrodynamic interaction forces and yaw moment acting on W_2. From the figures, it can be seen that the effect of the water depth on hydrodynamic interaction forces and yaw moment are almost the same as the effect of the separation distance. It reveals that when the ships are in the overtaking process in the restricted waterways, the peak magnitude of the hydrodynamic interaction forces would be amplified.

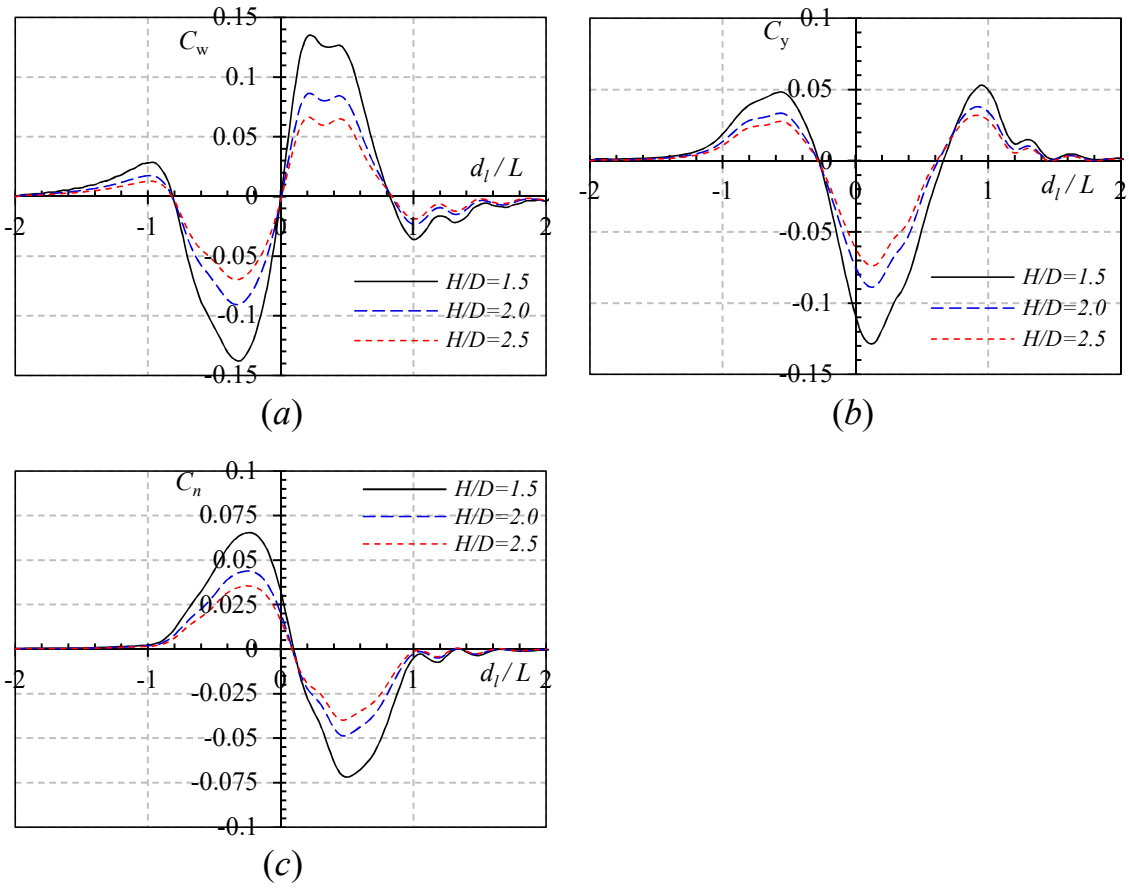

Figure 5.12: (a) The wave-resistance, (b) the sway force and (c) the yaw moment are acting on W_2 at different water depth during overtaking. The speed ratio is $\gamma = U_1/U_2 = 2.0$ and the $H/D = 1.5$.

5.5.3 Wave patterns generated by the two ships in deep and shallow water

Deep water

In this thesis, another important aspect is solving the wave patterns to observe the interference between two sets of ship waves during the overtaking maneuveres. As mentioned before, the far-field effect should not be neglect at high-speed $F_n > 0.2$, such that it would investigate the Froude number of the W_1 keeps constant $F_{n1} = 0.3$, while the value of the ratio in the changes of $\gamma = U_1/U_2 = 1.2$, 1.5 and 2.0. The numerical results of normalised forces/moment at different values γ are depicted in Figure 5.13.

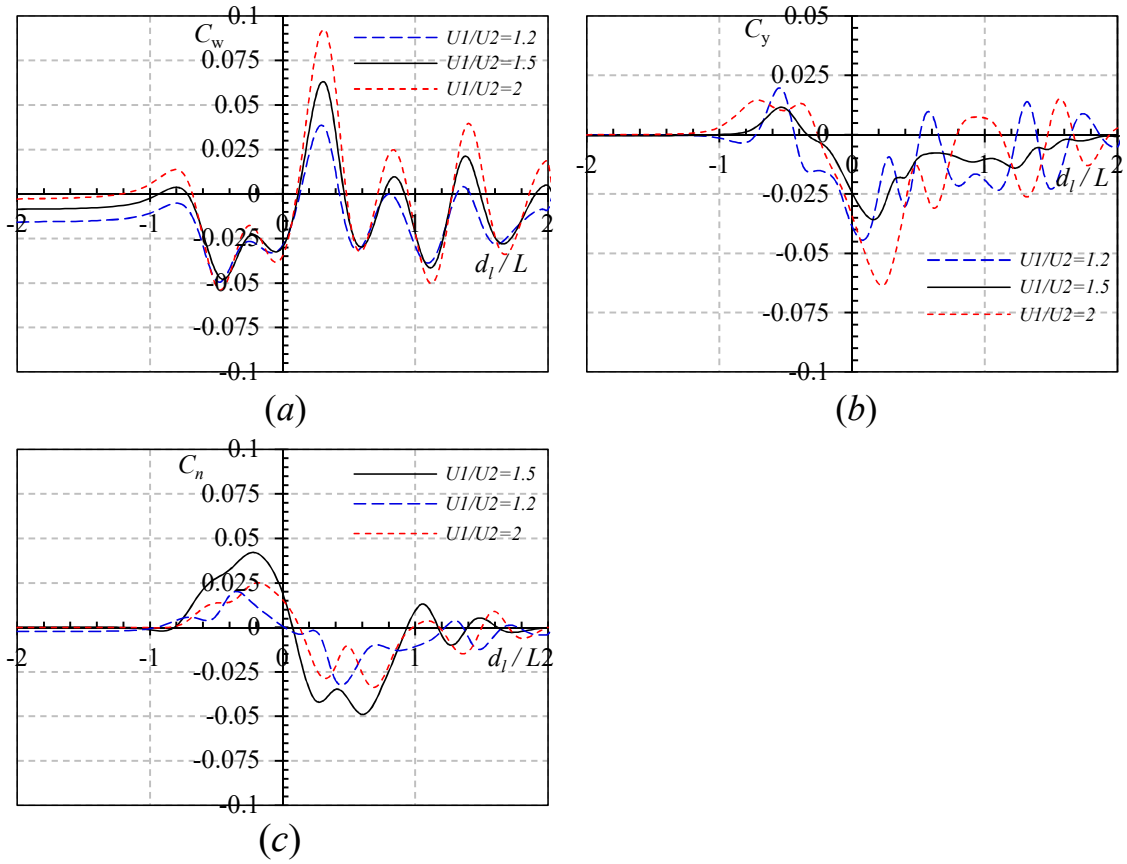

Figure 5.13: Hydrodynamic force and moment acting on W_2 at different ratios of ship speeds during overtaking. The separation distance is $d_t = 2.0B$ and the water depth is infinite.

The coefficient curves exhibit distinct fluctuations when the W_1 overtakes towards the W_2 from -2L to 2L downstream. The amplitude of the fluctuations becomes larger as the W_1 gets closer to the W_2. As the ratio γ increases, The lifting force coefficient C_y and the yaw moment coefficient C_n acting on W_2 with different values γ show insignificant differences in fluctuation phase, while the wave-making resistance Cw keeps the same fluctuation phase.

In order to find how the wave patterns alter the hydrodynamic interaction, we depict the wave flows around the ships at various d_l/L. The instantaneous wave patterns between the ships at various γ during the overtaking process with different configurations are shown in Figure 5.14. It should be noted that the total wave elevation ζ presented is not only the

simple superposition of the waves generated by two individual hulls moving forward. When we calculate the wave elevation produced by W_1, the presence of W_1 is also considered. Typically, W_1 is treated as an obstacle, which is momentarily stationary in the body-fixed frame of W_1. Therefore, the diffraction and reflection by W_1 are considered in the present study. The first significant disturbance occurs when the d_l/L = -0.5 corresponding to Figure 5.14 (a), (e) and (i). The stern of W_2 locates at the divergent wave of W_1 experience larger hydrodynamic forces and moment. Theoretically, it can also be explained by the water wave theory introduced before in Chapter 3. For example, in Figure 5.14 (a), if the starboard of W_2's aft part is in the wave trough, an extra resistance will be added. These reflected waves can be seen clearly when the two ships are in the close stagger position around the d_l/L = 0.3 in Figure 5.14 (c). It can be seen that a significant increase in wave elevations is observed in-between hulls. When the W_2 is overtaken by the W_1, the starboard of W_2 's fore part is in the wave trough region. As a result, the wave resistance is decreasing. With smaller γ as shown in Figure 5.14 (e)-(i), W_2 moves at much slower speeds than the overtaking W_1 generates lower waves; therefore, its wave patterns are almost imperceptible in comparison with those of W_2. As the value of γ keeping decreasing, two hulls generate waves with large different amplitudes and wavelengths. As a result, less wave interference may be achieved, which does not change the wave elevation of the flow field. However, regardless of the values of γ, the free surface on the port of the W_1 is less disturbed by the influence of W_2 during the overtaking process. It can be explained also from the wave energy theory. When the W_2 is wholly or partly in the divergent disturbance region generated by the W_1, the interaction becomes significant. The bow and stern waves interfere in this region, and the wave energy concentrated in this region is usually high, especially when the shipping speed is moderate or high.

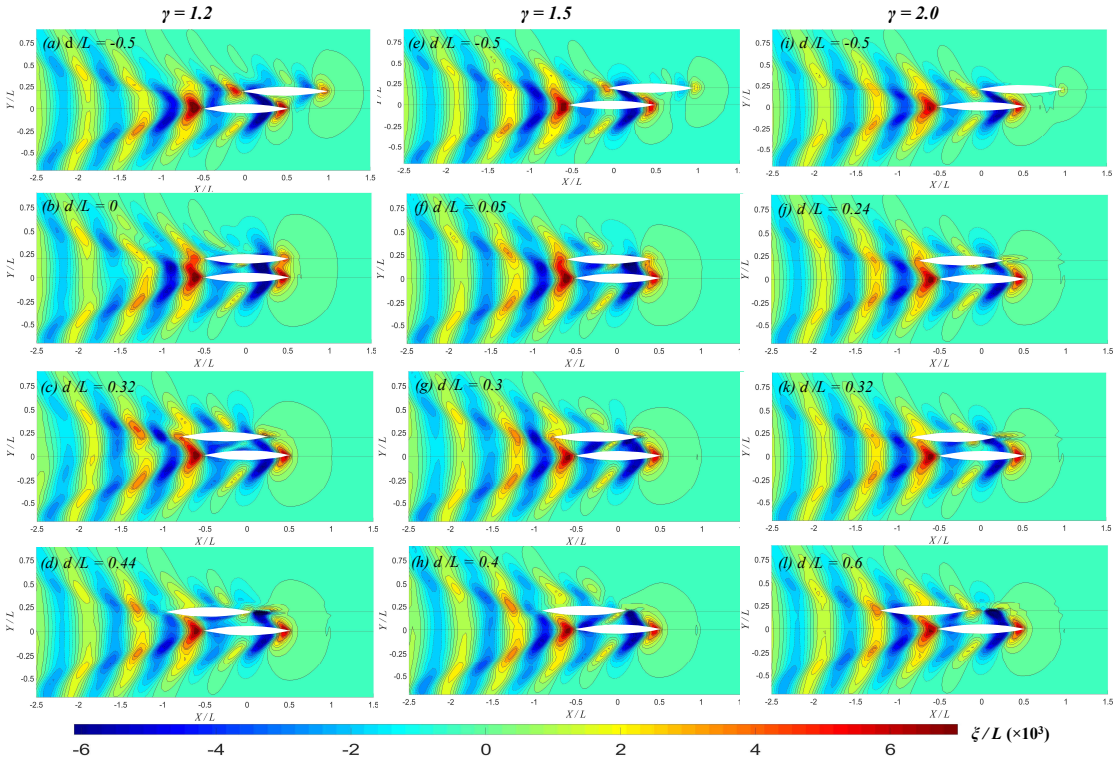

Figure 5.14: The wave patterns when the vessel W_2 at different ratios γ overtaking the vessel W_1. The separation distance is $d_t = 2.0B$ and the water depth is infinite.

Shallow water

Ships maneuvering is relevant in coastal areas or harbour approaches, where the bottom depth is limited, traffic heavier, and where the hydrodynamic interaction effect is increasing hazards. Therefore, the wave patterns between the two ships during overtaking in shallow water would be investigated in this section. The Froude number of the W_1 keeps constant $F_{n1} = 0.3$, and the value of the ratio in the changes of $\gamma = U1/U2 = 1.5$, 2.0 and 3.0. The water depth is defined at the H/D =2.0. The depth Froude number of W_1 is F_{hn1} = 0.85. This speed is very higher for the ship. However, the study in this section is only interested in the very shallow water wave patterns. From Figure 5.15 (a), Comparing with the wave resistance curve of the ship W_2 after being overtaken by W_1 in deep water, the force amplitude induced by the far-field waves is larger and the fluctuation period is increasing. The period of the curves has a relation to the wave length of the divergent wave generated by W_1. The peak value around $d_l/L = 0.3$ in the curves is sensitive to the

ratio γ in the shallow water.

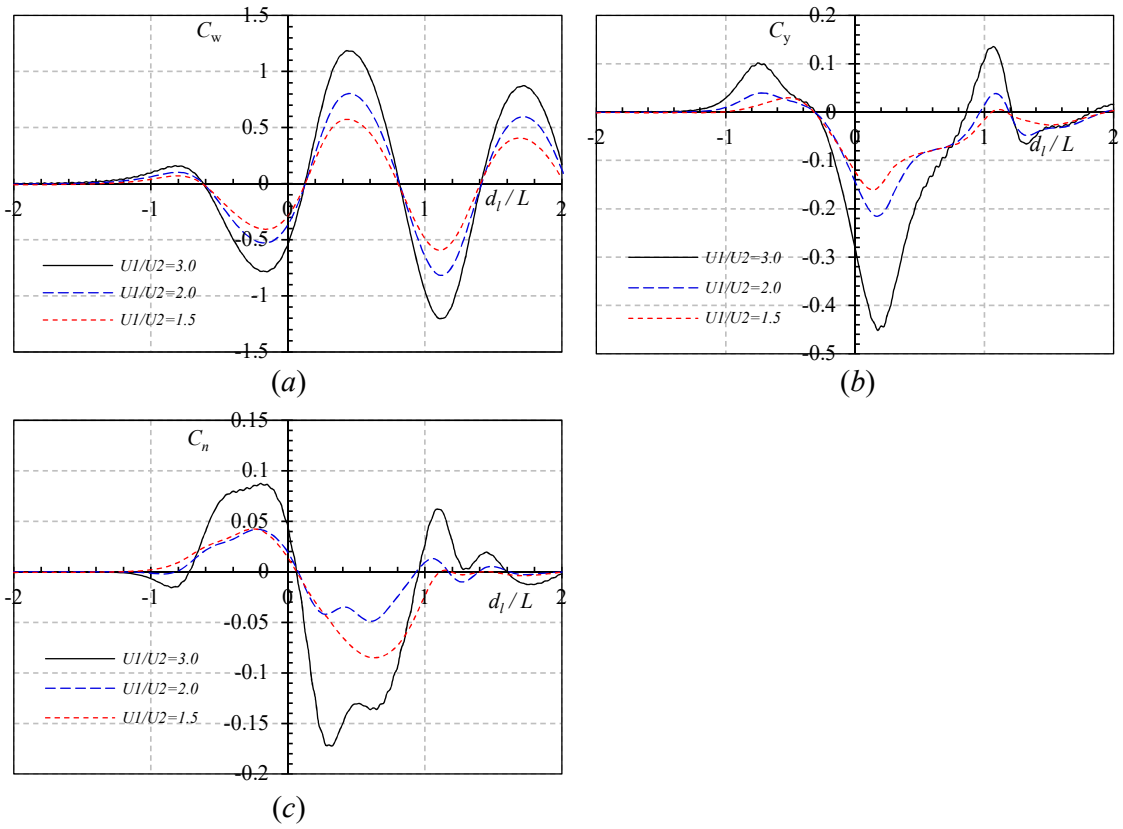

Figure 5.15: Hydrodynamic force and moment acting on W_2 at different ratios of ship speeds during overtaking. The separation distance is $d_t = 2.0B$ and the water depth H/D =2.

Figure 5.16 shows the wave elevation components obtained by the present superposition principle. In Figure 5.16, it shows that the wave patterns almost keep the same during the overtaking process. This is because of the difference in the depth Froude number between two ships being very large. Only at the bow part, the wave region is changing when the ratio γ is at 1.5. Theoretically, it can also be explained by the water wave theory introduced before in Chapter 3. Similarly, as the conclusion from Figure 5.14, in Figure 5.16 (c), (g) and (k), it can be drawn that the starboard of W_2's fore part is in the wave trough, an extra resistance will be added. As a result of the wave pattern has a significant difference distributed in the starboard and port of the W_2 around the dl/L = 0.3. In Figure 5.16 (d), (h) and (l), a significant increase in wave trough is observed

in-between hulls. At a distance, the $d_l/L = 0.44$, the starboard of W_2's fore part is in the wave trough region. As a result, the wave resistance is decreasing. While the pitch moment acting on the W_2 turns to be large. With smaller γ as shown in Figure 5.16 (e)-(i), W_2 moves at much slower speeds than the overtaking W_1 generates insignificant waves; therefore, its wave patterns are almost imperceptible in comparison with those of W_2. As the value of γ keeping decreasing, two hulls generates waves with large different amplitudes and wavelengths.

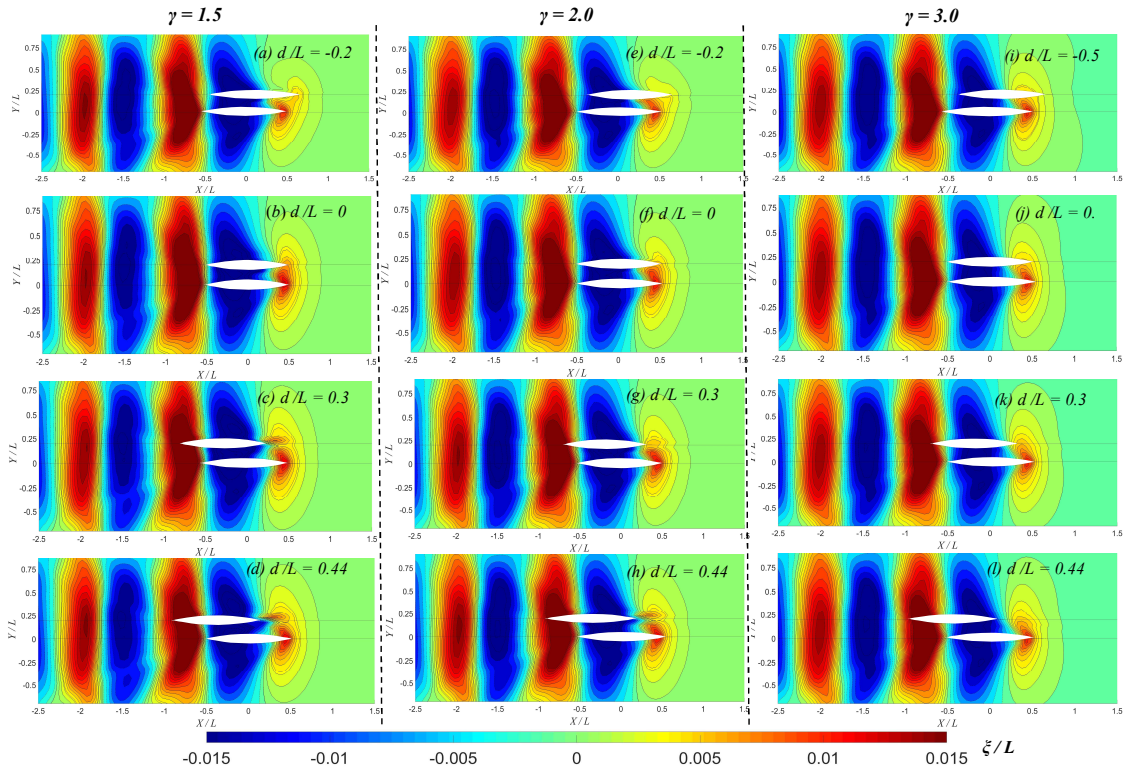

Figure 5.16: The wave pattern of the vessel W_2 at different ratios γ during overtaking at the different positions corresponding to the vessel W_1 in shallow water. The separation distance is $d_t = 2.0$ B and the water depth $H/D = 2$.

5.6 Summary

In the present study, we extend the unsteady potential flow solver to investigate the unsteady phenomenon involved in the interaction between the ships in shallow water. By imposing an unsteady non-linear free surface condition to the BVP, we successfully captured

the unsteady waves initiated by ships during overtaking. The results of the potential-flow panel method are validated by the experimental data and the high-order panel method. The main features of the hydrodynamic interaction in the overtaking process, the maximum lateral force, and the associated instantaneous stagger, are satisfactorily captured by the current computational model with restrained sinkage and trim. When the speed ratio between ships becomes large, it is shown that the ship is overtaken by the other ship experiences loads of larger magnitude and heavy oscillations. It also can also be observed that with the small speed ratio, the forces/moment of both ships approaches those of a steady-state di-hull system. In conclusion, the unsteady free surface around hulls is found to have non-negligible effects on the forces acting on the ships. First, the body of a slower overtaken ship effectively blocks the divergent waves generated by the fast overtaking counterpart. On the other hand, when the tow ships travel with comparable speeds , the wave interference considerably changes the free surface elevations between the two ships.

Chapter 6

Conclusions

6.1 Conclusions

The primary objective of the work presented in this thesis is to study the steady and unsteady wave generated by a single body and multi-bodies travelling in deep and shallow water. The main achievements against the objectives are outlined below:

6.1.1 Steady wave problem

A 3-D Rankine source method based on the potential flow theory with the linear free surface condition is used to investigate the hydrodynamic interaction between the ship model and the false bottom. In numerical study, it investigates the steady false-bottom effect. If the false bottom is infinitely long (the same length as the towing tank), the false-bottom effects can be neglected when the breadth of the false bottom is larger than 15 times of the ship breadth ($Bd/B > 15$). The presently proposed influence width formula by the ITTC, $y_{infl} = 5B(F_h + 1)$, proposes a safe estimation of the necessary width of the false bottom and suggests a false bottom breadth of 15 times the ship breadth at $F_h = 0.5$.
Then, in the study of the mechanism of the steady hydrodynamic interaction between human swimmers, the conclusion has been achieved. When a swimmer was following his competitor at the same speed, he/she could save up to 65 % of the total wave drag at the position where he could utilize the leading swimmer's wave as an aid to improve his swimming performance. In a two-swimmer configuration, the maximum wave drag reduc-

tion of the drafter swimming at $U = 2.16$ m/s is 55% when the partial wave cancellation effect occurs. In a three-swimmer configuration, the wave drag turns to be a thrust force, pushing the drafter forward. According to the wave drag results of a single swimmer, the wave drag contributes $40 - 60\%$ of the total drag when he/she swims with high speed near the free surface. By swimming in an optimum position behind one/two leading swimmers, the drafter could utilize the Kelvin waves as a propelling aid to preserve energy, hence improving the swimming performance.

6.1.2 Unsteady wave problem

The unsteady numerical simulation algorithm has been developed to investigate the unsteady wave generated by a single body and multi-bodies. An implicit finite-difference algorithm and an iterative boundary-integral solution procedure are used to deal with the unsteady nonlinear free surface condition. Generally, the constant speed of a ship model is achieved by towing the model from the rest to the target speed with a given acceleration. The results showed that both the acceleration and water depth have a significant effect on the oscillation amplitude of the unsteady wave resistance. The frequency of the unsteady waves is highly dependent on water depth. The oscillation amplitude and period are mainly determined by three factors: speed, acceleration, and water depth.

In the final Chapter 5, it extends the unsteady potential flow solver to investigate the unsteady phenomenon involved the interaction between the ships in shallow water. By imposing an unsteady non-linear free surface condition to the BVP, it successfully captured the unsteady waves initiated by ships during overtaking. The main features of the hydrodynamic interaction in the overtaking process, the maximum lateral force, and the associated instantaneous stagger, are satisfactorily captured by the current computational model with restrained sinkage and trim. When the speed ratio between ships becomes large, it is shown that the ship is overtaken by the other ship experiences loads of larger magnitude and heavy oscillations. It also can be observed that with the small speed ratio, the forces/moment of both ships approaches those of a steady-state di-hull system. In conclusion, the unsteady free surface around hulls is found to have non-negligible effects on the forces acting on the ships. First, the body of a slower overtaken ship effectively blocks

the divergent waves generated by the fast overtaking counterpart. On the other hand, when the tow ships travel with comparable speeds, the wave interference considerably changes the free surface elevations between the two ships.

6.2 Future work

In this section it outlines the potential future work inspired by the results in this thesis.

- In Chapter 2 & 4, it investigated the steady and unsteady interaction between the ship and the false bottom. In all cases, the thickness of the false bottom was not considered in the thesis. However, in those cases, the dipole might need to be added to simulate the thickness. One potential future problem is to consider the effect of the false bottom's thickness.

- With the application of the superposition method in Chapter 3, it was able to compute multi-swimmers in steady motion. However, it might be more interesting to investigate the unsteady waves generated by the swimmers moving at different speeds. The effect of the unsteady interaction is more realistic to interpret the strategy for the swimming competition due to the unsteady waves.

- In Chapter 4 & 5, it was able to numerically predict the unsteady waves generated by a single ship and multi-bodies by using both the linear and nonlinear FSBC methods. However, the nonlinear method was not fully nonlinear FSBC because of the influence matrix was not updated during each iterative step. As a result, some accuracy would be lost. Therefore, the numerical would be updated for the future studies.

Bibliography

[1] Andrady, A. L., & Neal, M. A. (2009). Applications and societal benefits of plastics. *Philosophical transactions of the Royal Society of London. Series B, Biological sciences*, 364(1526), 1977-1984. doi:10.1098/rstb.2008.0304

[2] Alam, M.-R., Mei, C.C., 2008. Ships advancing near the critical speed in a shallow channel with a randomly uneven bed. *Journal of Fluid Mechanics* 616, 397-417.

[3] Badgerow, J.P., Hainsworth, F.R., 1981. Energy savings through formation flight? A re-examination of the vee formation. *Journal of Theoretical Biology* 93 (1), 41-52.

[4] Berger, M.A., de Groot, G., Hollander, A.P., 1995. Hydrodynamic drag and lift forces on human hand/arm models. *Journal of Biomechanics* 28 (2), 125-133.

[5] Blocken, B., Defraeye, T., Koninckx, E., Carmeliet, J., Hespel, P., 2013. CFD simulations of the aerodynamic drag of two drafting cyclists. *Computers & Fluids 71 (Supplement C)*, 435-445.

[6] Bober, T., Czabanski, B., 1975. Changes in breaststroke techniques under different speed conditions, *Second International Symposium on Biomechanics in Swimming*, pp. 188-193.

[7] Broker, J.P., Kyle, C.R., Burke, E.R., 1999. Racing cyclist power requirements in the 4000-m individual and team pursuits. *Medicine and science in sports and exercise* 31 (11), 1677-1685.

[8] Calisal, S., 1977. Effect of initial acceleration on ship wave pattern and wake survey methods. *Journal of Ship Research* 21 (04), 239-247.

[9] Carrica, P.M., Mofidi, A., Eloot, K., Delefortrie, G., 2016. Direct simulation and experimental study of zigzag maneuver of KCS in shallow water. *Ocean Engineering* 112, 117-133.

[10] Chatard, J.-C., Wilson, B., 2003. Drafting distance in swimming. *Medicine & Science in Sports & Exercise* 35 (7), 1176-1181.

[11] Chen, X.-N., Sharma, S.D., 1995. A slender ship moving at a near-critical speed in a shallow channel. *Journal of Fluid Mechanics* 291, 263-285.

[12] Choi, H.S., Mei, C.C., 1989. Wave resistance and squat of a slender ship moving near the critical speed in restricted water, *5th International Conference on Numerical Ship Hydrodynamics*, Hiroshima, Japan.

[13] Collatz, G., 1963. Potentialtheoretische Untersuchung der hydrodynamischen Wechselwirkung zweier Schiffskörper. *Jahrbuch der Schiffbautechnischen Gesellschaft* 57, 281-389.

[14] Cortesi, M., Fantozzi, S., Di Michele, R., Zamparo, P., Gatta, G., 2014. Passive drag reduction using full-body swimsuits: the role of body position. *The Journal of Strength & Conditioning Research* 28 (11), 3164-3171.

[15] Cortesi, M., Gatta, G., 2015. Effect of The Swimmer's Head Position on Passive Drag. *Journal of human kinetics* 49 (1), 37-45.

[16] Counsilman, J.E., 1968. *The science of swimming*. Prentice Hall.

[17] Cutts, C., Speakman, J., 1994. Energy savings in formation flight of pink-footed geese. *Journal of Experimental Biology* 189 (1), 251-261.

[18] Dand, I., 1975. Some aspects of tug-ship interaction, 4th Int. Tug Conv.

[19] Dawson, C.W., 1977. A practical computer method for solving ship-wave problems, [C].*Proceedings of Second International Conference on Numerical Ship Hydrodynamics*, DTIC Document, 1977:pp. 30-38.

[20] Day, A.H., Clelland, D., Doctors, L.J., 2009. Unsteady finite-depth effects during resistance tests on a ship model in a towing tank. *Journal of Marine Science and Technology* 14 (3), 387-397.

[21] Doctors, L., Beck, R., 1987. Convergence properties of the Neumann-Kelvin problem for a submerged body. *Journal of ship research* 31 (4).

[22] Doctors, L.J., 1975. The experimental wave resistance of an accelerating two-dimensional pressure distribution. *Journal of Fluid Mechanics* 72 (3), 513-527.

[23] Doctors, L.J., Day, A.H., Clelland, D., 2008. Unsteady effects during resistance tests on a ship model in a towing tank. *Journal of Ship Research* 52 (4), 263-273.

[24] Enger, S., Perić, M., Perić, R., 2010. Simulation of flow around KCS-hull, *Proceedings from Gothenburg 2010—A Workshop on Numerical Ship Hydrodynamics*, Gothenburg.

[25] Faltinsen, O.M., 2005. Hydrodynamics of high-speed marine vehicles. *Cambridge university press*.

[26] Farell, C., Guven, O., 1973. On the experimental determination of the resistance components of a submerged spheroid. *Journal of ship research* 17 (2).

[27] Fish, F.E., 1994. Energy conservation by formation swimming: metabolic evidence from ducklings. *Mechanics and physiology of animal swimming*, 193-204.

[28] Fish, F.E., 1995. Kinematics of ducklings swimming in formation: consequences of position. *Journal of Experimental Zoology Part A: Ecological Genetics and Physiology* 273 (1), 1-11.

[29] Gatta, G., Zamparo, P., Cortesi, M., 2013. Effect of swim cap model on passive drag. The *Journal of Strength & Conditioning Research* 27 (10), 2904-2908.

[30] Gourlay, T., 2008. Slender-body methods for predicting ship squat. *Ocean Engineering* 35 (2), 191-200.

[31] Hainsworth, F.R., 1987. Precision and dynamics of positioning by Canada geese flying in formation. *Journal of Experimental Biology* 128 (1), 445-462.

[32] Hess, J.L., Smith, A.M., 1964. Calculation of non-lifting potential flow about arbitrary three-dimensional bodies. *Douglas Aircraft Co Long Beach CA*.

[33] Huang, F., Yang, C., Noblesse, F., 2013. Numerical implementation and validation of the Neumann–Michell theory of ship waves. *European Journal of Mechanics-B/Fluids* 42, 47-68.

[34] Huijing, P., Toussaint, H., Mackay, R., Vervoon, K., Clarys, J., Hollander, A., 1988. Active drag related to body dimensions. *Swimming science* V, 31-37.

[35] Hummel, D., 1983. Aerodynamic aspects of formation flight in birds. *Journal of Theoretical Biology* 104 (3), 321-347.

[36] ITTC, 2011. Resistance Test, *ITTC: Recommended Procedures and Guidelines*: 7.5-02-02-02.

[37] ITTC, R.P., 2017. Guidelines: Testing and Extrapolation Methods: Resistance-Uncertainty Analysis, Example for Resistance Test. *ITTC Recommended Procedures and Guidelines, Procedure 7.5-02-02.*

[38] Kajitani, H., Miyata, H., Ikehata, M., Tanaka, H., Adachi, H., Namimatsu, M., Ogiwara, S., 1983. *The summary of the cooperative experiment on Wigley parabolic model in Japan.* TOKYO UNIV (JAPAN).

[39] Kara, F., 2000. Time domain hydrodynamics and hydroelastic analysis of floating bodies with forward speed. *SSRC University of Strathclyde*, Glasgow.

[40] Kijima, K., Nakiri, Y., 1990. Prediction method of ship maneuvrability in deep and shallow waters, in: Cross, C.S.J. (Ed.), *Marine Simulation and Ship Maneuvrability*, Tokyo, Japan, p. p.311.

[41] Kijima, K., Yasukawa, H., 1984. Maneuvrability of ships in narrow waterway. *Journal of the Society of Naval Architects of Japa*n 1984 (156), 171-179.

[42] King, B., 1987. Time-domain analysis of wave exciting forces on ships and bodies. *PhD thesis, University of Michigan.*

[43] King, B.K., Beck, R.F., Magee, A.R., Seakeeping calculations with forward speed using time domain analysis, *Proc. 17th Symp. on Naval Hydrodynamics* (1988) pp. 577-596.

[44] Kjendlie, P.-L., Stallman, R., 2011. Morphology and swimming performance. World Book of Swimming. *From Science to Performance*. New York: Nova, 203-222.

[45] Koeltzsch, K., Dinkelacker, A., Grundmann, R., 2002. Flow over convergent and divergent wall riblets. *Experiments in fluids* 33 (2), 346-350.

[46] Korsmeyer, F.T., Lee, C.-H., Newman, J., N., 1993. Computation of Ship Interaction Forces in Restricted Waters. *Journal of Ship Researc*h 37 (4), 298-306.

[47] Kring, D.C., 1994. Time domain ship motions by a three-dimensional Rankine panel method. *PhD Thesis*.

[48] Kyle, C.R., 1979. Reduction of wind resistance and power output of racing cyclists and runners travelling in groups. *Ergonomics* 22 (4), 387-397.

[49] Lang, T.G., 1966. Hydrodynamic analysis of cetacean performance. *Whales, dolphins and porpoises*, 410-432.

[50] Lataire, E., Vantorre, M., Delefortrie, G., Candries, M., 2012. Mathematical modelling of forces acting on ships during lightering operations. *Ocean Engineering* 55, 101-115.

[51] Lewis, F.M., 1929. The inertia of the water surrounding a vibrating ship. *SNAME* 37, 1-20.

[52] Li, Y., Sclavounos, P.D., 2002. Three-dimensional nonlinear solitary waves in shallow water generated by an advancing disturbance. *Journal of Fluid Mechanics* 470, 383-410.

[53] Liao, J.C., Beal, D.N., Lauder, G.V., Triantafyllou, M.S., 2003. Fish exploiting vortices decrease muscle activity. *Science* 302 (5650), 1566-1569.

[54] Lissaman, P., Shollenberger, C.A., 1970. Formation flight of birds. *Science* 168 (3934), 1003-1005.

[55] Lunde, J.K., 1951. on the linearized theory of wave resistance for displacement ships in steady and accelerated motion. *Transactions of the Society of Naval Architects and Marine Engineers*, 59, 25-76,.

[56] Lyttle, A., Blanksby, B., Elliott, B., Lloyd, D., 1999. Optimal depth for streamlined gliding. *Biomechanics and medicine in swimming VIII*, 165-170.

[57] Lyttle, A.D., Blanksby, B., Elliot, B., Lloyd, D.G., 1998. The effect of depth and velocity on drag during the streamlined guide. *Journal of Swimming Research* 13, 15-22.

[58] Maeng, J.-S., Park, J.-H., Jang, S.-M., Han, S.-Y., 2013. A modeling approach to energy savings of flying Canada geese using computational fluid dynamics. *Journal of Theoretical Biology* 320, 76-85.

[59] Maglisho, E., 1982. Swimming faster. *Palo Alto*, Mayfield.

[60] Marinho, D.A., Rouboa, A.I., Alves, F.B., Vilas-Boas, J.P., Machado, L., Reis, V.M., Silva, A.J., 2009. Hydrodynamic analysis of different thumb positions in swimming. *Journal of sports science & medicine* 8 (1), 58.

[61] May, R.M., 1979. Flight formations in geese and other birds. *Nature* 282, 778-780.

[62] Michell, J.H., 1898. XI. The wave-resistance of a ship. The London, Edinburgh, and Dublin *Philosophical Magazine and Journal of Science* 45 (272), 106-123.

[63] Mollendorf, J.C., ALBERT C TERMIN, I., Oppenheim, E., Pendergast, D.R., 2004. Effect of swim suit design on passive drag. *Medicine & Science in Sports & Exercise* 36 (6), 1029-1035.

[64] Mousaviraad, S.M., Sadat-Hosseini, S.H., Stern, F., 2016. Ship–ship interactions in calm water and waves. Part 1: analysis of the experimental data. *Ocean Engineering* 111, 615-626.

[65] Mucha, P., Deng, G., Gourlay, T., Moctar, E., Ould, B., 2016. Validation studies on numerical prediction of ship squat and resistance in shallow water, *4th MASHCON International Conference on Ship Maneuvring in Shallow and Confined Water with special focus on Ship Bottom Interaction*, Elbcampus, Hamburg, Germany, pp. 122-133.

[66] Nakos, D.E., 1990. Ship wave patterns and motions by a three dimensional Rankine panel method.

[67] Nakos, D.E., Kring, D., Sclavounos, P.D., 1994. Rankine panel methods for transient free-surface flows.

[68] Newman, J.N., 1977. Marine hydrodynamics. *MIT press.*

[69] Newman, J.N., 1985. Transient axisymmetric motion of a floating cylinder. *Journal of Fluid Mechanics* 157, 17-33.

[70] Oeffner, J., Lauder, G.V., 2012. The hydrodynamic function of shark skin and two biomimetic applications. *Journal of Experimental Biology* 215 (5), 785-795.

[71] Ohring, S., Telste, J., 1997. Numerical solutions of transient three-dimensional ship-wave problems, *Proceedings of the Second International Conference on Numerical Ship Hydrodynamics*, University of California, Berkeley, September 1977: pp.88.

[72] Olds, T., 1998. The mathematics of breaking away and chasing in cycling. *European journal of applied physiology and occupational physiology* 77 (6), 492-497.

[73] Oltmann, P., 1970. Experimentelle Untersuchung der hydrodynamischen Wechselwirkung schiffsähnlicher Körper. *Schiff Hafen* 22, 701-709.

[74] Peters, A.S., 1949. A new treatment of the ship wave problem. *Communications on pure and applied mathematics* 2 (2-3), 123-148.

[75] Pinkster, J.A., 2004. The influence of a free surface on passing ship effects. *International Shipbuilding Progress* 51 (4), 313-338.

[76] Polidori, G., Taiar, R., Fohanno, S., Mai, T., Lodini, A., 2006. Skin-friction drag analysis from the forced convection modeling in simplified underwater swimming. *Journal of Biomechanics* 39 (13), 2535-2541.

[77] Portugal, S.J., Hubel, T.Y., Fritz, J., Heese, S., Trobe, D., Voelkl, B., Hailes, S., Wilson, A.M., Usherwood, J.R., 2014. Upwash exploitation and downwash avoidance by flap phasing in ibis formation flight. *Nature* 505 (7483), 399-402.

[78] Raven, H.C., 1998. A solution method for the nonlinear ship wave resistance problem, *PhD thesis*, Technische Universiteit Delft.

[79] Saha, G.K., Suzuki, K., Kai, H., 2004. Hydrodynamic optimization of ship hull forms in shallow water. *Journal of Marine Science and Technology* 9 (2), 51-62.

[80] Salvesen, N., Tuck, E.O., Faltinsen, O., 1970. Ship motions and sea loads.[J]. *Trans. of Society of Naval Architects and Marine Engineers*, 1970, 78:250-287.

[81] Schultz, M.P., 2007. Effects of coating roughness and biofouling on ship resistance and powering. *Biofouling* 23 (5), 331-341.

[82] Sclavounos, P.D., Nakos, D.E., Stability analysis of panel methods for free-surface flows with forward speed,*Symposium on Naval Hydrodynamics, 17th* Location: The Hague, Netherlands pp. 173-193.

[83] Shen, Z., Wan, D., Carrica, P.M., 2014. RANS simulations of free maneuvers with moving rudders and propellers using overset grids in OpenFOAM, *SIMMAN workshop on Verification and Validation of Ship Maneuvering Simulation Methods*. Presented at the SIMMAN workshop on Verification and Validation of Ship Maneuvering Simulation Methods, Lyngby, Denmark.

[84] Simman, 2014. Workshop on Verification and Validation of Ship Maneuvring Simulation Methods, *simman2014.dk*, Lyngby, Denmark.

[85] Soding, H., 1997. Drastic resistance reductions in catamarans by staggered hulls. *Proceedings of FAST'97*, Sydney, 225-230.

[86] Söding, H., Conrad, F., 2005. Analysis of overtaking maneuvres in a narrow waterway. *Ship Technology Research* 52, 189-193.

[87] Sun, X., Yan, X., Wu, B., Song, X., 2013. Analysis of the operational energy efficiency for inland river ships. *Transportation Research Part D: Transport and Environment* 22, 34-39.

[88] Tarafder, S.M., Suzuki, K., 2008. Wave-making resistance of a catamaran hull in shallow water using a potential-based panel method. *Journal of Ship Research* 52 (1), 16-29.

[89] Terziev, M., Tezdogan, T., Oguz, E., Gourlay, T., Demirel, Y.K., Incecik, A., 2018. Numerical investigation of the behaviour and performance of ships advancing through restricted shallow waters. *Journal of Fluids and Structures* 76, 185-215.

[90] Torsvik, T., Dysthe, K., Pedersen, G., 2006. Influence of variable Froude number on waves generated by ships in shallow water. *Physics of Fluids* 18 (6), 062102.

[91] Toussaint, H., De Groot, G., Savelberg, H., Vervoorn, K., Hollander, A., van Ingen Schenau, G., 1988. Active drag related to velocity in male and female swimmers. *Journal of Biomechanics* 21 (5), 435-438.

[92] Toussaint, H., Truijens, M., 2005. Biomechanical aspects of peak performance in human swimming. *Animal Biology* 55 (1), 17-40.

[93] Toussaint, H.M., Beek, P.J., 1992. Biomechanics of competitive front crawl swimming. *Sports medicine* 13 (1), 8-24.

[94] Toussaint, H.M., Bruinink, L., Coster, R., De Looze, M., Van Rossem, B., Van Veenen, R., De Groot, G., 1989. *Effect of a triathlon wet suit on drag during swimming. Med Sci Sports Exerc* 21 (3), 325-328.

[95] Toussaint, H.M., Truijens, M., Elzinga, M.J., de Ven, A.V., de best, H., Snabel, B., de Groot, G., 2002a. Swimming: Effect of a fast-skin^{TM}'body'suit on drag during front crawl swimming. *Sports Biomechanics* 1 (1), 1-10.

[96] Toussaint, H.M., van Stralen, M., Stevens, E., 2002b. Wave drag in front crawl swimming, *ISBS-Conference Proceedings Archive.*

[97] Tuck, E., 1987. Wave resistance of thin ships and catamarans. *Applied Mathematics Report* T8701.

[98] Tuck, E., Newman, J., 1976. Hydrodynamic interactions between ships, *Symposium on Naval Hydrodynamics, 10th, Proceeding*, Pap and Discuss, Cambridge, Mass, June 24-28, 1974.

[99] Tuck, E.O., 1966a. Shallow-water flows past slender bodies. *Journal of Fluid Mechanics* 26 (1), 81-95.

[100] Tuck, E.O., Lazauskas, L., 1998. Optimum hull spacing of a family of multihulls, *J.ship technology research*, 1998,45:180-195.

[101] Tuck, E.O., Newman, J.N., 1974. Hydrodynamic interactions between ships, *Proceedings of 10th Symposium on Naval Hydrodynamics*, Cambridge, MA, USA, pp. 35-70.

[102] Vantorre, M., 2003. Review of practical methods for assessing shallow and restricted water effects, *International Conference on Marine Simulation and Ship Maneuverability (MARSIM)*. Kanazawa, Japan. WS-4-1-WS-4-11.

[103] Vantorre, M., Verzhbitskaya, E., Laforce, E., 2002. Model test based formulations of ship-ship interaction forces. *Ship Technology Research* 49, 124-141.

[104] Varyani, K.S., McGregor, R., Wold, P., 1998. *Interactive forces and moments between several ships meeting in confined waters. Control Engineering Practice* 6 (5), 635-642.

[105] Varyani, K.S., McGregor, R., Wold, P., 2002. Identification of trends in extremes of sway–yaw interference for several ships meeting in restricted waters. *Ship Technology Research* 49, 174-191.

[106] Vennell, R., Pease, D., Wilson, B., 2006. Wave drag on human swimmers. *Journal of Biomechanics* 39 (4), 664-671.

[107] Vilas-Boas, J.P., Ramos, R.J., Fernandes, R.J., Silva, A.J., Rouboa, A.I., Machado, L., Barbosa, T.M., Marinho, D.A., 2015. Hydrodynamic analysis of different finger positions in swimming: a computational fluid dynamics approach. *Journal of applied biomechanics* 31 (1), 48-55.

[108] Vorontsov, A., Rumyantsev, V., 2000. Resistive Forces in Swimming. *Biomechanics in Sport: Performance Enhancement and Injury Prevention*, 184-204.

[109] Webb, A., Banks, J., Phillips, C., Hudson, D., Taunton, D., Turnock, S., 2011. Prediction of passive and active drag in swimming. *Procedia Engineering* 13, 133-140.

[110] Wehausen, J.V., 1961. Effect of the initial acceleration upon the wave resistance of ship models. *CALIFORNIA UNIV BERKELEY INST OF ENGINEERING RESEARCH.*

[111] Wehausen, J.V., 1964. Effect of the Initial Acceleration Upon the Wave Resistance of Ship Models. *Journal of Ship Research* 8 (01), 38-50.

[112] Weihs, D., 1973. Hydromechanics of fish schooling. *Nature* 241 (5387), 290-291.

[113] Weihs, D., 2004. The hydrodynamics of dolphin drafting. *Journal of Biology* 3 (2), 8.

[114] Weimerskirch, H., Martin, J., Clerquin, Y., Alexandre, P., Jiraskova, S., 2001. Energy saving in flight formation. *Nature* 413, 697.

[115] Westerweel, J., Aslan, K., Pennings, P., Yilmaz, B., 2016. Advantage of a lead swimmer in drafting. *arXiv preprint arXiv:1610.10082.*

[116] Williams, T., Friedl, W., Fong, M., Yamada, R., Sedivy, P., Haun, J., 1992. Travel at low energetic cost by swimming and wave-riding bottlenose dolphins. *Nature* 355 (6363), 821.

[117] Xiang, X., Faltinsen, O.M., 2010. Maneuvering of Two Interacting Ships in Calm Water, *11th International Symposium on Practical Design of Ships and Other Floating Structures*, Rio de Janeiro, RJ, Brazil.

[118] Xiang, X., Faltinsen, O.M., 2011. Maneuvering of two interacting ships in calm water. *Marine Systems & Ocean Technology* 6 (2), 65-73.

[119] Xu, H.-f., Zou, Z.-j., Wu, S.-w., Liu, X.-y., Zou, L.J.S., 2017. Bank effects on ship–ship hydrodynamic interaction in shallow water based on high-order panel method[J]. *Ships and Offshore Structures*, 2017, 12(6):843-861.

[120] Xu, H., Zou, Z., Zou, L., Liu, X., 2016. Unsteady hydrodynamic interaction between two cylindroids in shallow water based on high-order panel method. E*ngineering Analysis with Boundary Elements* 70, 134-146.

[121] Yasukawa, H., 1990. A Rankine panel method to calculate unsteady ship hydrodynamic forces. *Journal of the Society of Naval Architects of Japan* 1990 (168), 131-140.

[122] Yasukawa, H., Yoshimura, Y., 2015. Introduction of MMG standard method for ship maneuvering predictions. *Journal of Marine Science and Technology* 20 (1), 37-52.

[123] Yeo, D.J., Yun, K., Kim, Y., 2016. Experimental Study on the Maneuvrability of KVLCC2 in Shallow Water, *4th MASHCO International Conference on Ship Maneuvring in Shallow and Confined Water with special focus on Ship Bottom Interaction*, Elbcampus, Hamburg, Germany, pp. 287-294.

[124] Yeung, R.W., 1978. On the interactions of slender ships in shallow water. *Journal of Fluid Mechanics* 85, 143-159.

[125] Yeung, R.W., 1982. Numerical methods in free-surface flows. *Annual review of fluid mechanics* 14 (1), 395-442.

[126] Yuan, Z.-M., 2019. Ship hydrodynamics in confined waterways. *Journal of Ship Research* 63 (1), 16-29.

[127] Yuan, Z.-M., He, S., Kellett, P., Incecik, A., Turan, O., Boulougouris, E., 2015a. Ship-to-ship interaction during overtaking operation in shallow water. *Journal of ship research* 59 (3), 172-187.

[128] Yuan, Z.-M., Incecik, A., Dai, S., Alexander, D., Ji, C.-Y., Zhang, X., 2015b. Hydrodynamic interactions between two ships travelling or stationary in shallow waters. *Ocean Engineering* 108, 620-635.

[129] Yuan, Z.-M., Li, M., Ji, C.-Y., Li, L., Jia, L., Incecik, A., 2019. Steady hydrodynamic interaction between human swimmers. *Journal of the Royal Society Interface 16* (150), 20180768.

[130] Yuan, Z.-M., Zhang, X., Ji, C.-Y., Jia, L., Wang, H., Incecik, A., 2018. Side wall effects on ship model testing in a towing tank. *Ocean Engineering* 147, 447-457.

[131] Yuan, Z.M., He, S., Kellett, P., Incecik, A., Turan, O., Boulougouris, E., 2015c. Ship-to-Ship Interaction during Overtaking Operation in Shallow Water. *Journal of Ship Research* 59 (3), 172-187.

[132] Yuan, Z.M., Incecik, A., 2016. Investigation of ship-bank, ship-bottom and ship-ship interactions by using potential flow method, *4th International Conference on Ship Maneuvring in Shallow and Confined Water*, Hamburg, Germany.

[133] Zaidi, H., Taiar, R., Fohanno, S., Polidori, G., 2008. Analysis of the effect of swimmer's head position on swimming performance using computational fluid dynamics. *Journal of Biomechanics* 41 (6), 1350-1358.

[134] Zhou, X., Sutulo, S., Guedes Soares, C., 2012. Computation of ship hydrodynamic interaction forces in restricted waters using potential theory. *Journal of Marine Science and Application* 11 (3), 265-275.

[135] Zou, L., Larsson, L.J.O.E., 2013. Numerical predictions of ship-to-ship interaction in shallow water[J]. *Ocean Engineering*, 2013, 72:386-402.